National Technical University of Athens

School of Civil Engineering

Diploma Thesis

CYCLIC ANALYSIS OF ELASTOPLASTIC STRUCTURES WITH KINEMATIC HARDENING

GEORGE TSILIMIDOS

Supervisor Professor: K. V. SPILIOPOULOS

OCTOBER, 2021

Dedication

To my parents

George Tsilimidos

Acknowledgements

I will be always grateful to Prof. K. V. Spiliopoulos for his clear guidance and encouragement. I want to thank him for the precious time that dedicated to me. The time of working on this thesis has been very effective.

I would like to thank Prof. M. Nerantzaki for giving me orientation and strong support.

I would like to thank PhD candidate J. Kapogiannis for his valuable help on the problems that I encountered during this work.

Contents

Chapter 0: Introduction

Overview

The main business of structural engineers is to design structures safely, economically and fficiently. Elastic analysis does not fully exploit the capacity of structures made of ductile materials. On the other hand, limit analysis finds the ultimate strength capacity (static collapse) with the assumption that applied loads on the structure are time-independent and proportional. This analysis defines the limit state of the structure made of elastic perfectly plastic material, and is specified in design codes (*strength design codes*) or standards. Actually, applied loads on the structures are mostly neither monotonic nor proportional, e.g. wind load on the buildings, traffic load on the bridges, waves onto the offshore oil-rigs, cyclic load on the machine devices, internal pressure in pipes, varying thermal load etc. Then the structure may fail by fatigue or unserviceability before reaching its ultimate strength capacity. Shakedown analysis defines the bounds of low cycle fatigue and incremental plastic collapse. A structure which is designed based on the shakedown limit is safer than a design based on the plastic limit. The concept of ratchetting (incremental plastic collapse) and alternating (low cycle fatigue) are rarely mentioned in the existing civil engineering design codes. However, all design codes of pressure vessels and piping allow extended loading by local plastifications in the first load cycles. For this they employ shakedown analysis implicitly (in the ASME Code) or also explicitly in the so called direct route of the European standard EN 13445-3, see Staat et al. (2005), Zeman et al. (2006).

The Notion of Shakedown

As there is no one-to-one stress-strain correspondence in the presence of plastic strains, the structural response to the same load can depend on the load history.

If a structure, made of an elastic-plastic material, is exposed to cyclic loads, then, in general, the following situations are possible:

1. If the load intensities remain sufficiently low, the structural response is perfectly elastic (with the exception of stress singularities).
2. If the load intensities become sufficiently high, the instantaneous load-carrying capacity of the structure becomes exhausted, plastic, unconstrained flow mechanism develops and the structure collapses.

Obviously, plastic deformations can develop also for loads below the collapse load.

3. If the plastic strain increments in each load cycle are of the same sign then, after a sufficient number of cycles, the total strains (and therefore displacements) become so large that the structure departs from its original form and becomes unserviceable. Such behaviour can be observed in experimental investigations. For a sufficiently high load amplitude (although below the statical load-carrying capacity) the deflection grows in each cycle. This phenomenon is called incremental collapse.
4. If the strain increments change sign in every cycle, they tend to cancel each other out and the total deformation remains small (this is so-called alternating plasticity). In this case, however, after a number of cycles material at the most stressed points begins to break due to low-cycle fatigue.

5. It may also happen that, after some plastic deformation in the initial load cycles, the structural behaviour becomes eventually elastic. Such stabilization of plastic deformations is called shakedown or adaptation.

It is worthwhile mentioning that the phenomena of incremental collapse and alternating plasticity (low-cycle fatigue) may appear simultaneously, e.g. if one component of the plastic strain tensor increases with each load cycle whereas another one oscillates.

The main problem of shakedown theory is to investigate whether or not a given structure will shake down under given loads. In this work, the question of shakedown will be answered by examining the structural behavior by means of a step-by-step procedure. However, it should be noted that such a procedure is very cumbersome and has great computational cost. Therefore,

some methods have been developed which allow one to find out whether a given structure is going to shake down, with no necessity to evaluate its future stress or strain states. These methods are called Direct Methods and have attracted many investigators' interest.

Description of Load Variations

The designer's knowledge of the future loadings to which a particular structure will be exposed is usually as follows:

1. types of loads (load modes) such as live load, wind load (sucking or pressure), water pressure, snow weight, dead weight, etc. are clearly determined
2. limits of variations of load intensities of particular load modes are also known as supplied by the design codes or they follow from some technological or service conditions
3. actual future history of the loads, however, is not given explicitly as it is impossible to predict throughout the life of the structure.

Within the framework of classical elastic structural mechanics, the designer had only to find out which one of the extreme load combinations resulted in maximum stress (or maximum reduced stress in the case of multi-axial stress states) and whether this maximum stress remained below an admissible level. In the case of plastic deformations such an approach can be inadequate.

However, as it will be proved later in Chapter 3, the shakedown load is not affected from the exact loading history (which is in general unknown), but only the extreme values.

Brief History of Shakedown

The fact that the collapse loads calculated according to limit analysis may fail to provide a proper measure of structural safety in the case of variable repeated loads, was pointed out for the first time by Griming as early as 1926 and later by Bleich, who proved the static shakedown theorem for a system of beams of ideal cross-sections. In 1936 Melan presented a more general theorem and later extended it to the general case of a continuum.

In 1957 Prager further extended the Melan theorem to account for thermal stresses. It was Koiter, who formulated a general kinematical shakedown theorem.

The notion of shakedown is applicable also in the case of strain-hardening. An appropriate static theorem was worked out by Melan, holding true for the generalized Bauschinger effect.

An extension to a more general strain-hardening model (the two surface model) was given by Weichert & Groβ-Weege.

Although the methods of shakedown analysis are already well-developed, there are few papers devoted to optimum structural design from the shakedown viewpoint.

Motivations and aims of the thesis

The main aim of this work is to investigate the shakedown bounds of problems addressed frequently in literature and compare the results of the step-by-step elastoplastic analyses with the results of various Direct Methods. Furthermore, the benefit of hardening on the shakedown load is investigated. The hardening model is the two-surface model introduced by Weichert & Groβ-Weege, which is a reasonable approach of the actual behaviour.

Organization of the thesis

Besides the introduction chapter, the thesis is structured in four chapters that can be read more or less independently. Chapter 1 presents the fundamentals of the theory of plasticity, with emphasis on models of the hardening effect. Chapter 2 presents the basic shakedown analysis theories. In this chapter, Melan's and Koiter's theorems are presented with emphasis on the shakedown problem for elastic-plastic bounded linearly kinematic hardening materials. Shakedown analysis states the design problem as a nonlinear optimization problem for the minimum of a failure load and for its dual, the maximum of a safe load. Chapter 3 describes the numerical method for the solution of the elastoplastic structure with the Finite Element Method and also the time histories of loading for the investigation of shakedown bounds. Chapter 4 provides some numerical applications and validations to verify the procedure.

Chapter 1: **Fundamentals in plasticity**

1.1 Inelastic behaviour of material

In the geometrically linear theory it is assumed that the total strain can be decomposed additively into an elastic or reversible part and an irreversible part (see Fig. 1.1). This decomposition is only possible under the assumption that the unloading branch is parallel to the elastic loading branch. If some thermal effects occur, a thermal strain term should be added and thus

$$\varepsilon_{ij} = \varepsilon_{ij}^{e} + \varepsilon_{ij}^{p} + \varepsilon_{ij}^{\theta}$$

Fig. 1.1c shows the idealized diagram of the uniaxial tensile test of mild steels, where $\sigma_y$and σ_u are yield stress and ultimate strength respectively. The graph indicates that there is an initial elastic range for the structural steels in which there is no permanent deformation on removal of the load. When the stress exceeds the elastic limit, the curve goes to inelastic range, consisting of two parts: initially, a perfectly plastic range occurs in which the steels yield, that is strain increases without increase in stress. Then follows a strain hardening range, where increase in strain is accompanied by a significant increase in stress. If the hardening range is ignored, the curve reduces to the elastic-perfectly plastic model as shown in Fig. 1.1b. Normally, the plastic strains are much larger than the elastic strains, and the material behaviour may be further simplified as rigid plastic, as shown in Fig. 1.1a.

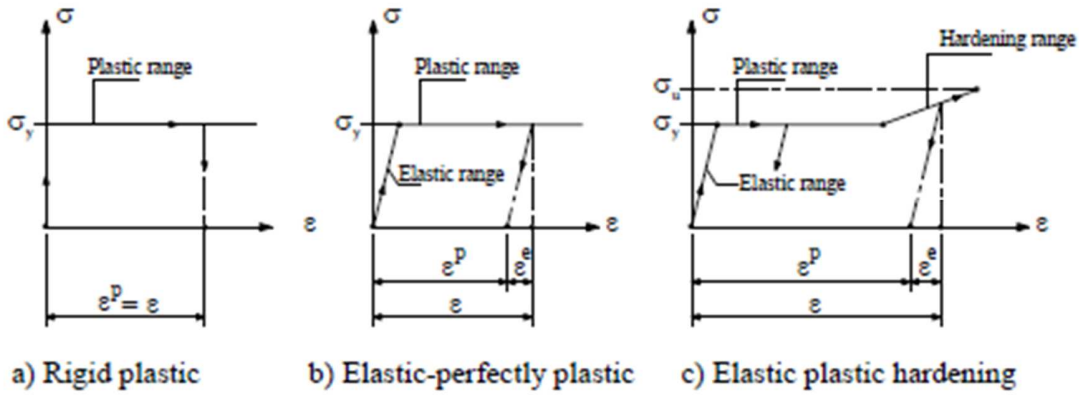

Figure 1.1: Simplified uniaxial stress-strain diagrams.

The elastic part of the strain obeys Hooke's law of linear elasticity

$$\varepsilon_{ij}^{e} = C_{ijkl}^{-1}\,\sigma_{kl}$$

where the elastic constants are components of a tensor of rank 4. For an isotropic material, this tensor is expressed in the form below

$$C_{ijkl} = \frac{\nu E}{(1+\nu)(1-2\nu)}\delta_{ij}\delta_{kl} + \frac{E}{2(1+\nu)}\left(\delta_{ik}\delta_{jl} + \delta_{il}\delta_{jk}\right)$$

Where E denotes the Young's modulus, ν the Poisson ratio, and $\delta_{\alpha\beta}$ (α,β=i,j,k,l) is the Kronecker delta (Cartesian unit tensor of second order).

Since both σ_{ij} and ε_{ij}^{e} are symmetric tensors, the C_{ijkl} and C_{ijkl}^{-1} tensors have

the following symmetries

$$C_{ijkl} = C_{jikl} = C_{ijlk} = C_{jilk}$$

The relationship can be inverted giving

$$\sigma_{ij} = 2G\varepsilon_{ij}^{e} + \frac{2\nu}{1-2\nu}G\delta_{ij}\varepsilon_{kk}^{e}$$

Where $G = \frac{E}{2(1+\nu)}$ is the shear modulus of elasticity.

The plastic strain rate obeys an associated flow law

$$\dot{\boldsymbol{\varepsilon}}^{p} = \dot{\lambda}\,\frac{\partial f}{\partial \boldsymbol{\sigma}}$$

where $\dot{\lambda}$ is a non-negative plastic multiplier and $f(\boldsymbol{\sigma}, \theta, \boldsymbol{\xi})$ represents a time-independent yield surface, which will be discussed in the section 1.2.

The plastic multiplier $\dot{\lambda}$ must satisfy the following complementarity conditions:

$$\dot{\lambda} \geq 0, \qquad f \leq 0, \qquad \dot{\lambda} f = 0$$

1.2 Yield function-yield surface

To develop a mathematical theory of plasticity, a basic assumption is made that there exists a continuous *scalar yield function* $f(\boldsymbol{\sigma}, \theta, \boldsymbol{\xi})$, which has following properties:

- The equation $f(\boldsymbol{\sigma}, \theta, \boldsymbol{\xi}) = 0$ represents a convex hypersurface, called *yield* or *loading surface*, in the stress space $\boldsymbol{\sigma}$ for a given temperature θ and an array of internal variables $\boldsymbol{\xi}$ which are determined experimentally. The plastic strain rate $\dot{\boldsymbol{\varepsilon}}^{p}$ can be nonzero in the region where $f(\boldsymbol{\sigma}, \theta, \boldsymbol{\xi}) = 0$.
- $f(\boldsymbol{\sigma}, \theta, \boldsymbol{\xi}) < 0$ represents the *elastic region*, which occupies the interior of the yield surface. In this region, both plastic strain rate $\dot{\boldsymbol{\varepsilon}}^{p}$ and all internal variables $\boldsymbol{\xi}$ are zeros.
- $f(\boldsymbol{\sigma}, \theta, \boldsymbol{\xi}) > 0$ corresponds to a region in stress space which is inaccessible for the material.

For multi-axial stresses, it is necessary to define *yield criteria* which will cause yielding. We present here after two most well-known *yield criteria* in plasticity. From fig.1.1, we can see that the initial yielding is the same for the cases with or without hardening.

Experiments have shown that the plastic deformation of metals essentially is independent of hydrostatic stress. Therefore, only the deviatoric stress

$$\boldsymbol{s} = \boldsymbol{\sigma} - \frac{1}{3} tr(\boldsymbol{\sigma})\boldsymbol{I}$$

causes yielding.

1.2.1 Von Mises yield criterion

The von Mises yield criterion is defined by the yield function

$$f(\boldsymbol{\sigma}) = J_2 - k_v^2 = 0$$

where
k_v is a material strength parameter. For a perfectly plastic material, k_v is a constant independent of strain history, for a hardening material k_v will be allowed to change with strain history.
J_2 is the second principal invariant of the stress deviator $\boldsymbol{s}$, which has the form

$$J_2 = \frac{1}{2}\boldsymbol{s}:\boldsymbol{s}$$

If the material is subjected to a pure shear σ_{12}, while all other stress components vanish, then $J_2 = \sigma_{12}^2$, and yielding should occur when $\sigma_{12} = k_v$. Hence *the constant* $k_v = {}^{\sigma_y}/_{\sqrt{3}}$ *is the yield stress in pure shear.*

1.2.3 Tresca yield criterion

Tresca concluded that the decisive factor for yielding is the maximum shear stress in the material. He proposed the yield criterion stipulating that the maximum shear stress has a constant value during plastic flow.
Using the principal stresses is the simplest way to express Tresca's idea. If the principal axes of stress are labelled $\sigma_1, \sigma_2, \sigma_3$ then Tresca's yield condition is

$$f(\sigma) = \max(|\sigma_1 - \sigma_3|, |\sigma_2 - \sigma_3|, |\sigma_1 - \sigma_3|) - 2k_T = 0$$

where $k_T = {}^{\sigma_y}/_{2}$.

The Tresca criterion can be put into an invariant form

$$f(J_2, J_3) = 4J_2^3 - 27J_3^2 - 36k_T^2 J_2^2 + 96k_T^4 J_2 - 64k_T^6 = 0$$

Where J_2, J_3 are the second and third invariants of the stress deviation tensor $\boldsymbol{s}$ with

$$J_3 = det(s_{ij}) = \frac{1}{3} s_{ij} s_{jk} s_{kl}$$

1.3 Perfectly plastic material and the initial yield surface

The yield function of perfectly plastic material, without hardening and temperature dependence is

$$f(\boldsymbol{\sigma}) = F[\boldsymbol{\sigma}] - \sigma_y^2 = 0$$

For isotropic materials, the yield function depends only on the *invariants* of stress.

$$f = f(I_1, I_2, I_3)$$

where I_1, I_2, I_3 are the three invariants of the stress tensor σ_{ij}. In terms of principal stresses, the yield function is expressed as:

$$f = f(\sigma_1, \sigma_2, \sigma_3)$$

The yield surface $f(\sigma_1, \sigma_2, \sigma_3) = 0$ can be plotted in a three-dimensional stress space. The von Mises yield criterion is $f = J_2 - k^2$, with k being a constant. The surface $f = 0$ appears as an infinite circular cylinder whose axis is equally inclined to the coordinate axes, where the principal stresses $\sigma_1, \sigma_2, \sigma_3$ are taken as the coordinate axes (Fig. 1.2).

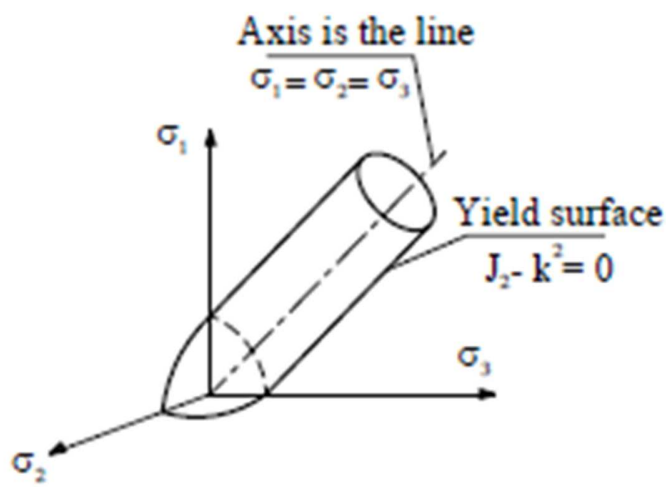

Figure 1.2: Yield surface according to von Mises criterion in the principal stress plane.

Since the effect of hydrostatic pressure on yield can be neglected, the yield function will be independent of $I_1 = \sigma_1 + \sigma_2 + \sigma_3$. It means that the yield function could be expressed advantageously as:

$$f = f(J_2, J_3)$$

where J_2, J_3 are the second and third invariants of the stress deviation tensor $\boldsymbol{s}$.
When f depends on J_2, J_3 alone, it can be written in the form

$$f = f(\sigma_1 - \sigma_3, \sigma_2 - \sigma_3)$$

and the yield surface $f = 0$ can be represented in two-dimensional plot with $\sigma_1 - \sigma_3, \sigma_2 - \sigma_3$ as coordinate axes, (Fig. 1.3).

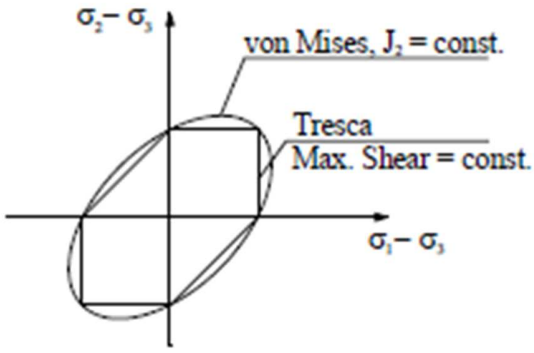

Figure 1.3: Yield surfaces plotted on the plane $(\sigma_1 - \sigma_3), (\sigma_2 - \sigma_3)$.

Another way of representing a yield surface when it is unaffected by hydrostatic pressure is to project the yield surface on the deviatoric plane $\sigma_1 + \sigma_2 + \sigma_3 = 0$, called the π-plane (Fig. 1.4).

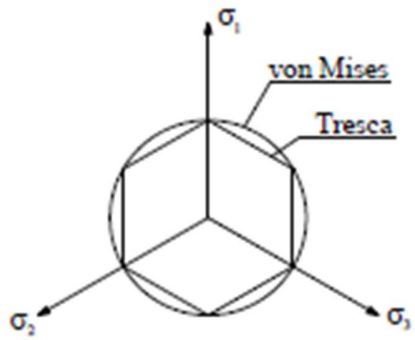

Figure 1.4: Projection of yield surfaces on the deviatoric plane.

1.4 Hardening materials and the subsequent yield surfaces

Experiments show that if you plastically deform a solid, then unload it, and then try to re-load it so as to induce further plastic flow, its resistance to plastic flow will have increased. This is known as strain hardening.

Obviously, we can model strain hardening by relating the size and shape of the yield surface to plastic strain in some appropriate way. There are many ways to do this. Here we describe the two simplest approaches.

1.4.1 Isotropic hardening and its subsequent yield surface

The isotropic hardening model assumes that the material remains isotropic during the process of plastic loading and that the subsequent yield surface is a uniform expansion of the initial yield surface. The initial and subsequent yield surfaces have the same centre, (Fig. 1.5).

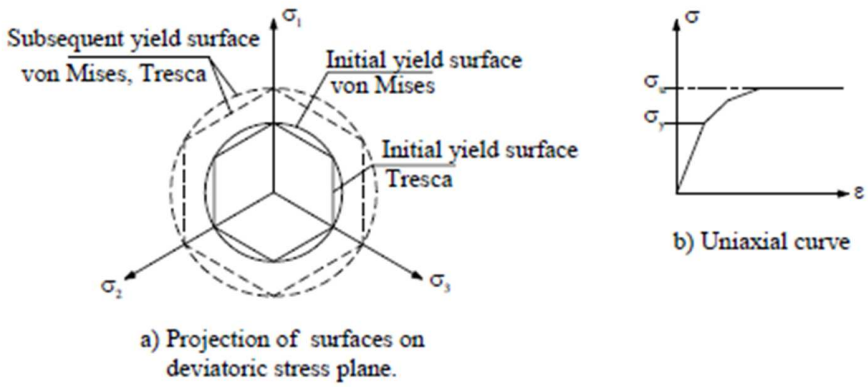

Figure 1.5: A model for isotropic hardening.

In a general case, the subsequent yield surfaces can be expressed in the form

$$f = f^*(J_2, J_3) - \sigma_y(\xi)$$

where ξ is an internal variable that characterizes the hardening of the material.

The *strainhardening hypothesis* assumes that σ_y is a monotonically increasing function, which depends only on the *effective plastic strain* but not the strain path.

To get a suitable scalar measure of effective plastic strain the accumulated plastic strain magnitude is defined

$$\overline{\varepsilon^p} = \int \sqrt{\frac{2}{3} d\varepsilon_{ij}^p d\varepsilon_{ij}^p}$$

(the factor of 2/3 is introduced so that $\overline{\varepsilon^p} = \varepsilon_{11}^p$ in a uniaxial tensile test in which the specimen is stretched parallel to the $\boldsymbol{e}_1$ direction)

Then σ_y is expressed as a function of $\overline{\varepsilon^p}$. Power laws or piecewise linear approximations are often used in practice. A few of the more common forms of isotropic hardening functions are:

- Perfectly plastic solid: $\sigma_y = constant$
- Linear strain hardening solid: $\sigma_y(\overline{\varepsilon^p}) = \sigma_y^0 + H\overline{\varepsilon^p}$
- Power—law hardening material: $\sigma_y(\overline{\varepsilon^p}) = \sigma_y^0 + H(\overline{\varepsilon^p})^{1/m}$

In these formulas, σ_y^0, H, m are material properties. These functions are illustrated in the figures below (fig 1.6)

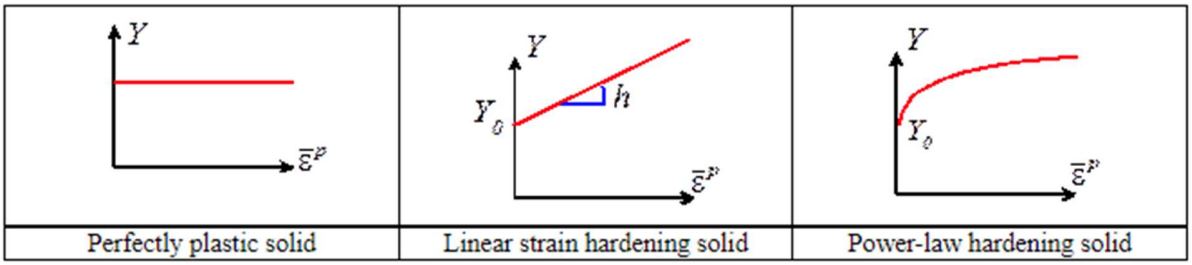

Figure 1.6: Basic models for yield stress.

However, an isotropic hardening law is generally not useful in situations where the structure is subjected to cyclic loading. It does not account for the Bauschinger effect, and so it predicts that after a few cycles the structure will just harden until it responds elastically. This model rejects the possibility of incremental plasticity.

1.4.2 Bauschinger effect

The Bauschinger effect refers to a property of materials where the material's stress/strain characteristics change as a result of the microscopic stress distribution of the material. For example, an increase in tensile yield strength occurs at the expense of compressive yield strength. The effect is named after German engineer Johann Bauschinger.

While more tensile cold working increases the tensile yield strength, the local initial compressive yield strength after tensile cold working is actually reduced. The greater the tensile cold working, the lower the compressive yield strength (fig 1.7).

It is a general phenomenon found in most polycrystalline metals. Based on the cold work structure.

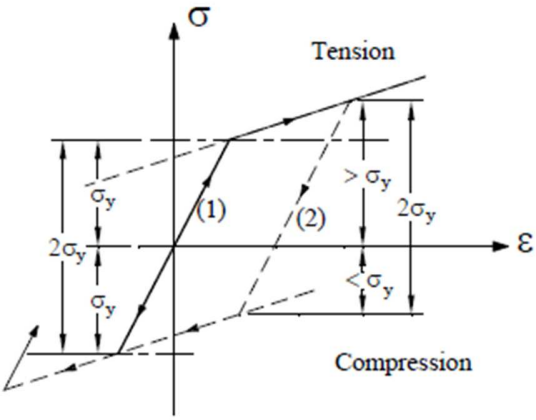

Figure 1.7: An expression of the Bauschinger effect.

1.4.3 Kinematic hardening and its subsequent yield surface

The kinematic hardening leads to a translation of the loading surface corresponding to the propagation and generation of dislocations in crystalline solids. The initial yield surface can translate without changing its shape and size. The translation may be limited by obstacles for the motions of the dislocations causing a back-stress on the dislocations so that their motion becomes progressively more difficult. This is observed as work-hardening effect i.e. increasing applied stress is necessary to produce additional plastic deformation.

a. Unbounded kinematic hardening model

The original Melan-Prager model is characterized by unbounded translation of the loading surface in the multi-axial stress space. Fig. 1.8a shows that the subsequent yield surface can translate unboundedly, and as mentioned before, this hardening model rejects the possibility of incremental plasticity. The subsequent yield surface translates with the evolution of the back-stress $\boldsymbol{\pi}$. This evolution for loading and unloading paths starts once the structure begins to yield, see Fig 1.8b for linearly kinematic hardening material.

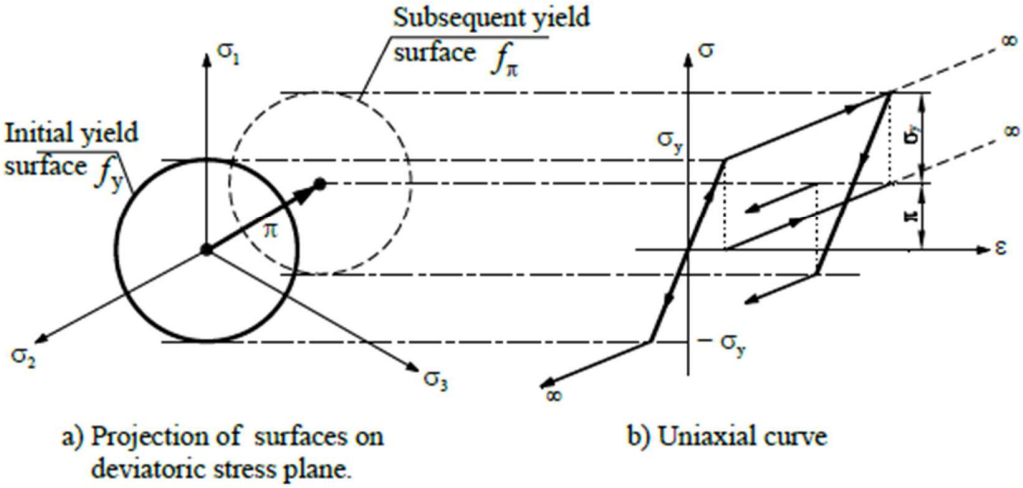

Figure 1.8: A model for unbounded linearly kinematic hardening.

In the case of kinematic hardening, the yield function is defined using the reduced stress tensor which is the difference of the backstress from the total stress $\boldsymbol{\sigma} - \boldsymbol{\pi}$.

Thus, the yield criterion becomes

$$f_\pi(\boldsymbol{\sigma}, \boldsymbol{\pi}) = F[\boldsymbol{\sigma} - \boldsymbol{\pi}] - \sigma_y^2 = 0$$

The evolution of backstresses $\boldsymbol{\pi}$ need to be related to the plastic strain history. There are many ways to do this, which can model subtle features of the plastic response of solids under cyclic and non-proportional loading. The simplest approach is the linear kinematic hardening model where

$$\dot{\boldsymbol{\pi}} = \frac{2}{3} C \dot{\boldsymbol{\varepsilon}}^p$$

with the material constant C being the slope of the stress- plastic strain curve.

A more sophisticated approach is to set

$$\dot{\boldsymbol{\pi}} = \frac{2}{3} C \dot{\boldsymbol{\varepsilon}}^p - \gamma \boldsymbol{\pi} \dot{\overline{\varepsilon^p}}$$

where C and γ are material constants. It's not so easy to visualize what this does – it turns out that that this relation can model *cyclic creep* – the tendency of a material to accumulate strain in the direction of mean stress under cyclic loading, as illustrated in the figure 1.9.

It is known as the Armstrong-Frederick hardening law.

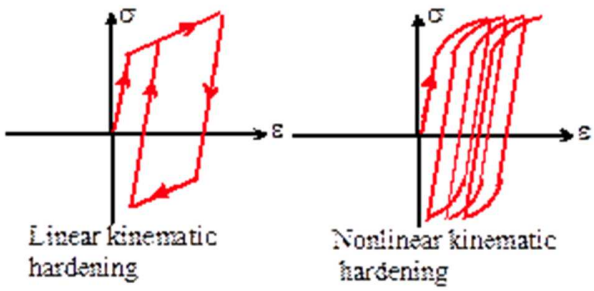

Figure 1.9: Linear and nonlinear kinematic hardening models.

Unbounded kinematic hardening means that the ultimate strength σ_u of the material is infinite, so this model is not realistic and not suitable for limit analysis. Moreover, a structure made of unbounded linearly kinematic materials can fail only by alternating plasticity, i.e. it is impossible for such a structure to be involved in incremental plastic collapse, while the alternating plasticity limit (plastic fatigue) exists and is the same for materials with and without hardening.

More realistic two surface models of bounded kinematic hardening have been introduced by Weichert and Gross-Weege. We present these models in the next section.

b. Bounded with two-surface plasticity model

In the two-surface model of plasticity the translation of f_π is constrained by a bounding surface f_u. This model means that one surface is the initial surface f_y and the other one is the bounding surface f_u (see Fig. 1.10). The stress $\boldsymbol{\sigma}$ is bounded by the ultimate strength σ_u. The initial yield surface can translate inside the bounding surface, without changing its shape and size, such that *the subsequent yield surface always stays inside a bounding surface*, consequently, *the center of the subsequent yield surface cannot move outside the back-stress surface* f_b. Fig. 1.10b shows the case of nonlinear kinematic hardening of e.g. the Armstrong-Frederick model in which the bounding surface is reached asymptotically. The two-surface shakedown analysis uses a linearly kinematic hardening model. According to Staat and Heitzer, both models give very close shakedown limits.

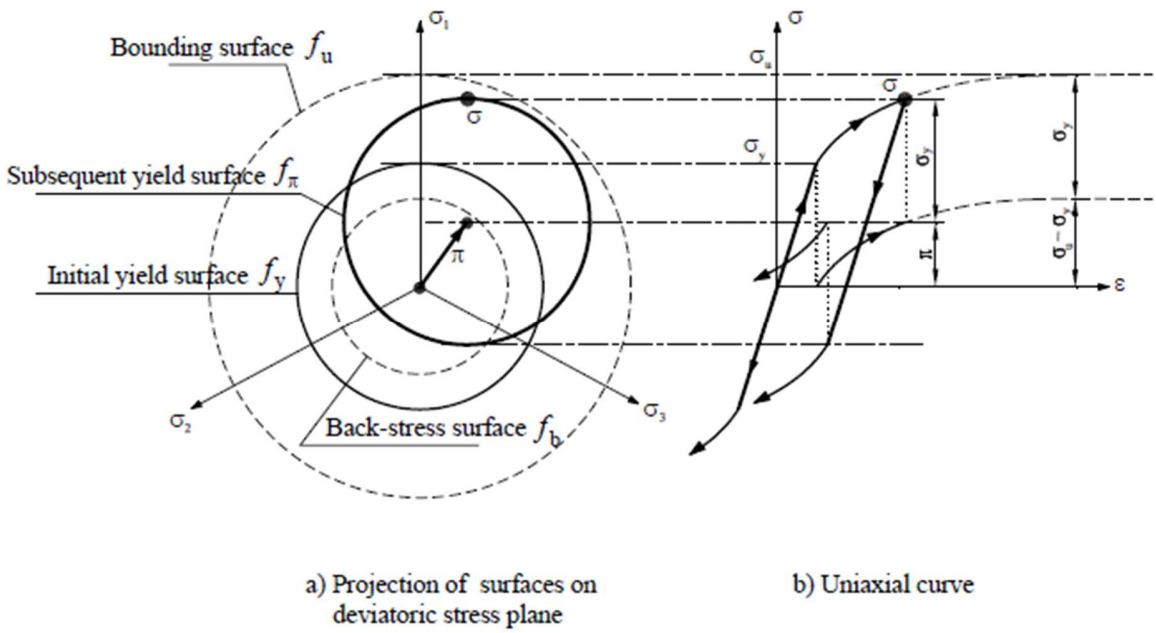

Figure 1.10: A two-surface model for bounded kinematic hardening.

The subsequent yield surface may or may not touch the bounding surface. It is bounded by one of the two following ways:

a) *it always stays inside a bounding surface,* expressed by the following condition

$$F[\boldsymbol{\sigma}] \leq \sigma_u^2$$

b) *its centre cannot move outside the back-stress surface* f_b, expressed by the following condition

$$F[\boldsymbol{\sigma} - \boldsymbol{\pi}] \leq \left(\sigma_u - \sigma_y\right)^2$$

The inequalities can be proven to be equivalent.

When $\sigma_u \geq 2\sigma_y$ then shakedown limit of bounded kinematic hardening structure can be proved that is equal to that of unbounded kinematic hardening structure.

1.5 Drucker's postulate

Drucker's postulates were developed in the 1950s in an attempt to provide the missing link between material behaviour and mathematics.

The process of application and removal of the additional stress is called *stress cycle*. Removing the additional stress enables the stress of the structure to return to the original stress state, but the

strain state can be different if plastic deformation occurred during the stress cycle. Note that $d\boldsymbol{\sigma}: d\boldsymbol{\varepsilon}^{\boldsymbol{e}}$ is always positive, due to positive definiteness of the tensor of elasticity, where $d\boldsymbol{\varepsilon}^{\boldsymbol{e}}$ is the elastic strain increment which is recoverable. Drucker accordingly defines a work-hardening (or "stable") plastic material if the following two conditions hold true:

- *the work done during incremental loading is positive*

$$d\boldsymbol{\sigma}: d\boldsymbol{\varepsilon} > 0$$

- *the work done in the loading-unloading cycle is nonnegative*

$$d\boldsymbol{\sigma}: (d\boldsymbol{\varepsilon} - d\boldsymbol{\varepsilon}^{\boldsymbol{e}}) = d\boldsymbol{\sigma}: d\boldsymbol{\varepsilon}^{\boldsymbol{p}} \geq 0$$

where $d\boldsymbol{\varepsilon}^{\boldsymbol{p}}$ is the *plastic strain increment*, which is not recovered by the process of *stress cycle*. The second equation, sometimes known simply as **Drucker's inequality**, is valid for both work-hardening and perfectly plastic materials, where for the case of perfect plasticity, it assumes equality: $d\boldsymbol{\sigma}: d\boldsymbol{\varepsilon}^{\boldsymbol{p}} = 0$

Drucker's inequality can be extended to allow for a finite $d\boldsymbol{\sigma}$ produced by the external agency. In fact, the initial stress $\boldsymbol{\sigma}^0$, may not at any point be outside the yield surface such that $\boldsymbol{\sigma}^0 \leq \boldsymbol{\sigma}$. The work per unit volume done by the external agency is $(\boldsymbol{\sigma} - \boldsymbol{\sigma}^0): d\boldsymbol{\varepsilon}^{\boldsymbol{p}}$, thus the inequality becomes

$$(\boldsymbol{\sigma} - \boldsymbol{\sigma}^0): d\boldsymbol{\varepsilon}^{\boldsymbol{p}} \geq \mathbf{0}$$

The last equation is also called the *principle of maximum plastic dissipation*.

It can be written in the form

$$\boldsymbol{\sigma}: \dot{\boldsymbol{\varepsilon}}^{\boldsymbol{p}} = D(\dot{\boldsymbol{\varepsilon}}^{\boldsymbol{p}}, \boldsymbol{\xi}) \geq \boldsymbol{\sigma}^{\mathbf{0}}: \dot{\boldsymbol{\varepsilon}}^{\boldsymbol{p}}$$

where the *plastic dissipation* $D(\dot{\boldsymbol{\varepsilon}}^{\boldsymbol{p}}, \boldsymbol{\xi})$ depends on the plastic strain rate $\dot{\boldsymbol{\varepsilon}}^{\boldsymbol{p}}$ and the internal variable $\boldsymbol{\xi}$ only.

Consequences of Drucker's postulate

- *The yield surface and all subsequent loading surfaces must be convex.*

The convexity of the yield surface plays a very important role in plasticity. It permits the use of convex programming in limit and shakedown analysis. It should be noted that Drucker's postulate is quite independent of the basic laws of thermodynamics. It does not hold if internal structural changes occur or for temperature dependent behaviour. Furthermore, the yield surface fails to be convex if there is an interaction between elastic and plastic deformations, i.e. if the elastic properties depend on the plastic deformation.

- *The plastic strain increment vector must be normal to the loading surface at a regular point, and it must lie between the adjacent normals to the loading surface at a corner of the surface.*

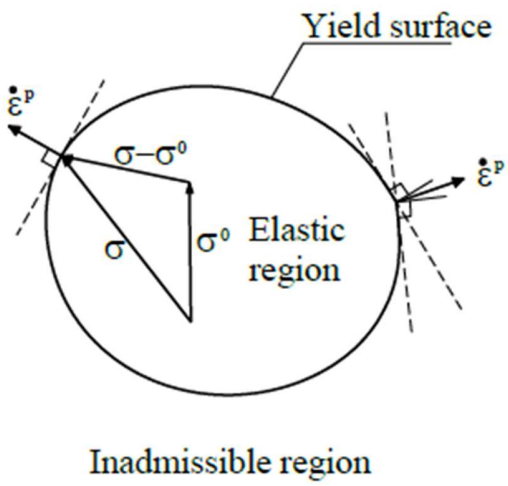

Figure 1.11: Normality rule

Two above consequences are equivalent with the principle of maximum plastic dissipation $(\boldsymbol{\sigma} - \boldsymbol{\sigma}^0) : d\boldsymbol{\varepsilon}^{\boldsymbol{p}} \geq \mathbf{0}$, and can be represented as

$$\dot{\boldsymbol{\varepsilon}}^p = \dot{\lambda} \frac{\partial f}{\partial \boldsymbol{\sigma}}$$

In the case of having n intersected differentiable yield surfaces at a singular point, plastic flow rule becomes:

$$\dot{\boldsymbol{\varepsilon}}^p = \sum_{k=1}^{n} \dot{\lambda}_k \frac{\partial f_k}{\partial \boldsymbol{\sigma}}$$

- The rate of change of plastic strain must be a linear function of the change of the stress.

1.6 Plastic dissipation functions

The plastic dissipation function is defined as

$$D(\dot{\boldsymbol{\varepsilon}}^p, \boldsymbol{\xi}) = \boldsymbol{\sigma} : \dot{\boldsymbol{\varepsilon}}^p$$

where $\boldsymbol{\sigma}$ is the existing stress tensor satisfying the yield condition $f(\boldsymbol{\sigma}, \boldsymbol{\xi}) = 0$.

It follows from the principle of maximum plastic dissipation $\boldsymbol{\sigma} : \dot{\boldsymbol{\varepsilon}}^p$ that, for a given temperature, the dissipation is defined uniquely by the plastic strain rate $\dot{\boldsymbol{\varepsilon}}^p$.

From the same principle follow some important inequalities for the dissipation function:

- $\int_{t_1}^{t_2} D(\dot{\boldsymbol{\varepsilon}}^p)\, dt \geq D(\Delta \boldsymbol{\varepsilon}^p)$,where $\Delta \boldsymbol{\varepsilon}^p = \boldsymbol{\varepsilon}^p(t_2) - \boldsymbol{\varepsilon}^p(t_1)$

- $D(\dot{\boldsymbol{\varepsilon}}_1^p + \dot{\boldsymbol{\varepsilon}}_2^p) \leq D(\dot{\boldsymbol{\varepsilon}}_1^p) + D(\dot{\boldsymbol{\varepsilon}}_2^p)$,with equality when there exist constant $a > 0$ such that $\dot{\boldsymbol{\varepsilon}}_1^p = a\dot{\boldsymbol{\varepsilon}}_2^p$
- $D(a\dot{\boldsymbol{\varepsilon}}^p) = aD(\dot{\boldsymbol{\varepsilon}}^p), a \geq 0$

1.7 Fundamental principles in plasticity

Consider a structure subjected to volume loads (body force) $\boldsymbol{f}$ and surface loads $\boldsymbol{t}_0$. The stresses $\boldsymbol{\sigma}$ are said to be in equilibrium if they satisfy the equations of internal equilibrium

$$div\boldsymbol{\sigma} + \boldsymbol{f} = \boldsymbol{0} \; in \; V$$

and the conditions of equilibrium on the traction boundary ∂V_σ of the body

$$\boldsymbol{\sigma n} = \boldsymbol{t}_0 \; on \; \partial V_\sigma$$

Any stress field satisfying both conditions of equillibrium is called a *statically admissible* field.

Furthermore, if this stress field nowhere violates the yield criterion $f(\boldsymbol{\sigma}) \leq 0$, it is called a *plastically admissible* or *licit* stress field.

The actual flow mechanism is composed of the velocities $\dot{\boldsymbol{u}}$ and strain rate $\dot{\boldsymbol{\varepsilon}}$ in the body which satisfy the compatibility condition and kinematical boundary conditions

$$\dot{\boldsymbol{\varepsilon}} = \frac{1}{2}(\nabla\dot{\boldsymbol{u}} + (\nabla\dot{\boldsymbol{u}})^T) \; in \; V$$

$$\dot{\boldsymbol{u}} = \dot{\boldsymbol{u}}_{\boldsymbol{0}} \; on \; \partial V_u$$

Any mechanism satisfying both conditions is called *kinematically admissible*.

Furthermore, if this mechanism furnishes a non-negative external rate of work

$$W_{ex} = \int_V \boldsymbol{f}^T \dot{\boldsymbol{u}} \, dV + \int_{\partial V_\sigma} \boldsymbol{t}_0{}^T \dot{\boldsymbol{u}} \, dS \; \geq 0$$

then it is called a *licit* mechanism. A kinematically admissible strain and displacement field can be defined in a similar manner.

Principle of virtual work

One of the main tools in the mechanics of continua is the principle of virtual work, which states that *for all strain rate tensors* **ε** *and velocity vectors* **u** *that are kinematically admissible, and for all stresses* **σ** *that are statically admissible we have the following virtual power equation*

$$\int_V \boldsymbol{\sigma} : \dot{\boldsymbol{\varepsilon}}\, dV = \int_V \boldsymbol{f}^T \dot{\boldsymbol{u}}\, dV + \int_{\partial V_\sigma} \boldsymbol{t}_0{}^T \dot{\boldsymbol{u}}\, dS + \int_{\partial V_u} (\boldsymbol{n}\boldsymbol{\sigma})^T \dot{\boldsymbol{u}}_0\, dS$$

It should be emphasized that the statical and kinematical quantities can be unrelated.

The physical interpretation of the above equation is, *the External virtual work is equal to internal virtual work when equilibrated forces and stresses undergo unrelated but consistent displacements and strains*.

In the above variational principle, no constitutive equation of the material is assumed, so it is applicable even if the body is not elastic, for which the energy functional cannot be defined.

The finite element analysis of structures is based on this variational equation.

1.8 Some General Relations for Elastic-Plastic Structures

An elastic-plastic structure may be regarded as a linear elastic structure with an imposed distortion field.

In many considerations it is useful to employ a notion of a fictitious perfectly elastic structure of the same geometry and elastic properties as the actual structure. Then the actual stress field σ_{ij} can be decomposed in the following manner:

$$\sigma_{ij} = \sigma_{ij}^e + \rho_{ij}$$

where σ_{ij}^e denotes the stress field which would appear in the reference structure if subjected to the same loads as the actual one. The remaining part ρ_{ij} satisfies the internal equilibrium equations for vanishing body forces and homogeneous statical boundary conditions on that part of the boundary on which surface tractions are prescribed. Therefore the field ρ_{ij} is called the *residual stress* or *instantaneous residual stress.*

On substituting Hooke's law in the total strain decomposition and substituting the above decomposition for the actual stress one obtains the following decomposition of the actual strain field

$$\varepsilon_{ij} = C_{ijkl}^{-1}\sigma_{kl}^e + \varepsilon_{ij}^\theta + \varepsilon_{ij}^p + C_{ijkl}^{-1}\rho_{kl}$$

It can easily be seen that the first two terms constitute the strain field in the reference perfectly elastic structure when exposed to the same loads and temperature. This field is compatible with the displacement field u_i^e appropriate for the reference elastic structure. As the total strain field ε_{ij} is also compatible the last two terms clearly result from a certain displacement field u_i^r called the residual displacement field.

$$\varepsilon_{ij}^{\theta} + C_{ijkl}^{-1}\sigma_{kl}^{e} = \frac{1}{2}\left(u_{i,j}^{e} + u_{j,i}^{e}\right)$$
$$\varepsilon_{ij}^{p} + C_{ijkl}^{-1}\rho_{kl} = \frac{1}{2}\left(u_{i,j}^{r} + u_{j,i}^{r}\right)$$
$$u_i = u_i^e + u_i^r$$

It will be proven that, at every instant, the residual stress ρ_{ij} and displacement u_i^r fields are uniquely defined by the instantaneous plastic strain field ε_{ij}^{p}.

Let us assume that there exist two different residual stress fields ρ_{ij} and τ_{ij}. From the virtual work principle:

$$\int_V \rho_{ij}\left[C_{ijkl}^{-1}\rho_{kl} + \varepsilon_{ij}^{p}\right]dV = \int_V \tau_{ij}\left[C_{ijkl}^{-1}\rho_{kl} + \varepsilon_{ij}^{p}\right]dV = \int_V \tau_{ij}\left[C_{ijkl}^{-1}\tau_{kl} + \varepsilon_{ij}^{p}\right]dV = 0$$

On simple rearrangements one obtains

$$\int_V \left(\rho_{ij} - \tau_{ij}\right)C_{ijkl}^{-1}(\rho_{kl} - \tau_{kl})dV = 0$$

As the integrand is strictly-positively definite: $\rho_{ij} = \tau_{ij}$

By assuming the existence of two different residual displacement fields u_i^r, $\overline{u}_i$, in view of the above result, one obtains from the compatibility equation of the residual displacement field that

$$(u_i^r - \overline{u}_i)_{,j} + \left(u_j^r - \overline{u}_j\right)_{,i} = 0$$

which implies that the fields may differ only by a rigid-body motion. In the case of the kinematical boundary conditions prevailing in practice this implies that $u_i^r = \overline{u}_i$.

Chapter 2: **Shakedown theories**

2.1 Behaviour of a structure

For structures subjected to varying loads, shakedown is more relevant than static collapse, which has been investigated by limit analysis. A structure made of perfectly plastic materials as well as linear or nonlinear kinematic hardening materials, subjected to cyclic loads may behave in one of the following ways, depending on the intensity and character of the applied loads:

1. If the applied loads are sufficiently low, the behaviour of the structure is purely elastic ($\boldsymbol{\varepsilon} = \boldsymbol{\varepsilon}^e$).When the first point of the body reaches the yield stress, it reaches the elastic limit, (see Fig. 2.1). The behaviour of the structure according to this state does not influence its integrity, since macroscopic plastic deformation and damage do not occur at all (except of high cycle fatigue, HCF). However, the load carrying potential of the structure is not fully exploited.

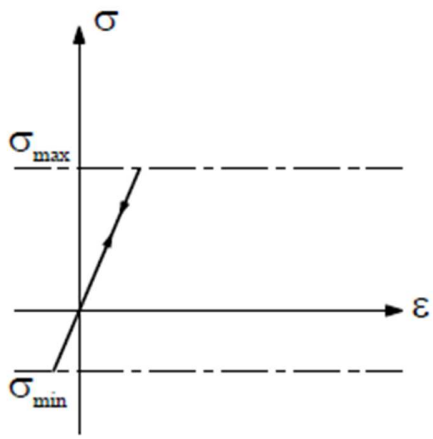

Figure 2.1: Purely elastic

2. If the load intensities is higher than the elastic limit, but do not exceed a certain limit (shakedown limit load), then plastic deformation occurs initially ($\dot{\boldsymbol{\varepsilon}}^p \neq \mathbf{0}$). After some cycles, the structure reaches a steady state in which the total plastic energy dissipated in the structure becomes bounded, no further plastic deformation occurs ($\dot{\boldsymbol{\varepsilon}}^p = \mathbf{0}$). The structure behaves as if it was elastic. We can say that the structure shakes down or the structure adapts itself, (see Fig. 2.2).

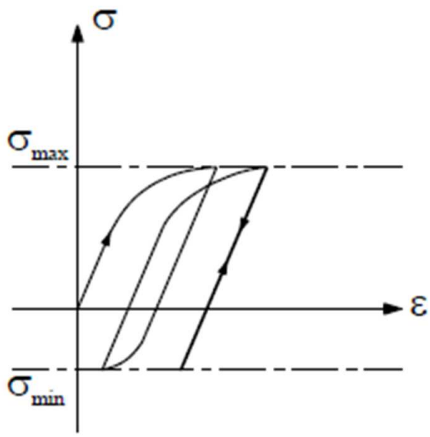

Figure 2.2: Shakedown.

3. If the load intensity is higher than the shakedown limit, then no stabilization situation is established, plastic flow continues to develop. The response of the structure may be one of the two following modes (or both simultaneously):
    - If the plastic strain increments in each load cycle, $(\dot{\boldsymbol{\varepsilon}}^p \neq \mathbf{0})$, are of the same sign, the plastic deformations in each cycle accumulates, $\Delta\boldsymbol{\varepsilon}^p \neq 0$, so that after enough cycles the total strains (and therefore displacements) become so large that the structure departs from its original form and becomes unserviceable. This phenomenon is called *incremental collapse* or *ratchetting* (see Fig. 2.3).

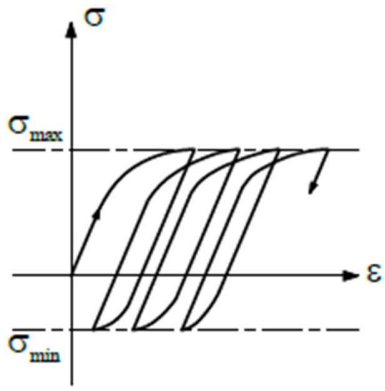

Figure 2.3: Ratchetting.

- If the plastic strain increments change sign in every cycle $(\dot{\boldsymbol{\varepsilon}}^p \neq \mathbf{0})$, they tend to cancel each other $\Delta\boldsymbol{\varepsilon}^p = 0$, and the *net* deformation remains small. However, after a sufficient number of cycles, the structure may fail by fracture due to Low Cycle Fatigue (LCF). This phenomenon is called *alternating plasticity* or *low cycle fatigue,* (see Fig. 2.4). <u>Hardening does not affect this state.</u>

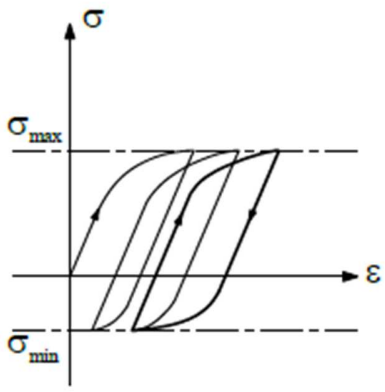

Figure 2.4: Alternating plasticity.

Note that: (1) incremental collapse and alternating plasticity may appear simultaneously, and (2) in the alternating plasticity mode, there is no essential difference between elastic-perfectly plastic and kinematic hardening materials.

4. If the load intensity is higher than the ultimate strength capacity of the structure, $(P > P_{lim})$, then the structure collapses instantaneously. This collapse is relevant to static collapse (see Fig. 2.5). The ultimate strength capacity of the structure made of unbounded kinematic hardening material is infinite.

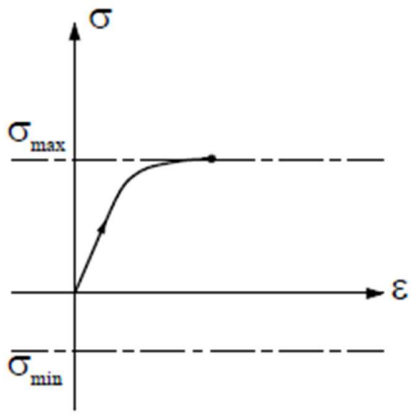

Figure 2.5: Instantaneous plastic collapse.

2.2 An intuitive criterion of shakedown

An intuitive examination of the above cases shows that if a given structure is going to shake down the total amount of plastic energy dissipated over any possible load path must be finite. Indeed, most of the authors have formulated shakedown criteria in this way. However, it should be kept in mind that such a concept of shakedown leads to an approximate description. The total

energy dissipated may be finite even if plastic strain increments appear at every load cycle but comprise a convergent series. On the other hand, boundedness of the total plastic work, without its maximum value being specified, seems to be sometimes too weak a requirement, e.g. if low-cycle fatigue is considered.

Nevertheless, the test results seem to confirm the theoretical predictions.

The shakedown criterion described above is

$$W_p = \int_0^t \sigma_{ij} \dot{\varepsilon}_{ij}^p dt < \infty$$

The above criterion is equivalent to the condition of boundedness of the maximum plastic strain

$$\max_{\boldsymbol{x} \in V} \max_{i,j} \lim_{t \to \infty} \left| \varepsilon_{ij}^p(\boldsymbol{x}, t) \right| < \infty$$

However, such a local definition causes substantial mathematical difficulties in formulating the basic shakedown theorems. A less stringent criterion reads

$$w_p = \frac{1}{V} \int_V \int_0^t \sigma_{ij} \dot{\varepsilon}_{ij}^p dt \, dV < w_0$$

where w_0 is a material constant suitably measured from low-cycle fatigue tests.

It can be shown that in the case of low-cycle fatigue, both of the above criteria, are approximations to the material failure criterion derived from experimental data. They also ensure, to some extent, boundedness of maximum deflections, in other words they state that incremental collapse is prevented.

2.3 Definition of load domain and fictitious elastic stress field

In shakedown analysis, the applied loads may vary independently, so it is necessary to define the load domain L. This load domain contains all possible load histories.

2.3.1 Load domain

We study here the shakedown problem of a structure subjected to n time-dependent (thermal and mechanical) loads $\overline{P}_k(t)$ with time denoted by t each of them can vary independently within a given range

$$\overline{P}_k(t) \in I_k = \left[\overline{P}_k^-, \overline{P}_k^+\right] = [\mu_k^-, \mu_k^+] P_k^0 \, , k = 1, \dots, n$$

These loads form a convex polyhedral domain L of n dimensions with $m = 2^n$ vertices in the load space, as shown in Fig. 2.6a and 2.6b for two variable loads and three variable loads respectively. These load domains can be represented in the following linear form

$$\boldsymbol{P}(t) = \sum_{k=1}^{n} \mu_k(t) P_k^0$$

where

$$\mu_k^- \leq \mu_k(t) \leq \mu_k^+$$

(a): Convex load domain with two variable loads

$$\boldsymbol{P}(t) = \sum_{k=1}^{2} \mu_k(t) P_k^0$$

The load domain L has 4 vertices:

$$\widehat{\boldsymbol{P}}_1 = \widehat{\boldsymbol{P}}_1(\mu_1^- P_1^0, \mu_2^+ P_2^0)$$
$$\cdots$$
$$\widehat{\boldsymbol{P}}_4 = \widehat{\boldsymbol{P}}_4(\mu_1^- P_1^0, \mu_2^- P_2^0)$$

and the domain can be enlarged by the load factor a

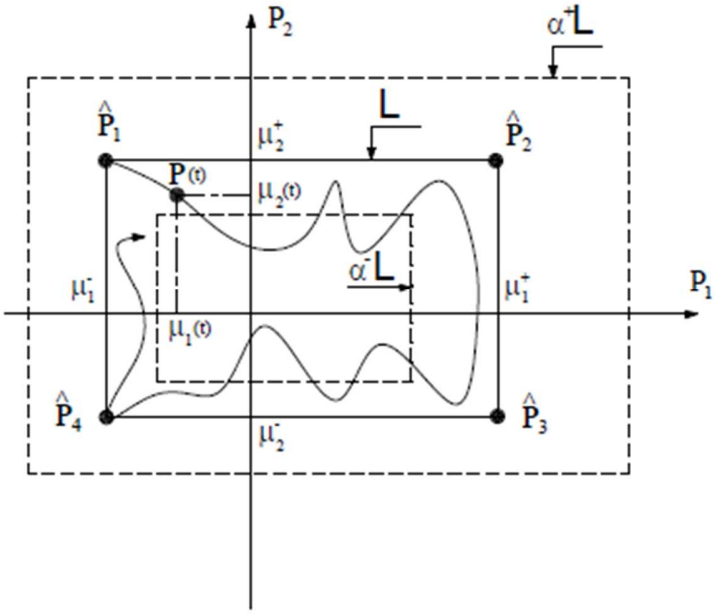

Figure 2.6a: Load domain with two variable loads.

(b): Convex load domain with three variable loads (axial force, moment, pressure)

$$\boldsymbol{P}(t) = \sum_{k=1}^{3} \mu_k(t) P_k^0$$

The load domain L has 8 vertices:

$$\widehat{\boldsymbol{P}}_1 = \widehat{\boldsymbol{P}}_1\left(\mu_p^+ p^0, \mu_N^- N^0, \mu_M^+ M^0\right)$$
$$\cdots$$
$$\widehat{\boldsymbol{P}}_8 = \widehat{\boldsymbol{P}}_8\left(\mu_p^+ p^0, \mu_N^+ N^0, \mu_M^- M^0\right)$$

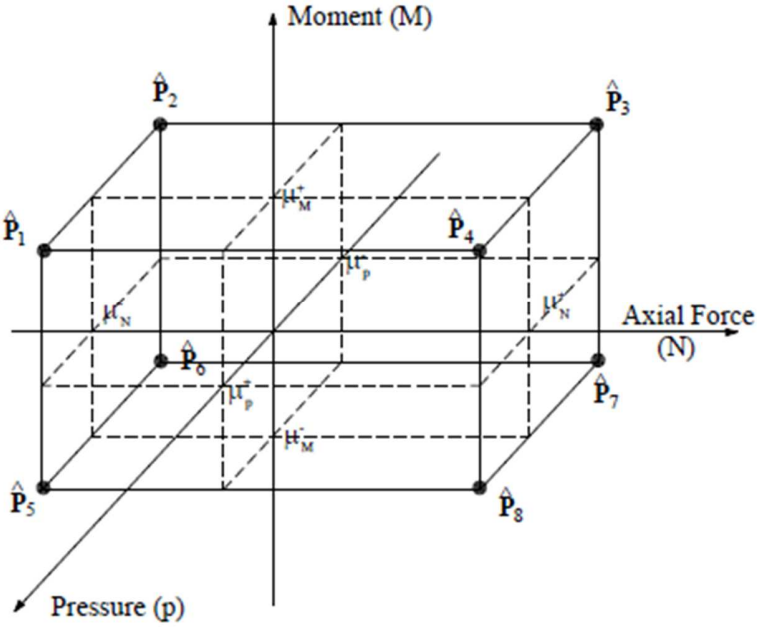

Figure 2.6b: Load domain with three variable loads.

Intuitively, from these load domains, we can see that for limit analysis, the monotone load is a case with only one point belonging to the load domain. In this way limit analysis is a special case of shakedown analysis.

2.3.2 Fictitious elastic stress field

In the case of limit and shakedown analysis, it is useful to describe this load domain L in the stress space. To this end, we use here the notion of a *fictitious perfectly elastic* structure which was introduced earlier in 1.8.

Applying the superposition principle, this fictitious elastic stress tensor field may be written in the form

$$\boldsymbol{\sigma}^e(\boldsymbol{x}, t) = \boldsymbol{\sigma}^e\left(\sum_{k=1}^{n} \mu_k(t) P_k^0\right) = \sum_{k=1}^{n} \mu_k(t) \boldsymbol{\sigma}_k^e(\boldsymbol{x})$$

It will be proven later that it is sufficient to only consider the relevant load vertices $\widehat{\boldsymbol{P}}_k$ instead of the entire load history to produce the shakedown limit.

With the concept of the fictitious elastic stress field, we can write:

$$\int_0^T \left(\int_V \boldsymbol{f}^T \, \dot{\boldsymbol{u}} \, dV + \int_{\partial V_\sigma} \boldsymbol{t}_0{}^T \, \dot{\boldsymbol{u}} \, dS \right) dt = \int_0^T \left(\int_V \boldsymbol{\sigma}^e(\boldsymbol{x}, t) : \dot{\boldsymbol{\varepsilon}}^p \, dV \right) dt > 0$$

2.4 Fundamental theorems of shakedown

In this section, we will present two basic theorems of shakedown, where the static or lower bound theorem investigates the shakedown or safe region, while the kinematic or upper bound theorem investigates the non-shakedown or failure region.

2.4.1 Static shakedown theorem (Melan)

Let us assume that a given structure has already shaken down over an arbitrary load path contained within a given load factors domain L. Then the generated plastic strain field $\varepsilon_{ij}^p = \overline{\varepsilon}_{ij}$ will not vary any more, neither will the residual stress field $\rho_{ij} = \overline{\rho}_{ij}$ irrespective of the elastic stress $\sigma_{ij}^e(x, t)$.

From the above reasoning it follows that the necessary condition for shakedown is the existence of a steady residual stress field $\overline{\rho}_{ij}$ such that

$$F\left[a\sigma_{ij}^e(\boldsymbol{x}, t) + \overline{\rho}_{ij}(\boldsymbol{x})\right] \leq \sigma_y^2(\boldsymbol{x})$$

for all the loads defined by the load domain and at all points of the body volume.

The following theorem shows that this necessary condition is also a sufficient one for a structure to shake down.

Theorem 2.1:

Shakedown occurs if there exist a safety factor $a > 1$ and *a time-independent residual stress field* $\overline{\boldsymbol{\rho}}(\boldsymbol{x})$*, statically admissible, such that:*

$$F[a\boldsymbol{\sigma}^e(\boldsymbol{x}, t) + \overline{\boldsymbol{\rho}}(\boldsymbol{x})] \leq \sigma_y^2(\boldsymbol{x}) \;\; \forall \boldsymbol{x} \in V \text{ and } \forall \boldsymbol{P}(t) \in L$$

<u>Proof</u>

At first, the residual stress field $\overline{\rho}_{ij}$ is divided by the safety factor $a > 1$

$$\tilde{\rho}_{ij} = \frac{\overline{\rho}_{ij}}{a}$$

and results to a new residual stress field $\tilde{\rho}_{ij}$ which is also self-equillibrated.

The theorem assumption then becomes

$$F\left[a\sigma_{ij}^{e} + a\tilde{\rho}_{ij}\right] \leq \sigma_y^2$$

Consider the strain energy associated with the difference between the actual residual stress field ρ_{ij}, and the guess for the residual stress field $\tilde{\rho}_{ij}$, which can be calculated as

$$W(t) = \frac{1}{2}\int_V \left(\rho_{ij} - \tilde{\rho}_{ij}\right) C_{ijkl}^{-1} (\rho_{kl} - \tilde{\rho}_{kl}) dV$$

For later reference note that $W(t)$ has to be non-negative, due to positive definiteness of the elasticity tensor.

The rate of change of $W(t)$ can be calculated as

$$\dot{W}(t) = \int_V \left(\rho_{ij} - \tilde{\rho}_{ij}\right) C_{ijkl}^{-1} \dot{\rho}_{kl} dV$$

where the symmetry of elasticity tensor $C_{ijkl}^{-1} = C_{klij}^{-1}$ and the time-independence of the residual stress field $\tilde{\rho}_{ij}$ were used.

Applying the principle of virtual work for the statically admissible self-equillibrated stress field $\rho_{ij} - \tilde{\rho}_{ij}$ and the kinematically admissible residual strain field

$$\int_V \left(\rho_{ij} - \tilde{\rho}_{ij}\right)\left(C_{ijkl}^{-1}\dot{\rho}_{kl} + \dot{\varepsilon}_{ij}^{p}\right) dV = 0$$

On substituting the latter into the former one obtains

$$\dot{W}(t) = -\int_V \left(\rho_{ij} - \tilde{\rho}_{ij}\right)\dot{\varepsilon}_{ij}^{p} dV$$

Making use of the principle of maximum plastic dissipation for the actual stress σ_{ij} state and the state $a\sigma_{ij}^{e} + a\tilde{\rho}_{ij}$ which is safe from the theorem assumption:

$$\left[\sigma_{ij} - \left(a\sigma_{ij}^{e} + a\tilde{\rho}_{ij}\right)\right]\dot{\varepsilon}_{ij}^{p} \geq 0$$

after some rearrangements

$$(a-1)\sigma_{ij}\dot{\varepsilon}_{ij}^{p} \leq \left[a\sigma_{ij} - a\sigma_{ij}^{e} - a\tilde{\rho}_{ij}\right]\dot{\varepsilon}_{ij}^{p} = a\left[\rho_{ij} - \tilde{\rho}_{ij}\right]\dot{\varepsilon}_{ij}^{p}$$

After integrating over the body volume

$$\int_V \sigma_{ij}\dot{\varepsilon}_{ij}^p dV \leq -\frac{\alpha}{\alpha-1}\dot{W}(t)$$

Integration with respect to time leads to

$$\int_0^t \int_V \sigma_{ij}\dot{\varepsilon}_{ij}^p dV\, dt \leq \frac{\alpha}{\alpha-1}[W(0)-W(t)] \leq \frac{\alpha}{\alpha-1}W(0)$$

$$= \frac{\alpha}{\alpha-1}\frac{1}{2}\int_V \tilde{\rho}_{ij}C_{ijkl}^{-1}\tilde{\rho}_{kl}dV$$

This proves the boundedness of the total energy dissipated. As the plastic deformation usually takes place in finite regions, the above inequality implies also the boundedness of the local energy dissipated.

The previous theorem can be extended to the case of bounded kinematic hardening material according to the two surface model proposed by Weichert and Groß-Weege.

Theorem 2.2:

Shakedown occurs if there exist a safety factor $a > 1$, *a time-independent residual stress field* $\overline{\boldsymbol{\rho}}(\boldsymbol{x})$, *statically admissible, and a time-independent field of back-stresses* $\overline{\boldsymbol{\pi}}(\boldsymbol{x})$ *such that:*

$$F[a\boldsymbol{\sigma}^e(\boldsymbol{x},t) + \overline{\boldsymbol{\rho}}(\boldsymbol{x}) - \overline{\boldsymbol{\pi}}(\boldsymbol{x})] \leq \sigma_y^2(\boldsymbol{x}) \;\; \forall \boldsymbol{x} \in V \text{ and } \forall \boldsymbol{P}(t) \in L$$

$$F[\overline{\boldsymbol{\pi}}(\boldsymbol{x})] \leq \left(\sigma_u(\boldsymbol{x}) - \sigma_y(\boldsymbol{x})\right)^2 \;\; \forall \boldsymbol{x} \in V$$

The second inequality can be replaced equivalently by $F[a\boldsymbol{\sigma}^e(\boldsymbol{x},t) + \overline{\boldsymbol{\rho}}(\boldsymbol{x})] \leq \sigma_u^2(\boldsymbol{x})$ as it was stated earlier in section 1.4.3b

It should be noted that, although the two-surface model is based on bounded linear kinematical hardening, Pham has extended it to be nonlinear by adding an additional constraint condition which states that the hysteresis loop must follow a clockwise direction.

Based on the above static theorem, we can find a permanent statically admissible residual stress field in order to obtain a maximum load domain that guarantees safety for every load history. The obtained shakedown load multiplier is generally a lower bound. The shakedown problem can be seen as a maximization issue in nonlinear programming

$$a_{sd}^{-} = \max a$$
$$s.t:$$
$$\begin{cases} F[a\boldsymbol{\sigma}^e(\boldsymbol{x},t) + \overline{\boldsymbol{\rho}}(\boldsymbol{x}) - \overline{\boldsymbol{\pi}}(\boldsymbol{x})] \leq \sigma_y^2(\boldsymbol{x}) & \forall \boldsymbol{x} \in V, \forall \boldsymbol{P}(t) \in L \\ F[\overline{\boldsymbol{\pi}}(\boldsymbol{x})] \leq \left(\sigma_u(\boldsymbol{x}) - \sigma_y(\boldsymbol{x})\right)^2 & \forall \boldsymbol{x} \in V \\ div\overline{\boldsymbol{\rho}}(\boldsymbol{x}) = \boldsymbol{0} & \forall \boldsymbol{x} \in V \\ \overline{\boldsymbol{\rho}}(\boldsymbol{x})\boldsymbol{n} = \boldsymbol{0} & \forall \boldsymbol{x} \in \partial V_\sigma \end{cases}$$

For the perfectly plastic behaviour $(\sigma_u = \sigma_y)$, the back-stresses $\overline{\boldsymbol{\pi}}(\boldsymbol{x})$ are identical zero due to the second inequality.

Melan's original theorem for unbounded kinematic hardening can be also deduced from the previous formulation if $\sigma_u \to \infty$. Then the second inequality is not relevant anymore and the back-stresses $\overline{\boldsymbol{\pi}}(\boldsymbol{x})$ are free variables.

It should be noted that shakedown is independent of the initial state of the structure i.e. initial strains or stresses just like limit analysis.

Let us also notice that all cases with singular elastic stress fields are excluded from the framework of the static shakedown theorem similarly with elastic analysis.

2.4.2 Kinematic shakedown theorem (Koiter)

Using plastic strain fields to formulate shakedown criterion, the kinematic shakedown theorem is the counterpart of the static one. The theorem was given by Koiter. An admissible cycle of the plastic strain field $\Delta\boldsymbol{\varepsilon}^p$ is introduced here, corresponding to a cycle of the displacement field $\Delta\boldsymbol{u}$. The plastic strain rate $\dot{\boldsymbol{\varepsilon}}^p$ may not necessarily be compatible at each instant during the time cycle T but the plastic strain accumulation over the cycle defined below

$$\Delta\boldsymbol{\varepsilon}^p = \int_0^T \dot{\boldsymbol{\varepsilon}}^p dt$$

must be compatible, such that

$$\begin{cases} \Delta\boldsymbol{\varepsilon}^p = \frac{1}{2}(\nabla\Delta\boldsymbol{u} + (\nabla\Delta\boldsymbol{u})^T) & in\ V \\ \Delta\boldsymbol{u} = \boldsymbol{0} & on\ \partial V_u \end{cases}$$

Theorem 2.3:

The structure will not shake down if

$$\int_0^T \left(\int_V \boldsymbol{f}^T \Delta\boldsymbol{u}\, dV + \int_{\partial V_\sigma} \boldsymbol{t}_0{}^T \Delta\dot{\boldsymbol{u}}\, dS \right) dt > \int_0^T \int_V D^p(\dot{\boldsymbol{\varepsilon}}^p) dV\, dt$$

or equivalently

$$\int_0^T \int_V \boldsymbol{\sigma}^e(\boldsymbol{x},t) : \dot{\boldsymbol{\varepsilon}}^p dV\, dt > \int_0^T \int_V D^p(\dot{\boldsymbol{\varepsilon}}^p) dV\, dt$$

<u>Proof</u>

Suppose that the solid <u>does</u> shake down.

Then, from the lower bound shakedown theorem, we know that there exists a time independent self-equilibrated residual stress field $\overline{\rho}_{ij}$, that $\sigma_{ij}^e + \overline{\rho}_{ij}$ lies below yield throughout the cycle.

$$F\left[\sigma_{ij}^e(\boldsymbol{x},t) + \overline{\rho}_{ij}(\boldsymbol{x})\right] \leq \sigma_y^2(\boldsymbol{x})$$

The principle of maximum plastic resistance then shows that

$$\left[\sigma_{ij} - \left(\sigma_{ij}^e + \overline{\rho}_{ij}\right)\right] \dot{\varepsilon}_{ij}^p \geq 0$$

Integrating this expression over the volume of the solid, and the cycle of loading gives

$$\int_0^T \int_V D^p\left(\dot{\varepsilon}_{ij}^p\right) dV\, dt - \int_0^T \int_V \sigma_{ij}^e \dot{\varepsilon}_{ij}^p dV\, dt - \int_0^T \int_V \overline{\rho}_{ij} \dot{\varepsilon}_{ij}^p dV\, dt \geq 0$$

Finally, reversing the order of integration in the last integral and using the principle of virtual work, we see that

$$\int_V \int_0^T \overline{\rho}_{ij} \dot{\varepsilon}_{ij}^p dt\, dV = \int_V \overline{\rho}_{ij} \Delta\varepsilon_{ij}^p dV = 0$$

Substituting back in the inequality

$$\int_0^T \int_V D^p\left(\dot{\varepsilon}_{ij}^p\right) dV\, dt \geq \int_0^T \int_V \sigma_{ij}^e \dot{\varepsilon}_{ij}^p dV\, dt$$

which contradicts the theorem assumption and proves the kinematic shakedown theorem.

Based on the kinematic theorem, an upper bound of the shakedown limit load multiplier can be computed. The shakedown problem can be seen as a mathematical minimization problem of nonlinear programming

$$a_{sd}^{+} = \min a$$
$$s.t:$$
$$\begin{cases} \Delta\boldsymbol{\varepsilon}^{p} = \int_{0}^{T} \dot{\boldsymbol{\varepsilon}}^{p} dt \\ \Delta\boldsymbol{\varepsilon}^{p} = \frac{1}{2}(\nabla\Delta\boldsymbol{u} + (\nabla\Delta\boldsymbol{u})^{T}) & in\ V \\ \Delta\boldsymbol{u} = \boldsymbol{0} & on\ \partial V_{u} \end{cases}$$

Chapter 3: **Numerical Formulations**

3.1 Description of strategy

There have been developed several numerical procedures, for the investigation of whether a structure with a given loading domain will shakedown under any possible loading path contained in the loading domain L. Over the past few years, the investigators have been interested in the so called Direct Methods, which usually try to find a residual time-independent field according to Melan's Theorem. These methods have the advantage of avoiding to keep track of the field variables and searching directly for a possible shakedown state. They attract a lot of attention, because they are usually very efficient computationally, due to the avoidance step-by step analysis. Such methods are:

- Interior Point Optimization
- Selective Algorithm
- Linear Matching Method (LMM)
- Residual Stress Decomposition Method (RSDM)

The main drawback of Direct Methods is that they fail to give the shakedown displacements, which could be unacceptable for the structure serviceability, so step-by-step solutions must be also used, at least complementary.

The solution strategy which is adopted in this work is step-by-step calculations for special loading histories. This solution strategy was proposed by Borkowski and Kleiber (1980).

In section 3.2, it will be proven that it is sufficient to check the structure over a cyclic load path which contains all the corners of L. As existing computer programs are developed for the case of proportional load variations, it seems practical to prescribe each load cycle as a sequence of proportional loading steps passing through every vertex.

Convergence of plastic deformations indicates shakedown in any load program within L, divergence—a possibility of low-cycle fatigue and/or incremental collapse.

Several loading cycles must be run on the computer with the plastic strain increments and the dissipated energy monitored. If the latter ceases to grow after a finite number of cycles, then the structure has adapted itself to the critical cyclic load and hence is able to shake down under any variable loading contained in L. On the contrary, if the dissipated energy grows steadily, then the adaptation is impossible.

Further inspection of the signs and magnitudes of plastic strain increments shows whether this is due to incremental collapse or alternating plasticity or both.

A more involved procedure enables an estimate to be made of the magnitude of the safety factor against inadaptation. Namely, if shakedown takes place for a given load domain L, let us enlarge it proportionally by a factor $a > 1$ so as to obtain a new domain aL. Then the above-presented

procedure is repeated for the enlarged domain aL. If plastic deformations still converge, a higher multiplier a' is to be applied until inadaptation sets in. Then the actual safety factor is bounded as follows

$$a < \mu < \alpha'$$

It should be emphasized that the above procedure can also be utilized in the experimental evaluation of shakedown loads.

Notice that the accuracy of the method may be strongly influenced by a possible error accumulation in subsequent load cycles.

The crucial point is to decide how many cycles must be simulated to decide whether the structure reaches shakedown. It should be clear that, if the time history consists of very few cycles, then this leads to a safe estimate, since inadaptation does not exclude the possibility of shakedown after more cycles.

The number of necessary cycles for shakedown are greatly affected by the hardening model, which is adopted.

- Isotropic Hardening: It is not suitable for modelling of cyclic behavior, because it predicts that for every loading below the limit load the yield function will expand until an elastic state is achieved, which means shakedown. Thus, this hardening law is not capable of modelling alternating plasticity nor incremental collapse.
- Alternating plasticity: This phenomenon is characteristic of symmetric stress- or strain-controlled experiments. Soft or annealed metals tend to harden toward a stable limit, and initially hardened metals tend to soften. Figure 3.1 illustrates the behavior of a metal that hardens under prescribed symmetric strain cycles. The kinematic hardening component of the models used alone predicts plastic shakedown after one stress cycle. The combination of the isotropic component together with the nonlinear kinematic component predicts shakedown after several cycles.

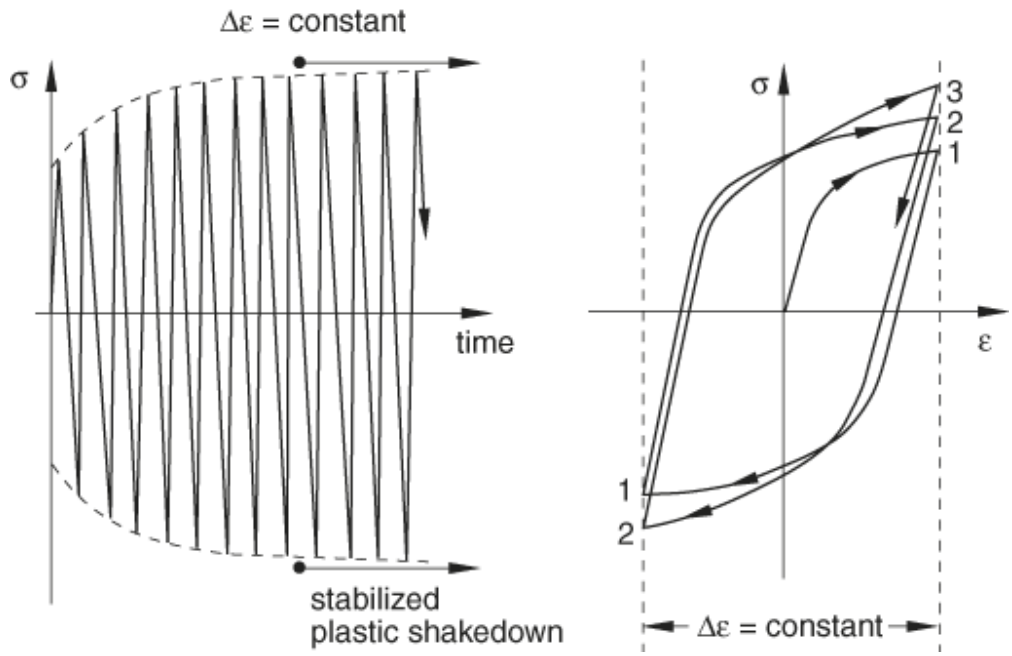

Figure 3.1: Plastic Shakedown

- Incremental collapse: Unsymmetric cycles of stress between prescribed limits will cause progressive "creep" or "ratchetting" in the direction of the mean stress (Figure 3.2). Typically, transient ratchetting is followed by stabilization (zero ratchet strain) for low mean stresses, while a constant increase in the accumulated ratchet strain is observed at high mean stresses. The nonlinear kinematic hardening component, used without the isotropic hardening component, predicts constant ratchet strain. The prediction of ratchetting is improved by adding isotropic hardening, in which case the ratchet strain may decrease until it becomes constant. However, in general the nonlinear hardening model with a single back-stress predicts a too significant ratchetting effect. The multilinear kinematic hardening model cannot predict this effect.

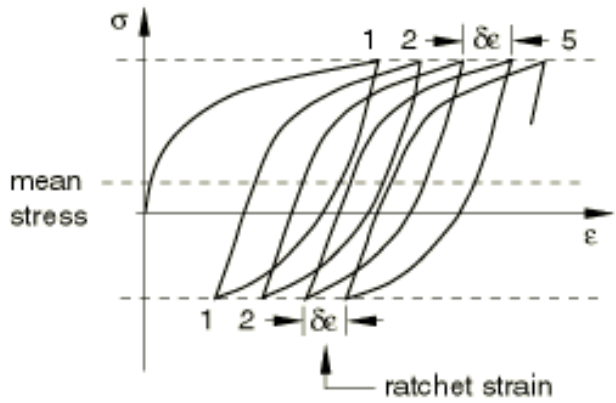

Figure 3.2: Plastic Shakedown

3.2 Discretization of the load domain

Let L be a load domain containing any possible load which acts on the structure V. Any load $\boldsymbol{P}(x,t) \in L$ could be specified by a variable t. For a variable loading the load domain contains infinitely many loads (for a monotonic load in limit analysis it is presented by one single load.)

In shakedown analysis all the non-countable loads $\boldsymbol{P}(x,t)$ must be verified. This situation leads to difficulties because of the infinite load histories that must be checked.
Fortunately, these difficulties can be overcome with the help of the following theorem introduced by König and Kleiber.

Before the statement of the theorem, the property of a cyclic load path is given:

$$\mu_k(t) = \mu_k(t+T), \qquad k = 1, \dots, n$$

i.e. all the load factors are in this case periodic functions of time with a common period T.

Next, an important property of the yield function, which is important for the proof of the theorem 3.1, is stated that follows from its convexity

$$f(\beta\boldsymbol{\sigma}_1 + (1-\beta)\boldsymbol{\sigma}_2) \leq \beta f(\boldsymbol{\sigma}_1) + (1-\beta) f(\boldsymbol{\sigma}_2)$$

where $\boldsymbol{\sigma}_1, \boldsymbol{\sigma}_2$ are safe stress states and $0 \leq \beta \leq 1$.

The following theorem is useful in the numerical investigation whether a given load domain will lead to shakedown or not.

Theorem 3.1:

A structure shakes down under a cyclic loading containing all the vertices of the convex loading domain L if and only if it shakes down for any loading path contained in L.

<u>Proof</u>

Consider a stress point at some cyclic loading path inside the convex domain. The elastic solution may be written at this point as a linear combination of the elastic solutions at its vertices due to convexity of the load domain:

$$\boldsymbol{\sigma}^e(\boldsymbol{x},t) = \sum_{k=1}^{n} \mu_k(t)\boldsymbol{\sigma}_k^e(\boldsymbol{x})$$

$$\sum_{k=1}^{n} \mu_k(t) = 1 \;\; and \;\; \mu_k(t) \geq 0$$

where $\boldsymbol{\sigma}_k^e$ are the elastic stresses at each vertex of this domain

Since by the hypothesis, a cyclic loading that passes through the vertices of the loading domain at different time points causes the structure to shake down, according to Melan's

theorem, a residual stress $\overline{\boldsymbol{\rho}}$ constant in time, and therefore common at all the vertices, will exist, such that the total stress at each vertex will be a safe state of stress:

$$f\left(\boldsymbol{\sigma}_k^e(\boldsymbol{x}) + \overline{\boldsymbol{\rho}}(\boldsymbol{x})\right) \leq 0, \qquad k = 1, \dots, n$$

This residual stress may be combined with $\boldsymbol{\sigma}^e(\boldsymbol{x}, t)$ to give:

$$f\left(\boldsymbol{\sigma}^e(\boldsymbol{x}, t) + \overline{\boldsymbol{\rho}}(\boldsymbol{x})\right) = f\left(\sum_{k=1}^{n} \mu_k(t)\boldsymbol{\sigma}_k^e(\boldsymbol{x}) + \overline{\boldsymbol{\rho}}(\boldsymbol{x})\right)$$
$$= f\left(\sum_{k=1}^{n} \mu_k(t)\boldsymbol{\sigma}_k^e(\boldsymbol{x}) + \overline{\boldsymbol{\rho}}(\boldsymbol{x}) \sum_{k=1}^{n} \mu_k(t)\right)$$

using the property of the coefficients $\mu_k(t)$

By grouping them, the above expression becomes

$$f\left(\boldsymbol{\sigma}^e(\boldsymbol{x}, t) + \overline{\boldsymbol{\rho}}(\boldsymbol{x})\right) = f\left(\sum_{k=1}^{n} \mu_k(t)\left(\boldsymbol{\sigma}_k^e(\boldsymbol{x}) + \overline{\boldsymbol{\rho}}(\boldsymbol{x})\right)\right) \leq \sum_{k=1}^{n} \mu_k(t)\, f\left(\boldsymbol{\sigma}_k^e(\boldsymbol{x}) + \overline{\boldsymbol{\rho}}(\boldsymbol{x})\right)$$

The above inequality is justified through the use of the generalized form of the convexity inequality of the yield function, often called Jensen's inequality, which may be proved by induction.

Thus, we conclude:

$$f\left(\boldsymbol{\sigma}^e(\boldsymbol{x}, t) + \overline{\boldsymbol{\rho}}(\boldsymbol{x})\right) \leq 0$$

because the safety condition is satisfied at each one of the load vertices and the coefficients $\mu_k(t)$ are non-negative.

The last inequality means that the condition of Melan's theorem is satisfied for every $\boldsymbol{P}(x, t) \in L$, so shakedown occurs for all possible load histories contained in L.

The inverse statement also holds because the case of a cyclic load history containing all the vertices of the convex loading domain L is a special case of the possible load histories contained in the domain L.

This theorem can be demonstrated via the load domain of two variable loads P_1 and P_2 as in Fig. 3.3a and Fig. 3.3b respectively.

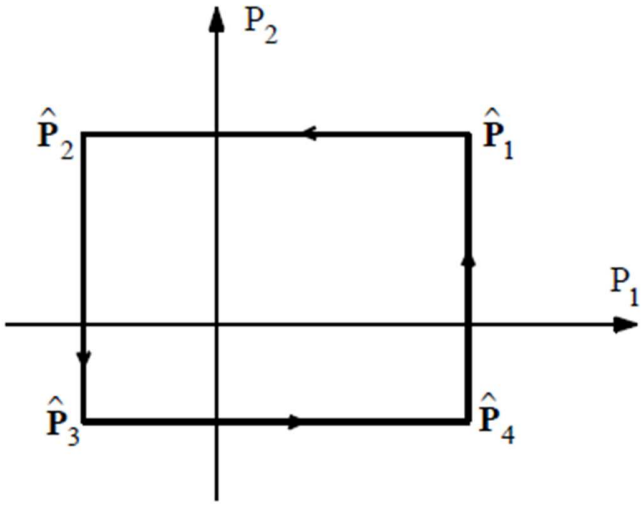

Figure 3.3a: Cyclic load path containing all vertices of L

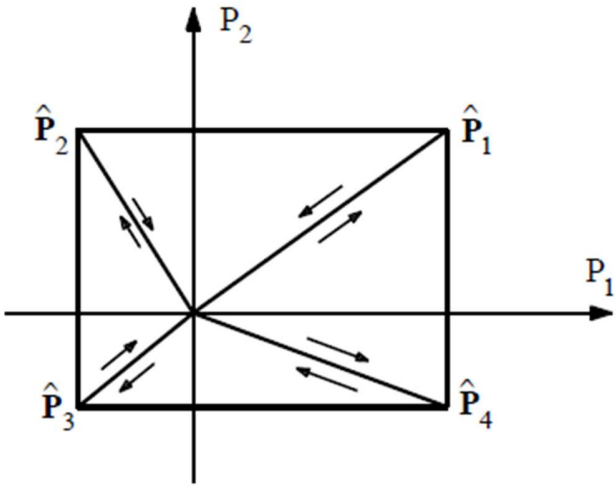

Figure 3.3b: Cyclic load path consisting of loading- unloading from the origin to each load vertex

A 2-D dimensional loading cuboid is a rectangle, i.e. $s = 4\ (2^2)$e.. For a 3-D loading domain, $s = 8\ (2^3)$. For an n-dimensional loading domain (n-cuboid) one can envisage that the number of vertices will be equal to the combination of the loads in all possible ways.

$$m = \binom{n}{0} + \binom{n}{1} + \cdots + \binom{n}{k} + \cdots + \binom{n}{n} = \sum_{k=0}^{n} \binom{n}{k} = 2^n$$

where $\binom{n}{k} = \frac{n!}{k!\,(n-k)!}$ is the binomial coefficient and the expression above is a standard binomial formula.

The theorem 3.1 holds for convex load domains and convex yield surfaces, which permits to consider one cyclic load path instead of all loading history. This means that the cyclic loading could be described by a finite number of load cases $\widehat{\boldsymbol{P}}_k$.

These n loads P_k vary in a given interval $\left[P_k^{min}, P_k^{max}\right]$, e.g. for a cyclic pressure load, the pressure is bounded by minimum and maximum pressure.

By defining the load cases $\widehat{\boldsymbol{P}}_1, \cdots, \widehat{\boldsymbol{P}}_m$ via the load limits in each case, any load $\boldsymbol{P}(x,t) \in L$ in a convex load space L is given as unique convex combination of the $\widehat{\boldsymbol{P}}_k(\boldsymbol{x})$, as follows

$$\boldsymbol{P}(\boldsymbol{x},t) = \sum_{k=1}^{m} \delta(t_k)\, \widehat{\boldsymbol{P}}_k(\boldsymbol{x})$$

with:

$$\delta(t_k) = \begin{cases} 1 & if\ t = t_k \\ 0 & if\ t \neq t_k \end{cases}$$

and

$$\widehat{\boldsymbol{P}}_k(\boldsymbol{x}) = \sum_{k=1}^{n} \mu_k P_k^0$$

3.3 Finite Element Solution

In order to solve the elastoplastic step-by-step problem, the Finite Element Method is utilized, which is widely used for nonlinear problems.

Following common usage in the finite-element literature, in the exposition that follows the tensor notation is abandoned in favour of matrix and vector notation. The following standard conventions are used for 2nd order tensors

$$\boldsymbol{\varepsilon} = \begin{bmatrix} \varepsilon_{11} \\ \varepsilon_{22} \\ \varepsilon_{33} \\ 2\varepsilon_{12} \\ 2\varepsilon_{13} \\ 2\varepsilon_{23} \end{bmatrix}, \qquad \boldsymbol{\varepsilon^p} = \begin{bmatrix} \varepsilon_{11}^p \\ \varepsilon_{22}^p \\ \varepsilon_{33}^p \\ 2\varepsilon_{12}^p \\ 2\varepsilon_{13}^p \\ 2\varepsilon_{23}^p \end{bmatrix}, \qquad \boldsymbol{\sigma} = \begin{bmatrix} \sigma_{11} \\ \sigma_{22} \\ \sigma_{33} \\ \sigma_{12} \\ \sigma_{13} \\ \sigma_{23} \end{bmatrix}$$

and for 4th order tensors $\boldsymbol{C} = \begin{bmatrix} C_{1111} & C_{1122} & C_{1133} & C_{1112} & C_{1113} & C_{1123} \\ & C_{2222} & C_{2233} & C_{2212} & C_{2213} & C_{2223} \\ & & C_{3333} & C_{3312} & C_{3313} & C_{3323} \\ & & & C_{1212} & C_{1213} & C_{1223} \\ & & & & C_{1313} & C_{1323} \\ & & & & & C_{2323} \end{bmatrix}$

Due to the above notations, contraction between second-order tensors is replaced by a dot product, and application of a fourth-order tensor to a second-order tensor reduces to a matrix transformation; for instance

$$\boldsymbol{\sigma}:\boldsymbol{\varepsilon} = \sigma_{ij}\varepsilon_{ij} \rightarrow \boldsymbol{\sigma}\cdot\boldsymbol{\varepsilon} = \boldsymbol{\sigma}^T\boldsymbol{\varepsilon}$$
$$\boldsymbol{\sigma} = \boldsymbol{C}:\boldsymbol{\varepsilon}^e \rightarrow \boldsymbol{\sigma} = \boldsymbol{C}\boldsymbol{\varepsilon}^e$$

The finite-element formulation is based on *discontinuous interpolations* of stress and strain over a typical element V^e of a discretization $V \approx \bigcup_{e=1}^{N} V^e$

3.3.1 Displacement field interpolation

The displacement field is discretized by choosing to calculate the displacement field at a set of n nodes. The coordinates of these special points are denoted by $\boldsymbol{x}^e$.The unknown displacement vector at each nodal point will be denoted by $\boldsymbol{u}^e$.

The displacement increment and the virtual displacement are interpolated in the usual way.

$$\Delta\boldsymbol{u}(\boldsymbol{x}) = \boldsymbol{N}(\boldsymbol{x})\Delta\boldsymbol{u}^e, \qquad \delta\boldsymbol{u}(\boldsymbol{x}) = \boldsymbol{N}(\boldsymbol{x})\delta\boldsymbol{u}^e$$

where $\boldsymbol{N}(\boldsymbol{x})$ is the shape function matrix

$$\boldsymbol{N}(\boldsymbol{x}) = \begin{bmatrix} N_1(\boldsymbol{x}) & 0 & 0 & & N_n(\boldsymbol{x}) & 0 & 0 \\ 0 & N_1(\boldsymbol{x}) & 0 & \cdots & 0 & N_n(\boldsymbol{x}) & 0 \\ 0 & 0 & N_1(\boldsymbol{x}) & & 0 & 0 & N_n(\boldsymbol{x}) \end{bmatrix}$$

The shape functions $N_i(\boldsymbol{x})$ have the following property

$$N_i(\boldsymbol{x}^j) = \delta_{ij} = \begin{cases} 1, & if\ \boldsymbol{x}^i = \boldsymbol{x}^j \\ 0, & if\ \boldsymbol{x}^i \neq \boldsymbol{x}^j \end{cases}$$

and their choice is very important for the accuracy of the method.

The vector of global displacements is defined as

$$\boldsymbol{u} = [u_1^1 \quad u_2^1 \quad u_3^1 \quad \cdots \quad u_1^n \quad u_2^n \quad u_3^n]^T$$

The strain field results from the displacement field using the compatibility equation

$$\boldsymbol{\varepsilon}(x) = \boldsymbol{L}\boldsymbol{u}(x) = \boldsymbol{L}\boldsymbol{N}(\boldsymbol{x})\boldsymbol{u}^e = \boldsymbol{B}(\boldsymbol{x})\boldsymbol{u}^e$$

where $\boldsymbol{L}$ is the linear operator of the compatibility equation.

The last matrix $\boldsymbol{B}(\boldsymbol{x})$ is called the strain matrix and its elements are the first derivatives of the shape functions.

$$\boldsymbol{B}(\boldsymbol{x}) = \begin{bmatrix} N_{1,x} & 0 & 0 & & N_{n,x} & 0 & 0 \\ 0 & N_{1,y} & 0 & & 0 & N_{n,y} & 0 \\ 0 & 0 & N_{1,z} & & 0 & 0 & N_{n,z} \\ N_{1,y} & N_{1,x} & 0 & \cdots & N_{n,y} & N_{n,x} & 0 \\ N_{1,z} & 0 & N_{1,x} & & N_{n,z} & 0 & N_{n,x} \\ 0 & N_{1,z} & N_{1,y} & & 0 & N_{n,z} & N_{n,y} \end{bmatrix}$$

3.3.2 Principle of virtual work

As in all FEM analysis, the stress equilibrium equation is replaced by the equivalent statement of the principle of virtual work.

For all virtual displacement fields $\delta\boldsymbol{u}(\boldsymbol{x})$ that are kinematically compatible

$$\int_V \delta\boldsymbol{\varepsilon}^T(\boldsymbol{x})\boldsymbol{\sigma}dV - \int_V \delta\boldsymbol{u}^T(\boldsymbol{x})\boldsymbol{b}dV - \int_{\partial V_\sigma} \delta\boldsymbol{u}^{\boldsymbol{T}}(\boldsymbol{x})\boldsymbol{t}dS = 0$$

Interpolation of the virtual displacement field gives

$$\delta\boldsymbol{u}^T\left(\int_V \boldsymbol{B}^T\boldsymbol{\sigma}dV - \int_V \boldsymbol{N_f}^T\boldsymbol{f}dV - \int_{\partial V_\sigma} \boldsymbol{N_S}^T\boldsymbol{t_0}dS\right) = 0$$

The last equation must be satisfied for every kinematically compatible field $\delta\boldsymbol{u}$, so the equation reduces to

$$\int_V \boldsymbol{B}^T\boldsymbol{\sigma}dV - \int_V \boldsymbol{N_f}^T\boldsymbol{f}dV - \int_{\partial V_\sigma} \boldsymbol{N_S}^T\boldsymbol{t_0}dS = 0$$

Substituting the stress-strain material law $\boldsymbol{\sigma} = \boldsymbol{C\varepsilon}$ and using the same interpolation $\boldsymbol{\varepsilon} = \boldsymbol{Bu}$ for the actual strain field

$$\left(\int_V \boldsymbol{B}^T\boldsymbol{CB}dV\right)\boldsymbol{u} = \boldsymbol{q}_f + \boldsymbol{q}_t$$

The last expression has the form

$$\boldsymbol{Ku} = \boldsymbol{f}^{ext}$$

with stiffness matrix $\boldsymbol{K} = \int_V \boldsymbol{B}^T\boldsymbol{CB}dV$

and nodal loads$\boldsymbol{f}_f^{ext} = \int_V \boldsymbol{N_f}^T\boldsymbol{f}dV$ due to body forces and $\boldsymbol{f}_t^{ext} = \int_{\partial V_\sigma} \boldsymbol{N_S}^T\boldsymbol{t_0}dS$ due to surface tractions.

3.3.3 Isoparametric elements

In case of complex geometry, where it is not possible to generate a mess with perfect cubic elements, the concept of isoparametric elements is utilized. They are based on the use of a second coordinate system, which is defined by a mapping of the cartesian, called the natural system.

The mapping of the natural to the cartesian system is defined as

$$\boldsymbol{x} = \boldsymbol{x}(\boldsymbol{\xi})$$

where $\boldsymbol{x}$ are the Cartesian coordinates and $\boldsymbol{\xi}$ are the natural coordinates.

The inverse mapping is $\boldsymbol{\xi} = \boldsymbol{\xi}(\boldsymbol{x})$

Then the Jacobian of the transformation

$$\boldsymbol{J} = \frac{\partial \boldsymbol{x}}{\partial \boldsymbol{\xi}} = \begin{bmatrix} \frac{\partial x}{\partial \xi} & \frac{\partial y}{\partial \xi} & \frac{\partial z}{\partial \xi} \\ \frac{\partial x}{\partial \eta} & \frac{\partial y}{\partial \eta} & \frac{\partial z}{\partial \eta} \\ \frac{\partial x}{\partial \zeta} & \frac{\partial y}{\partial \zeta} & \frac{\partial z}{\partial \zeta} \end{bmatrix}$$

must satisfy $det\boldsymbol{J} > 0$ in order the mapping to be unique.

The derivatives can be taken with respect to the natural system instead of the cartesian and vice versa by the chain rule

$$\frac{\partial}{\partial \boldsymbol{x}} = \boldsymbol{J}\frac{\partial}{\partial \boldsymbol{\xi}} \quad or \quad \frac{\partial}{\partial \boldsymbol{\xi}} = \boldsymbol{J}^{-1}\frac{\partial}{\partial \boldsymbol{x}}$$

The shape functions can be conveniently defined in the natural system.

For example, for the case of linear hexahedral 8-node elements the shape functions are:

$$N_i = \frac{1}{8}(1 + \xi\xi_i)(1 + \eta\eta_i)(1 + \zeta\zeta_i), \qquad with\ \xi_i, \eta_i, \zeta_i \in \{-1,1\}$$

In order to obtain the strain matrix, the derivatives of the shape functions with respect to the natural coordinates are necessary.

The strain matrix takes the form

$$\boldsymbol{\varepsilon}(x) = \begin{bmatrix} \varepsilon_{11} \\ \varepsilon_{22} \\ \varepsilon_{33} \\ 2\varepsilon_{12} \\ 2\varepsilon_{13} \\ 2\varepsilon_{23} \end{bmatrix} = \begin{bmatrix} \dfrac{\partial u}{\partial x} \\ \dfrac{\partial v}{\partial y} \\ \dfrac{\partial w}{\partial z} \\ \dfrac{\partial u}{\partial y} + \dfrac{\partial v}{\partial x} \\ \dfrac{\partial u}{\partial z} + \dfrac{\partial w}{\partial x} \\ \dfrac{\partial v}{\partial z} + \dfrac{\partial w}{\partial y} \end{bmatrix} = \overbrace{\begin{bmatrix} \boldsymbol{J}_{1k}^{-1} & & \\ & \boldsymbol{J}_{2k}^{-1} & \\ & & \boldsymbol{J}_{3k}^{-1} \\ \boldsymbol{J}_{2k}^{-1} & \boldsymbol{J}_{1k}^{-1} & \\ \boldsymbol{J}_{3k}^{-1} & & \boldsymbol{J}_{1k}^{-1} \\ & \boldsymbol{J}_{3k}^{-1} & \boldsymbol{J}_{2k}^{-1} \end{bmatrix}}^{\boldsymbol{B}_1} \begin{bmatrix} \dfrac{\partial u}{\partial \xi} \\ \dfrac{\partial u}{\partial \eta} \\ \dfrac{\partial u}{\partial \zeta} \\ \dfrac{\partial v}{\partial \xi} \\ \dfrac{\partial v}{\partial \eta} \\ \dfrac{\partial v}{\partial \zeta} \\ \dfrac{\partial w}{\partial \xi} \\ \dfrac{\partial w}{\partial \eta} \\ \dfrac{\partial w}{\partial \zeta} \end{bmatrix}$$

where the $\boldsymbol{J}_{ik}^{-1}$ means the ith row of the inverse Jacobian matrix.

The components of the inverse of the Jacobian are

$$\boldsymbol{J}^{-1} = \begin{bmatrix} J_{11}^{-1} & J_{12}^{-1} & J_{13}^{-1} \\ J_{21}^{-1} & J_{22}^{-1} & J_{23}^{-1} \\ J_{31}^{-1} & J_{32}^{-1} & J_{33}^{-1} \end{bmatrix} = \frac{1}{detJ} \begin{bmatrix} \begin{vmatrix} J_{22} & J_{23} \\ J_{32} & J_{33} \end{vmatrix} & -\begin{vmatrix} J_{21} & J_{23} \\ J_{31} & J_{33} \end{vmatrix} & \begin{vmatrix} J_{21} & J_{22} \\ J_{31} & J_{32} \end{vmatrix} \\ -\begin{vmatrix} J_{12} & J_{13} \\ J_{32} & J_{33} \end{vmatrix} & \begin{vmatrix} J_{11} & J_{13} \\ J_{31} & J_{33} \end{vmatrix} & -\begin{vmatrix} J_{11} & J_{12} \\ J_{31} & J_{32} \end{vmatrix} \\ \begin{vmatrix} J_{12} & J_{13} \\ J_{22} & J_{23} \end{vmatrix} & -\begin{vmatrix} J_{11} & J_{13} \\ J_{21} & J_{23} \end{vmatrix} & \begin{vmatrix} J_{11} & J_{12} \\ J_{21} & J_{22} \end{vmatrix} \end{bmatrix}$$

$$= \frac{1}{det\boldsymbol{J}} \begin{bmatrix} J_{22}J_{33} - J_{23}J_{32} & J_{23}J_{31} - J_{21}J_{33} & J_{21}J_{22} - J_{31}J_{32} \\ J_{13}J_{32} - J_{12}J_{33} & J_{11}J_{33} - J_{13}J_{31} & J_{12}J_{31} - J_{11}J_{32} \\ J_{12}J_{23} - J_{13}J_{22} & J_{13}J_{21} - J_{11}J_{23} & J_{11}J_{22} - J_{12}J_{21} \end{bmatrix}$$

Using the same shape functions for the interpolation of the coordinates

$$\boldsymbol{x} = \boldsymbol{N}\boldsymbol{x}^{\boldsymbol{e}}$$

Then, the Jacobian can be calculated as

$$\boldsymbol{J} = \frac{\partial \boldsymbol{x}}{\partial \boldsymbol{\xi}} = \begin{bmatrix} \frac{\partial x}{\partial \xi} & \frac{\partial y}{\partial \xi} & \frac{\partial z}{\partial \xi} \\ \frac{\partial x}{\partial \eta} & \frac{\partial y}{\partial \eta} & \frac{\partial z}{\partial \eta} \\ \frac{\partial x}{\partial \zeta} & \frac{\partial y}{\partial \zeta} & \frac{\partial z}{\partial \zeta} \end{bmatrix} = \begin{bmatrix} N_{i,\xi} x_i & N_{i,\xi} y_i & N_{i,\xi} z_i \\ N_{i,\eta} x_i & N_{i,\eta} y_i & N_{i,\eta} z_i \\ N_{i,\zeta} x_i & N_{i,\zeta} y_i & N_{i,\zeta} z_i \end{bmatrix}$$

Interpolating the displacements over the element

$$\boldsymbol{u} = \boldsymbol{N}\boldsymbol{u}^{\boldsymbol{e}}$$

$$\begin{bmatrix} \frac{\partial u}{\partial \xi} \\ \frac{\partial u}{\partial \eta} \\ \frac{\partial u}{\partial \zeta} \\ \frac{\partial v}{\partial \xi} \\ \frac{\partial v}{\partial \eta} \\ \frac{\partial v}{\partial \zeta} \\ \frac{\partial w}{\partial \xi} \\ \frac{\partial w}{\partial \eta} \\ \frac{\partial w}{\partial \zeta} \end{bmatrix} = \overbrace{\begin{bmatrix} N_{1,\xi} & & & & & N_{n,\xi} & & \\ N_{1,\eta} & & & & & N_{n,\eta} & & \\ N_{1,\zeta} & & & & & N_{n,\zeta} & & \\ & N_{1,\xi} & & & & & N_{n,\xi} & \\ & N_{1,\eta} & & \cdots & & & N_{n,\eta} & \\ & N_{1,\zeta} & & & & & N_{n,\zeta} & \\ & & N_{1,\xi} & & & & & N_{n,\xi} \\ & & N_{1,\eta} & & & & & N_{n,\eta} \\ & & N_{1,\zeta} & & & & & N_{n,\zeta} \end{bmatrix}}^{\boldsymbol{B}_2} \begin{bmatrix} u_1^1 \\ u_2^1 \\ u_3^1 \\ \vdots \\ u_1^n \\ u_2^n \\ u_3^n \end{bmatrix}$$

Then strain matrix is computed as

$$\boldsymbol{B}(\boldsymbol{\xi}) = \boldsymbol{B}_1 \boldsymbol{B}_2$$

The integral transformation from the cartesian to the natural coordinate system is done with the following way

$$\int_{V_e} \boldsymbol{F}(\boldsymbol{x}) dV_e = \int_{V_\xi} \boldsymbol{F}(\boldsymbol{\xi})\, det\boldsymbol{J}\, dV_\xi = \int_{-1}^{1} \int_{-1}^{1} \int_{-1}^{1} \boldsymbol{F}(\xi, \eta, \zeta)\, det\boldsymbol{J}\, d\xi d\eta d\zeta$$

For example, the stiffness element matrix is calculated as

$$\boldsymbol{k^e} = \int_{V_e} \boldsymbol{B}^T \boldsymbol{C}\boldsymbol{B} dV_e = \int_{-1}^{1}\int_{-1}^{1}\int_{-1}^{1} \boldsymbol{B}^T(\xi,\eta,\zeta)\boldsymbol{C}(\xi,\eta,\zeta)\boldsymbol{B}(\xi,\eta,\zeta)\, det\boldsymbol{J}\, d\xi d\eta d\zeta$$

3.3.4 Numerical Integration

The analytical calculation of the integrals involved in the finite element equations is very difficult, or sometimes even impossible, especially in the case of isoparametric elements.

In order to overcome this problem, the integral calculation is done numerically using the Gauss-Legendre quadrature rule. According to this rule, the integral on the normalized domain $[-1,1]$ can be approximated as

$$\int_{-1}^{1} f(x)dx = \sum_{i=1}^{NGP} w_i f(x_i)$$

where NGP are the number of sample points (Gauss points), w_i are the integration weights and x_i are the points where the function is computed.

The choice of quadrature weights w_i and quadrature nodes x_i is very important for the accuracy of the calculation. In the Gauss-Legendre quadrature the unique choice that allows the quadrature rule to integrate degree $2NGP - 1$ polynomials exactly is used.

It can be proven that the optimal choice for the Gauss nodes x_i are the roots of the Legengre polynomial $P_{NGP}(x)$ of degree NGP.

The corresponding weights are given by the formula

$$w_i = \frac{2}{(1 - x_i^2)[P'_{NGP}(x_i)]^2}$$

The integration over the volume of the element can be done as follows

$$\int_{V_e} \boldsymbol{F}(\boldsymbol{x})dV_e = \int_{-1}^{1}\int_{-1}^{1}\int_{-1}^{1} \boldsymbol{F}(\xi,\eta,\zeta)\, det\boldsymbol{J}\, d\xi d\eta d\zeta = \sum_{i=1}^{NGP}\sum_{j=1}^{NGP}\sum_{k=1}^{NGP} w_i w_j w_k\, \boldsymbol{F}\left(\xi_i,\eta_j,\zeta_k\right) det\boldsymbol{J}$$

where the number of integration points was kept the same for every dimension without that be restrictive.

3.3.5 Linear system formulation

The global stiffness matrix is created by the assemblage of the element stiffness matrices to the correct position of the global one. This is done by assigning the components of the element stiffness matrix $\boldsymbol{k}^e$ to the corresponding position of the global matrix.

$$\boldsymbol{K} = \bigwedge_{e=1}^{N} \boldsymbol{k}^e$$

where $\bigwedge$ is the assembly operator.

In a similar way, the vector of external nodal forces is assembled, taking the contributions of all the elements of the solid.

$$\boldsymbol{f}^{\boldsymbol{ext}} = \bigwedge_{e=1}^{N} \boldsymbol{f}_e^{ext}$$

Then, the nodal displacements must satisfy

$$\boldsymbol{K}\boldsymbol{u} = \boldsymbol{f}^{\boldsymbol{ext}}$$

to ensure equilibrium.

However, the last expression is not invertible because the stiffness matrix $\boldsymbol{K}$ is singular.

The linear system can be solved only after the enforcement of the boundary conditions.

3.3.6 Newton-Raphson method

The solution of the system $\boldsymbol{K}\boldsymbol{u} = \boldsymbol{f}^{\boldsymbol{ext}}$ gives the nodal displacements of the mesh. If the problem was linear then the components of the stiffness matrix would be constant values. However, because of the material nonlinearity, the stiffness matrix $\boldsymbol{K}$ depends on the nodal displacements $\boldsymbol{u}$. In order to solve the nonlinear system of equations, the Newton-Raphson method is utilized, which is an iterative numerical method.

The virtual work equation has the form

$$\boldsymbol{r} = \int_V \boldsymbol{B}^T \boldsymbol{\sigma} dV - \int_V \boldsymbol{N_f}^T \boldsymbol{f} dV - \int_{\partial V_\sigma} \boldsymbol{N_S}^T \boldsymbol{t_0} dS = 0$$

or equivalently

$$\boldsymbol{r} = \boldsymbol{f}^{\boldsymbol{int}}(\boldsymbol{u}) - \boldsymbol{f}^{\boldsymbol{ext}} = 0$$

where $\boldsymbol{q}$ is the external forces nodal vector and $\boldsymbol{F}^{int}$ is the internal forces nodal vector.

The last one is calculated as

$$\boldsymbol{f}^{\boldsymbol{int}} = \bigwedge_{e=1}^{N} \int_{V_e} \boldsymbol{B}^T \boldsymbol{\sigma} dV_e$$

The total load is divided into small increments $\Delta \boldsymbol{u} = \boldsymbol{u}_{n+1} - \boldsymbol{u}_n$, in order for the linearity assumption to be valid on the interval $[t_n, t_{n+1}]$. It should be noted that time t does not insert as a real variable into the problem, but is used to represent the load increments.

The incremental procedure is applied in the following way.

Suppose that n is a step where equilibrium has been established. This means that nodal displacements $\boldsymbol{u}_n$, stresses $\boldsymbol{\sigma}_n$, and strains $\boldsymbol{\varepsilon}_n$ are known, so the internal forces nodal vector $\boldsymbol{f}_n^{int}$ is also known.

Then, a new equilibrium is pursued through iterations for the incremental step n+1. The iterative procedures starts by taking as first approximation the quantities from the previous converged state.

$$\boldsymbol{u}_{n+1}^0 = \boldsymbol{u}_n, \qquad \boldsymbol{f}^{\boldsymbol{int}}(\boldsymbol{u}_{n+1}^0) = \boldsymbol{f}^{\boldsymbol{int}}(\boldsymbol{u}_n)$$

Where the underscript denotes the incremental step and the superscript denotes the iteration.

The goal of the procedure is to find solution $\boldsymbol{u}^*$ such that the residual vector $\boldsymbol{r}$becomes zero (or gets close to zero).

After the expansion of the residual vector in Taylor series and ignoring the terms of 2nd and higher order

$$\boldsymbol{r}(\boldsymbol{u}^*) = \boldsymbol{r}\left(\boldsymbol{u}_{n+1}^{i-1}\right) + \left.\frac{\partial \boldsymbol{r}}{\partial \boldsymbol{u}}\right|_{\boldsymbol{u}_{n+1}^{i-1}} \left(\boldsymbol{u}^* - \boldsymbol{u}_{n+1}^{i-1}\right)$$

By demanding $\boldsymbol{r}(\boldsymbol{u}^*) = \boldsymbol{0}$ the above relation becomes

$$\boldsymbol{r}\left(\boldsymbol{u}_{n+1}^{i-1}\right) + \left.\frac{\partial \boldsymbol{r}}{\partial \boldsymbol{u}}\right|_{\boldsymbol{u}_{n+1}^{i-1}} \Delta \boldsymbol{u}_{n+1}^{i} = \boldsymbol{0}$$

Noting that external loading does not depend on nodal displacements

$$\left.\frac{\partial \boldsymbol{r}}{\partial \boldsymbol{u}}\right|_{\boldsymbol{u}_{n+1}^{i-1}} = \left.\frac{\partial \boldsymbol{f}^{\boldsymbol{int}}}{\partial \boldsymbol{u}}\right|_{\boldsymbol{u}_{n+1}^{i-1}} = \boldsymbol{K}_{n+1}^{i-1}$$

The equation of equilibrium takes the form

$$\boldsymbol{K}_{n+1}^{i-1} \Delta \boldsymbol{u}_{n+1}^{i} = \boldsymbol{f}_{n+1}^{\boldsymbol{ext}} - \boldsymbol{f}^{\boldsymbol{int}}\left(\boldsymbol{u}_{n+1}^{i-1}\right)$$

After the solution of the linear system of equation the next approximation of the nodal displacements

$$\boldsymbol{u}_{n+1}^{i} = \boldsymbol{u}_{n+1}^{i-1} + \Delta \boldsymbol{u}_{n+1}^{i}$$

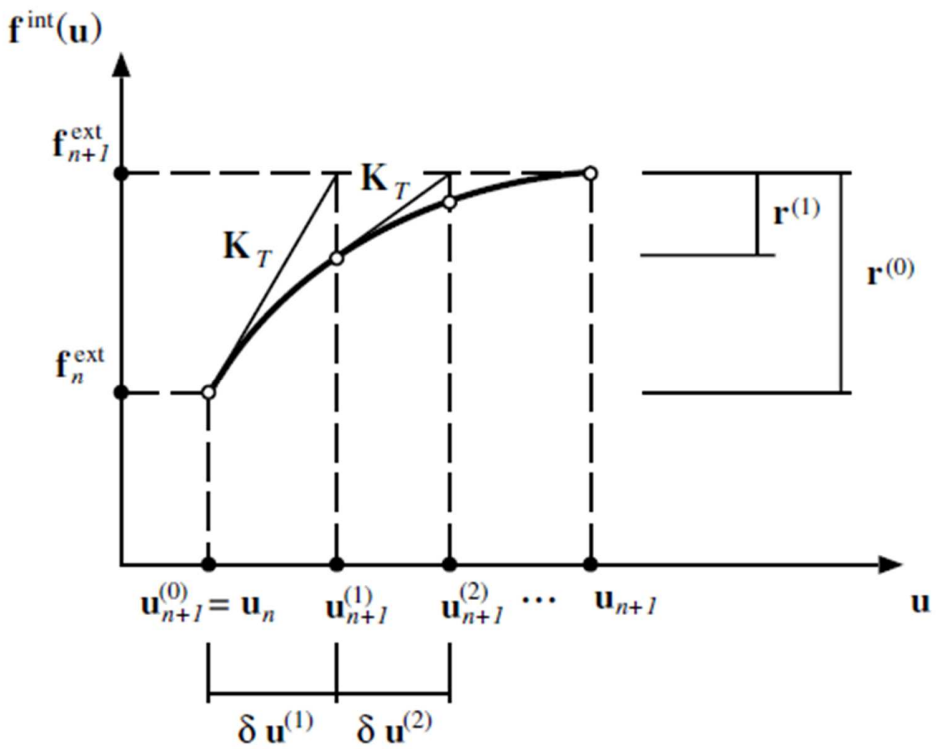

Figure 3.4: **The Newton–Raphson algorithm for the incremental finite element equilibrium equation**

The iterative procedure stops when the residual vector gets close to zero.

$$\|\boldsymbol{r}(\boldsymbol{u}_{n+1}^{i})\| < \varepsilon_{tol}\|\boldsymbol{f}_{n+1}^{\boldsymbol{ext}}\|$$

with ε_{tol} the desired tolerance.

The corresponding displacement vector $\boldsymbol{u}_{n+1}^{i}$ is then accepted as sufficiently close to the solution

Table 3.1 The Newton–Raphson algorithm for the incremental finite element equilibrium equation

1. Initialization of variables of load increment $n+1$

$$i = 0, \qquad \boldsymbol{u}_{n+1}^{0} = \boldsymbol{u}_n, \qquad \boldsymbol{f}^{\boldsymbol{int}}(\boldsymbol{u}_{n+1}^{0}) = \boldsymbol{f}^{\boldsymbol{int}}(\boldsymbol{u}_n), \qquad \boldsymbol{K}_{n+1}^{0} = \boldsymbol{K}_n$$

$$\boldsymbol{f}_{n+1}^{\boldsymbol{ext}} = \bigwedge_{e=1}^{N}\left(\int_{V_e} \boldsymbol{N_f}^T \boldsymbol{f}_{\boldsymbol{n+1}} dV_e + \int_{\partial V_\sigma} \boldsymbol{N_S}^T \boldsymbol{t}_{\boldsymbol{0_{n+1}}} dS\right)$$

2. Iteration i

$$i \leftarrow i+1, \qquad \Delta \boldsymbol{u}_{n+1}^{i} = \left(\boldsymbol{K}_{n+1}^{i-1}\right)^{-1}\left(\boldsymbol{f}_{n+1}^{ext} - \boldsymbol{f}^{int}\left(\boldsymbol{u}_{n+1}^{i-1}\right)\right)$$

$$\boldsymbol{u}_{n+1}^{i} = \boldsymbol{u}_{n+1}^{i-1} + \Delta \boldsymbol{u}_{n+1}^{i}$$

3. Calculation of element displacements & strains

$$\boldsymbol{u}_{n+1}^{i} \rightarrow \boldsymbol{u}^{(e)}{}_{\boldsymbol{n+1}}^{\boldsymbol{i}}, \qquad \boldsymbol{\varepsilon}_{n+1}^{i} = \boldsymbol{B}^{e}\boldsymbol{u}^{(e)}{}_{\boldsymbol{n+1}}^{\boldsymbol{i}}$$

4. Integration of elastoplastic relations for calculation of element stresses and elastoplastic material modulus at the integration points

$$\boldsymbol{\sigma}_{n+1}^{i} = \boldsymbol{\sigma}_{n+1}^{i}\left(\boldsymbol{\varepsilon}_{n+1}^{i}\right), \qquad \boldsymbol{C}^{ep}{}_{\boldsymbol{n+1}}^{\boldsymbol{i}} = \boldsymbol{C}^{ep}{}_{\boldsymbol{n+1}}^{\boldsymbol{i}}\left(\boldsymbol{\varepsilon}_{n+1}^{i}\right)$$

5. Calculation of equivalent nodal internal forces vector and tangent stiffness modulus of elements

$$\boldsymbol{f}_{\boldsymbol{e}}^{\boldsymbol{int}}\left(\boldsymbol{u}^{(e)}{}_{\boldsymbol{n+1}}^{\boldsymbol{i}}\right) = \sum_{j=1}^{NGP} w_j \boldsymbol{B}_{\boldsymbol{j}}^{T} \boldsymbol{\sigma}_{n+1_j}^{i}$$

$$\boldsymbol{k}^{(e)}{}_{\boldsymbol{n+1}}^{\boldsymbol{i}} = \sum_{j=1}^{NGP} w_j \boldsymbol{B}_{\boldsymbol{j}}^{T} \boldsymbol{C}^{ep}{}_{\boldsymbol{n+1}}^{\boldsymbol{i}} \boldsymbol{B}_j$$

6. Assemblage of global stiffness matrix and nodal internal forces vector

$$\boldsymbol{f}^{\boldsymbol{int}} = \bigwedge_{e=1}^{N} \boldsymbol{f}_{\boldsymbol{e}}^{\boldsymbol{int}}, \qquad \boldsymbol{K}_{n+1}^{i} = \bigwedge_{e=1}^{N} \boldsymbol{k}^{(e)}{}_{\boldsymbol{n+1}}^{\boldsymbol{i}}$$

7. Calculation of residual forces vector and check of convergence

$$\boldsymbol{r}\left(\boldsymbol{u}_{n+1}^{i}\right) = \boldsymbol{f}_{n+1}^{ext} - \boldsymbol{f}^{int}\left(\boldsymbol{u}_{n+1}^{i}\right)$$

$$\left\|\boldsymbol{r}\left(\boldsymbol{u}_{n+1}^{i}\right)\right\| < \varepsilon_{tol}\left\|\boldsymbol{f}_{n+1}^{ext}\right\| \rightarrow \begin{cases} true, & (*)_{n+1}^{i} = (*)_{n+1} \\ false, & then\ proceed\ to\ step\ 2 \end{cases}$$

3.3.7 Integration of Elastoplastic relations

In order to calculate the stresses at the integration points for the incremental step $n+1$, the elastoplastic stress-strain relations must be integrated.

Here, a material with von-Mieses yield condition and a general case of isotropic/ kinematic hardening is adopted for the representation of the numerical algorithm.

Table 3.2 Elastoplastic relations for Mieses hardening material

1. Linear elastic law $\boldsymbol{\sigma} = \boldsymbol{C}^e : \boldsymbol{\varepsilon}^e$
2. Yield function $f(\boldsymbol{\sigma}, \boldsymbol{\pi}, \sigma_y) = \sqrt{3J_2(\boldsymbol{s}(\boldsymbol{\sigma}) - \boldsymbol{\pi})} - \sigma_y = \sqrt{\frac{3}{2}}\|\boldsymbol{\eta}\| - \sigma_y$
3. Associative plastic flow rule $\dot{\boldsymbol{\varepsilon}}^p = \dot{\gamma}\frac{\partial f}{\partial \boldsymbol{\sigma}} = \dot{\gamma}\sqrt{\frac{3}{2}}\frac{\boldsymbol{\eta}}{\|\boldsymbol{\eta}\|}$

   where the normal to the yield function $\boldsymbol{N} = \frac{\partial f}{\partial \boldsymbol{\sigma}} = \sqrt{\frac{3}{2}}\frac{\boldsymbol{\eta}}{\|\boldsymbol{\eta}\|}$
4. Isotropic hardening curve $\sigma_y = \sigma_y(\bar{\varepsilon}^p)$
5. Kinematic hardening rule $\dot{\boldsymbol{\pi}} = \frac{2}{3}H^{\boldsymbol{k}}(\bar{\varepsilon}^p)\dot{\boldsymbol{\varepsilon}}^p = \dot{\gamma}\sqrt{\frac{2}{3}}H^{\boldsymbol{k}}(\bar{\varepsilon}^p)\frac{\boldsymbol{\eta}}{\|\boldsymbol{\eta}\|}$

The starting point here is the adoption of a backward Euler scheme for the time integration. An implicit integration method is preferred because it is unconditionally stable even for large time increments. Accordingly, for integration within a generic (pseudo-)time interval $[t_n, t_{n+1}]$, all rate quantities are replaced with corresponding incremental values within the considered interval and the rest with their values at the end of the interval t_{n+1}.

$$\boldsymbol{\varepsilon}^e_{n+1} = \boldsymbol{\varepsilon}^e_n + \Delta\boldsymbol{\varepsilon} - \Delta\boldsymbol{\varepsilon}^p$$

$$\boldsymbol{\varepsilon}^p_{n+1} = \boldsymbol{\varepsilon}^p_n + \Delta\gamma\boldsymbol{N}_{n+1}$$

$$\bar{\varepsilon}^p_{n+1} = \bar{\varepsilon}^p_n + \Delta\gamma$$

$$\boldsymbol{\pi}_{n+1} = \boldsymbol{\pi}_n + \Delta\gamma\sqrt{\frac{2}{3}}H^{\boldsymbol{k}}(\bar{\varepsilon}^p_{n+1})\frac{\boldsymbol{\eta}_{n+1}}{\|\boldsymbol{\eta}_{n+1}\|}$$

where the notation $\Delta(\cdot) = (\cdot)_{n+1} - (\cdot)_n$ was adopted.

The nature of the complementarity conditions

$$\dot{\lambda} \geq 0, \qquad f \leq 0, \qquad \dot{\lambda}f = 0$$

motivates the establishment of a (conceptually very simple) two-step algorithm in which the two possible sets of equations are employed sequentially and the final solution is selected as the only valid one.

(a) The Elastic Trial Step.

Firstly, the step $[t_n, t_{n+1}]$ is assumed to be elastic. The solution, which is not necessarily the actual one, will be called the elastic trial solution.

$$\Delta\gamma = 0$$

In this case there is no plastic flow or evolution of internal variables within the considered interval $[t_n, t_{n+1}]$.

$$\boldsymbol{\varepsilon}^e_{n+1} = \boldsymbol{\varepsilon}^e_n + \Delta\boldsymbol{\varepsilon}$$

$$\bar{\varepsilon}^p_{n+1} = \bar{\varepsilon}^p_n$$

$$\boldsymbol{\pi}_{n+1} = \boldsymbol{\pi}_n$$

The corresponding stress will be called the *elastic trial stress*, given by

$$\boldsymbol{\sigma}^{trial}_{n+1} = \boldsymbol{C}^e : \boldsymbol{\varepsilon}^e_{n+1}$$

Now note that, to be the actual solution, the elastic trial state has, in addition, to satisfy

$$f\left(\boldsymbol{\sigma}^{trial}_{n+1}\right) \leq 0$$

If the elastic trial state lies within the elastic domain or on the yield surface, it is accepted as a solution. In this case,

$$(\cdot)_{n+1} = (\cdot)^{trial}_{n+1}$$

and the algorithm is terminated. Otherwise, the elastic trial state is not plastically admissible and a solution must be obtained from the plastic corrector step described below.

(b) The Plastic Corrector Step (or Return-Mapping Algorithm).

The only option left now is to solve the problem with

$$f(\boldsymbol{\sigma}_{\boldsymbol{n+1}}) = 0$$

for some $\Delta\gamma > 0$

First, the deviatoric stress is calculated with the linear elastic law

$$\boldsymbol{s}_{\boldsymbol{n+1}} = \boldsymbol{s}^{trial}_{n+1} - 2G\Delta\gamma\sqrt{\frac{3}{2}}\frac{\boldsymbol{\eta}_{\boldsymbol{n+1}}}{\|\boldsymbol{\eta}_{\boldsymbol{n+1}}\|}$$

Subtracting the back-stress $\boldsymbol{\pi}_{n+1}$

$$\boldsymbol{\eta}_{\boldsymbol{n+1}} = \boldsymbol{\eta}^{trial}_{n+1} - \Delta\gamma\sqrt{\frac{3}{2}}\left[2G + \frac{2}{3}H^{\boldsymbol{k}}\left(\bar{\varepsilon}^p_{n+1}\right)\right]\frac{\boldsymbol{\eta}_{\boldsymbol{n+1}}}{\|\boldsymbol{\eta}_{\boldsymbol{n+1}}\|}$$

where $\boldsymbol{\eta}^{trial}_{n+1} = \boldsymbol{s}^{trial}_{n+1} - \boldsymbol{\pi}_n$

Note that the last expression implies that $\boldsymbol{\eta}_{\boldsymbol{n+1}}$ and $\boldsymbol{\eta}^{trial}_{n+1}$ are *collinear*, i.e. $\boldsymbol{\eta}_{\boldsymbol{n+1}}$ is a scalar multiple of $\boldsymbol{\eta}^{trial}_{n+1}$. This gives the identity

$$\frac{\boldsymbol{\eta}_{\boldsymbol{n+1}}}{\|\boldsymbol{\eta}_{\boldsymbol{n+1}}\|} = \frac{\boldsymbol{\eta}^{trial}_{n+1}}{\|\boldsymbol{\eta}^{trial}_{n+1}\|}$$

Substituting back to the expression of the reduced stress $\boldsymbol{\eta}_{\boldsymbol{n+1}}$

$$\boldsymbol{\eta}_{\boldsymbol{n+1}} = \left\{1 - \frac{\Delta\gamma}{\sigma_{e_{n+1}^{trial}}}\left[3G + H^{\boldsymbol{k}}\left(\bar{\varepsilon}_{n+1}^{p}\right)\right]\right\}\boldsymbol{\eta}_{n+1}^{trial}$$

where $\sigma_{e_{n+1}^{trial}}$ is the elastic trial relative effective stress, defined by $\sigma_{e_{n+1}^{trial}} = \sqrt{\frac{3}{2}}\left\|\boldsymbol{\eta}_{n+1}^{trial}\right\|$

Taking the norm and multiplying by $\sqrt{\frac{3}{2}}$, the expression for the effective stress at the end of the time increment is obtained

$$\sigma_{e_{\boldsymbol{n+1}}} = \sigma_{e_{n+1}^{trial}} - \Delta\gamma\left[3G + H^{\boldsymbol{k}}\left(\bar{\varepsilon}_{n+1}^{p}\right)\right]$$

Remembering that the yield condition must be satisfied at the end of the increment t_{n+1} and substituting the expressions of the equivalent plastic strain, a nonlinear scalar equation for $\Delta\gamma$ is obtained:

$$\tilde{f}(\Delta\gamma) = \sigma_{e_{n+1}^{trial}} - \Delta\gamma\left[3G + H^{\boldsymbol{k}}\left(\bar{\varepsilon}_{n}^{p} + \Delta\gamma\right)\right] - \sigma_{y}\left(\bar{\varepsilon}_{n}^{p} + \Delta\gamma\right) = 0$$

The solution of this nonlinear equation is obtained with the Newton- Raphson method, as before.

The derivative of $\tilde{f}(\Delta\gamma)$ with respect to $\Delta\gamma$ is calculated as

$$d = -3G - H^{\boldsymbol{k}}\left(\bar{\varepsilon}_{n}^{p} + \Delta\gamma\right) - H^{\boldsymbol{i}}\left(\bar{\varepsilon}_{n}^{p} + \Delta\gamma\right)$$

and $H^{\boldsymbol{i}} = \frac{\boldsymbol{d}\sigma_{y}}{\boldsymbol{d}\bar{\varepsilon}^{p}}$ is the slope of the isotropic hardening curve.

The solution is given by the iterative formula

$$\Delta\gamma^{(m)} = \Delta\gamma^{(m-1)} - \frac{\tilde{f}\left(\Delta\gamma^{(m-1)}\right)}{d}$$

with initial guess $\Delta\gamma^{(0)} = 0$.

The iterations stop when convergence is reached.

$$\left|\tilde{f}(\Delta\gamma)\right| < \varepsilon_{tol}$$

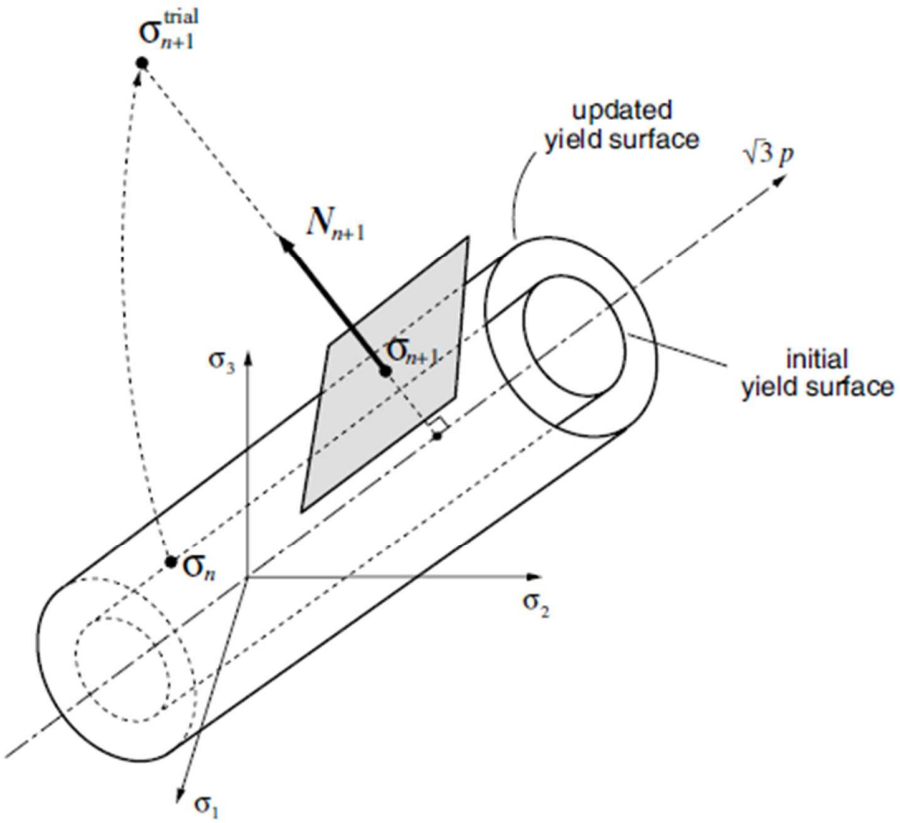

Figure 3.3: The implicit elastic predictor/return-mapping scheme for the von Mises model. Geometric interpretation in principal stress space.

The procedure of part (b) above possesses an appealing geometric interpretation as illustrated in Figure 3.3. Consider the yield surface at the elastic trial state. The elastic trial stress $\boldsymbol{\sigma}_{n+1}^{trial}$ in this case lies outside the plastically admissible domain (i.e. neither in the elastic domain nor on the yield surface). Upon solution of nonlinear equation $\tilde{f}(\Delta\gamma) = 0$, which is commonly referred to as the *plastic consistency equation*, ensures that the stress $\boldsymbol{\sigma}_{n+1}$ at the end of the interval $[t_n, t_{n+1}]$ lies on the updated yield surface; that is, the elastic trial stress *returns* to the yield surface so that plastic consistency is re-established in the updated state. In the case of perfect plasticity, $\boldsymbol{\sigma}_{n+1}^{trial}$ returns to a *fixed* surface. Due to this interpretation the procedure of part (b) is referred to as the *return mapping algorithm*

Table 3.3 Implicit elastic predictor/return-mapping algorithm for the von Mises model with mixed nonlinear hardening.

1. Elastic predictor

$$\boldsymbol{\varepsilon}^{e}_{n+1}{}^{trial} = \boldsymbol{\varepsilon}^{e}_{n} + \Delta\boldsymbol{\varepsilon}$$

$$\bar{\varepsilon}^{p}_{n+1}{}^{trial} = \bar{\varepsilon}^{p}_{n}, \qquad \boldsymbol{\pi}^{trial}_{n+1} = \boldsymbol{\pi}_{n}$$

$$p^{trial}_{n+1} = K\varepsilon_{v}{}^{e\,trial}_{n+1}, \qquad \boldsymbol{s}^{trial}_{n+1} = 2G\varepsilon_{d}{}^{e\,trial}_{n+1}$$

$$\boldsymbol{\eta}^{trial}_{n+1} = \boldsymbol{s}^{trial}_{n+1} - \boldsymbol{\pi}_{n}, \qquad \sigma_{e}{}^{trial}_{n+1} = \sqrt{\frac{3}{2}}\left\|\boldsymbol{\eta}^{trial}_{n+1}\right\|$$

2. Check plastic admissibility
   IF $\sigma_{e}{}^{trial}_{n+1} - \sigma_{y}\left(\bar{\varepsilon}^{p}_{n+1}{}^{trial}\right) \leq 0$
   THEN set $(\cdot)_{n+1} = (\cdot)^{trial}_{n+1}$ and EXIT
3. Return mapping
   Solve equation for $\Delta\gamma$

$$\tilde{f}(\Delta\gamma) = \sigma_{e}{}^{trial}_{n+1} - \Delta\gamma\left[3G + H^{k}\left(\bar{\varepsilon}^{p}_{n} + \Delta\gamma\right)\right] - \sigma_{y}\left(\bar{\varepsilon}^{p}_{n} + \Delta\gamma\right) = 0$$

   and update

$$\bar{\varepsilon}^{p}_{n+1} = \bar{\varepsilon}^{p}_{n} + \Delta\gamma$$

$$\boldsymbol{\pi}_{n+1} = \boldsymbol{\pi}_{n} + \Delta\gamma\sqrt{\frac{2}{3}}H^{k}\left(\bar{\varepsilon}^{p}_{n+1}\right)\frac{\boldsymbol{\eta}_{n+1}}{\|\boldsymbol{\eta}_{n+1}\|}$$

$$p_{n+1} = p^{trial}_{n+1}, \qquad \boldsymbol{s}_{n+1} = \boldsymbol{s}^{trial}_{n+1} - 2G\Delta\gamma\sqrt{\frac{3}{2}}\frac{\boldsymbol{\eta}_{n+1}}{\|\boldsymbol{\eta}_{n+1}\|}$$

$$\boldsymbol{\sigma}_{n+1} = \boldsymbol{s}_{n+1} + p_{n+1}\boldsymbol{I}, \qquad \boldsymbol{\varepsilon}^{e}_{n+1} = \frac{1}{2G}\boldsymbol{s}_{n+1} + \frac{1}{3}\varepsilon_{v}{}^{e\,trial}_{n+1}\boldsymbol{I}$$

4. EXIT

3.3.8 Consistent Tangent Modulus

The incremental constitutive equation for the determination of stress has the form

$$\boldsymbol{\sigma}_{n+1} = \bar{\boldsymbol{\sigma}}_{n+1}\left(\bar{\varepsilon}^{p}_{n}, \boldsymbol{\pi}_{n}, \boldsymbol{\varepsilon}^{e\,trial}_{n}\right)$$

The elastoplastic tangent stiffness matrix is defined as

$$\boldsymbol{C}^{ep}_{n+1} = \frac{\partial\bar{\boldsymbol{\sigma}}_{n+1}}{\partial\boldsymbol{\varepsilon}_{n+1}}$$

The crucial point that it must be emphasized is that the tangent moduli that appear in the linearized problem must be obtained by consistent linearization of the response function resulting from the integration algorithm, in order to preserve the quadratic rate of asymptotic convergence of the Newton-Raphson scheme.

Under plastic flow, the algorithmic incremental constitutive function gives

$$\boldsymbol{\sigma}_{\boldsymbol{n+1}} = \left[\boldsymbol{C}^e - \frac{\Delta\gamma 6G^2}{\sigma_{e_{n+1}}^{trial}}\boldsymbol{I}_d\right] : \boldsymbol{\varepsilon}_{n+1}^{e\ trial} + \frac{\Delta\gamma 3G}{\sigma_{e_{n+1}}^{trial}}\boldsymbol{\pi}_n$$

The elastoplastic consistent tangent operator for the present case is obtained by differentiating the above relation.

$$\boldsymbol{C}_{n+1}^{ep} = K\mathbf{1}x\mathbf{1} + 2G\left(1 - \frac{\Delta\gamma 3G}{\sigma_{e_{n+1}}^{trial}}\right)\boldsymbol{I}_d + 6G^2\left(\frac{\Delta\gamma}{\sigma_{e_{n+1}}^{trial}} - \frac{1}{3G + H^k + H^i}\right)\overline{\boldsymbol{N}}_{n+1}x\overline{\boldsymbol{N}}_{n+1}$$

where $\mathbf{1}$ is the 2nd order unit tensor, $\boldsymbol{I}_d$ is the deviator of the 4th order unit tensor, x is the dyadic product notation between two tensors and $\overline{\boldsymbol{N}}_{n+1} = \frac{\boldsymbol{\eta}_{\boldsymbol{n+1}}}{\|\boldsymbol{\eta}_{\boldsymbol{n+1}}\|}$ the unit flow vector.

Notice that the consistent elastoplastic modulus is slightly different from the elastoplastic modulus, which would result from the differentiation of the continuous equations and not the discrete ones. However, for small plastic increments $\Delta\gamma \to 0$, the consistent modulus tends to coincide with the continuous one.

Chapter 4: **Numerical Examples**

In this chapter, a few simple examples, which are available in literature and have been investigated by many authors, are analysed.

The FEM software for the step-by-step elastoplastic analysis is ABAQUS

4.1 Structure 1: Square plate with a central circular hole

Problem definitions

This problem has been addressed frequently in the literature. The various loading cases, used, were taken so as to belong to different regions below and above shakedown and ratcheting boundaries, as these have been estimated in Chen & Ponter (2001). The prescribed time histories of the loads are taken from Spiliopoulos & Panagiotou (2012). Results are plotted for the most highly stressed points, which are the Gauss points closest to the cusps of the hole.

Geometry: The plate geometry is described in Fig. 4.1. The square plate has dimensions $L \times L = 100 \times 100\ mm^2$ and thickness $d = 2\ mm$, where the dimension of the central circular hole is $D = 20\ mm$. By the symmetry of both geometry and applied loads, a quarter of the structure is modelled.

Material: Young's modulus: $E = 210\ GPa$, yield stress: $\sigma_y = 360\ MPa$, Poisson's ratio: $\nu = 0.3$.

Loads: Uniformly distributed loads: vertical tension load P_y and lateral tension load P_x. These loads have prescribed time histories for each case.

FEM model: The model consists of 308 quadratic 20-node-3D elements (C3D20 elements), with 3x3 Gaussian points for numerical integration to model a quarter of the structure (Fig. 4.1.1).

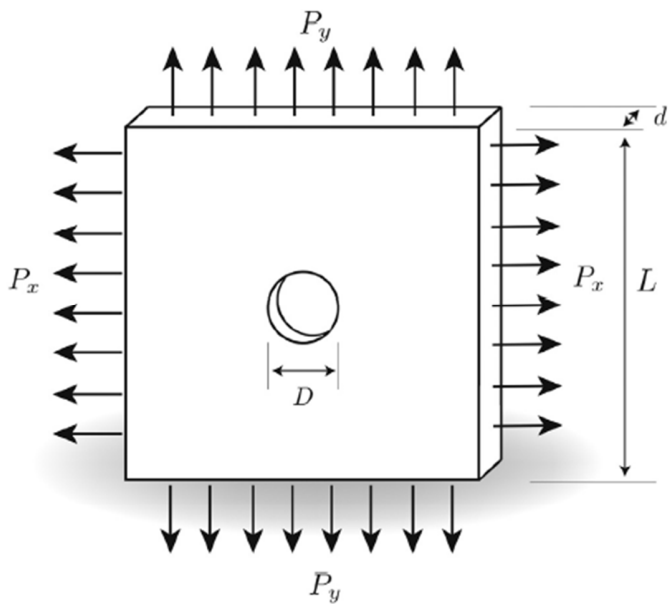

Figure 4.1.1: Square plate with central circular hole.

Loading case (a): The first cyclic loading case has the following variation with time (Fig 4.1.2):

$$P_y(t) = 0.65\sigma_y \sin^2(\pi t/T)\,, \qquad P_x(t) = 0$$

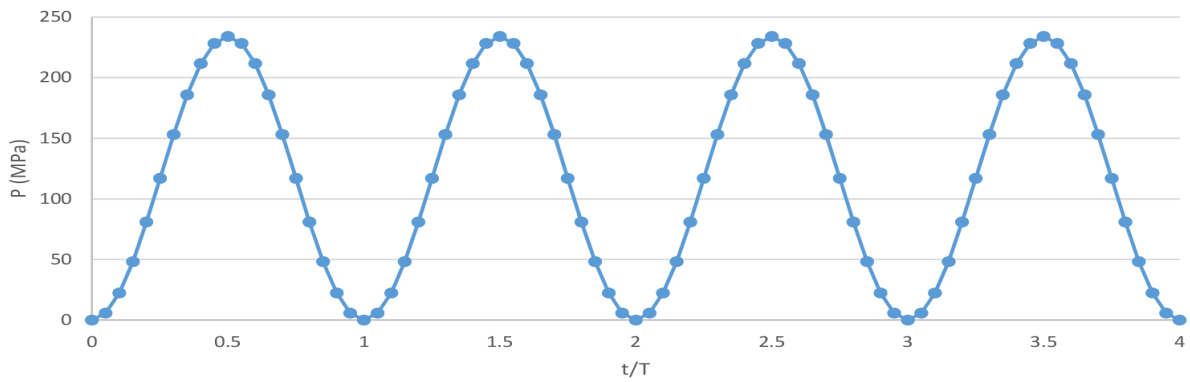

Figure 4.1.2: Load variation with time over four periods (loading case a).

The steady state predicted for the structure, is a shakedown state and this complies with the fact that this loading is below the shakedown boundary calculated in Chen & Ponter (2001).

In Fig.4.1.3, it is shown the total Mieses stress inside the steady cycle nowhere exceeds the yield stress and attains its maximum value, which is equal with the yield stress, when the external load takes its maximum value.

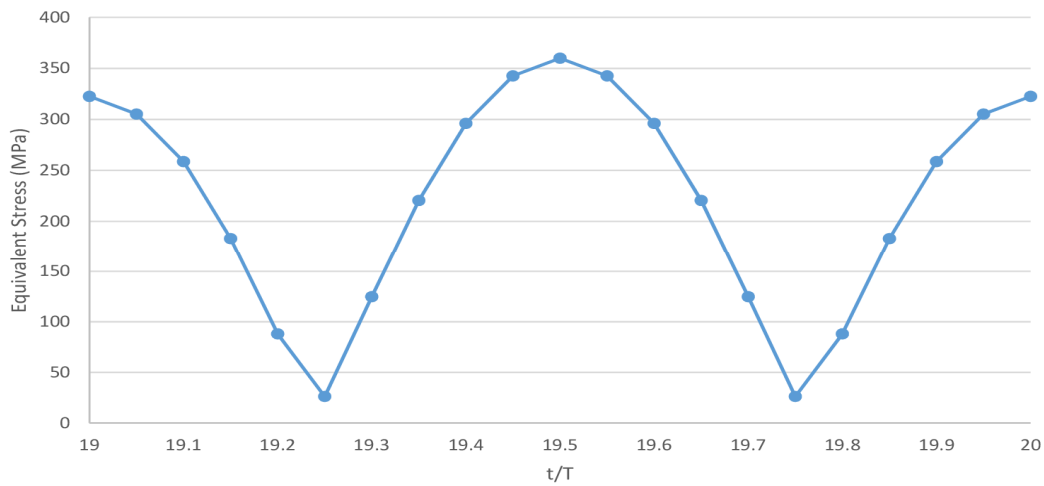

Figure 4.1.3: Equivalent Mieses stress distribution inside a cycle at steady-state (load case a – shakedown).

The plastic strains cease to grow after the first cycle of loading, which was expected for a perfectly plastic material. The plastic strain component along the direction yy is given in Fig. 4.1.4, where it is clear that shakedown occurs after the first cycle.

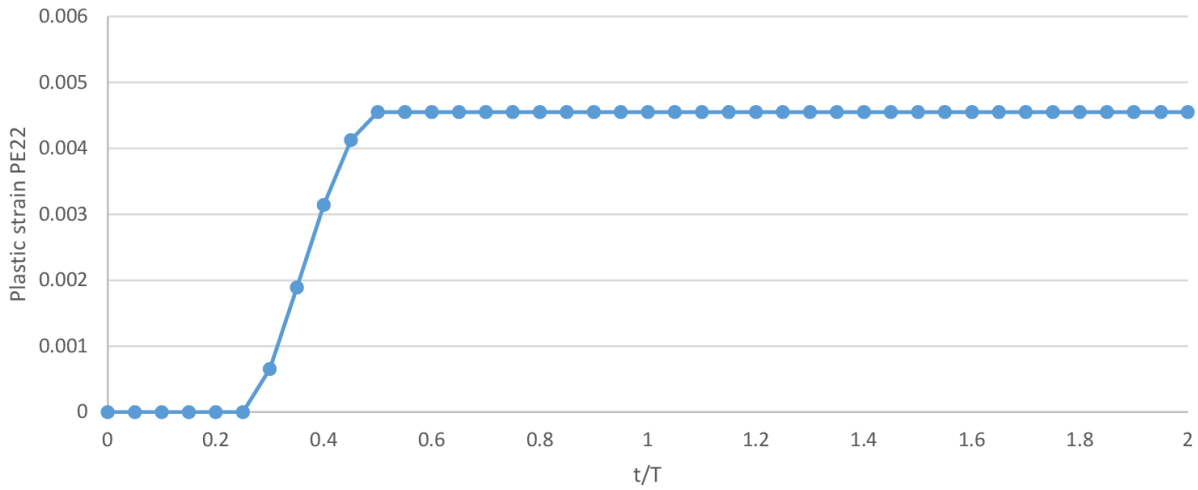

Figure 4.1.4: Plastic strain y-y component (load case a – shakedown).

<u>Loading case (b)</u>: The second cyclic loading case has the following variation with time (Fig. 4.1.5):

$$P_y(t) = 0.65\sigma_y \sin(2\pi t/T), \qquad P_x(t) = 0$$

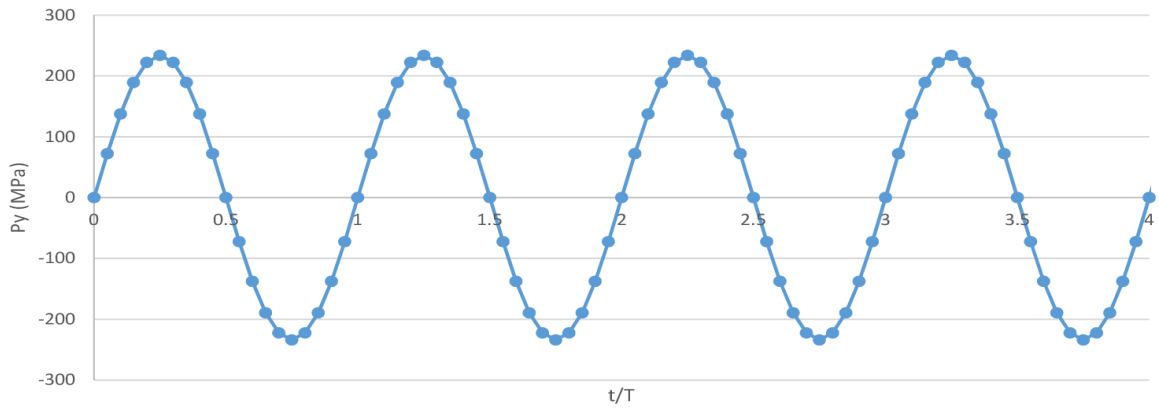

Figure 4.1.5: Load variation with time over four periods (loading case b).

The value of this load, at many cycle points, proves to be well in excess of the shakedown-reverse plasticity boundary. The present numerical procedure shows that this loading will lead some GPs to local reverse plasticity. The Fig. 4.1.6 shows the local reverse plasticity mechanism predicted by the time-stepping program.

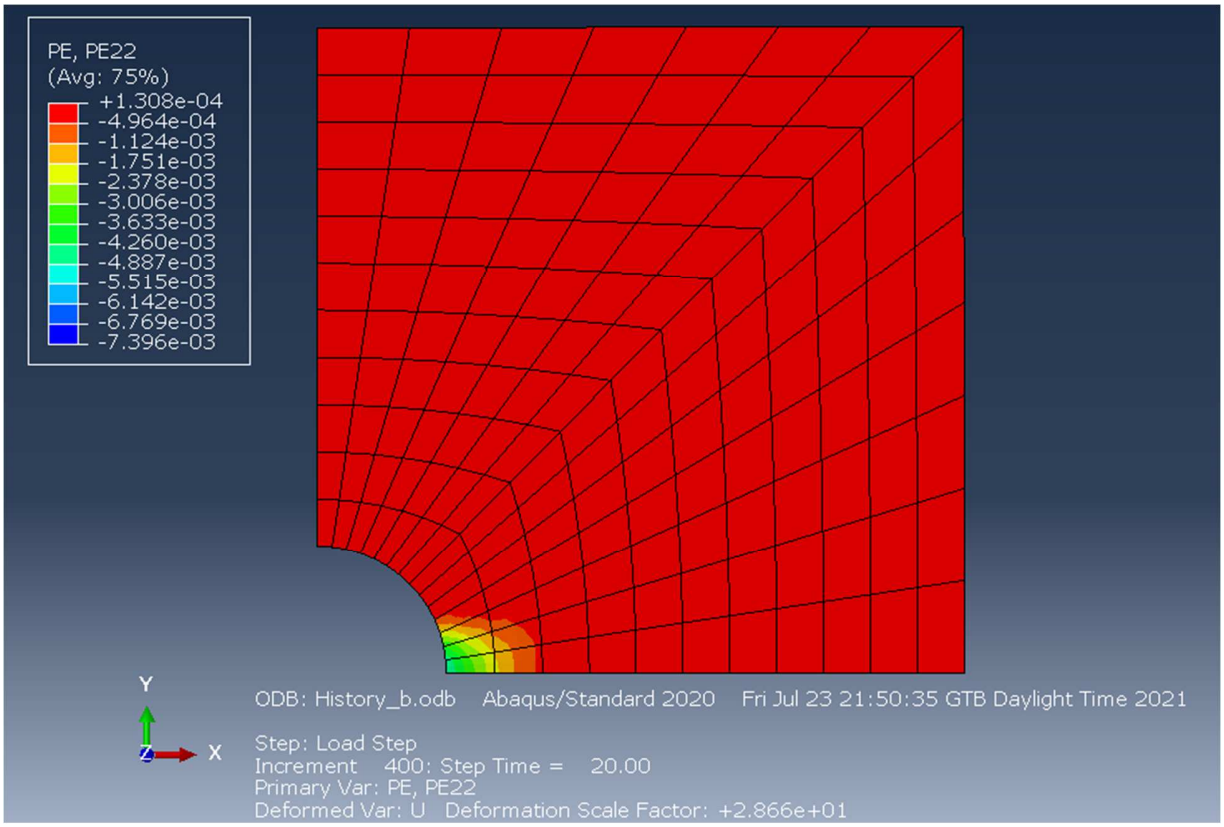

Figure 4.1.6: Local alternating plasticity mechanism for load case b.

The variation of the plastic strain of the most highly strained Gauss point of the structure inside the steady cycle is plotted in Fig. 4.1.7. Plastic straining occurs, alternately, inside the time intervals [0,0.25] and [0.5,0.75] at the steady cycle. The plastic strain along the yy at this GP of the time stepping program fluctuates around zero.

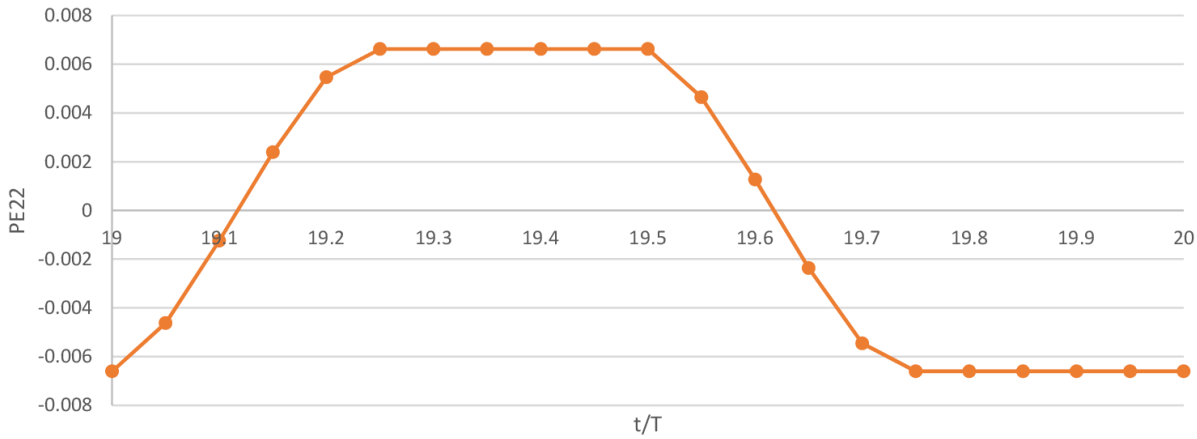

Figure 4.1.7: Plastic strain y-y component (load case b – alternating plasticity).

The stress- plastic strain diagram (direction yy) shows that loading b leads to a steady state where the magnitude of plastic strains cease growing which means that the total displacements remain bounded. However, this state is not safe, because the material breaks down after a small number of cycles due to Low Cycle Fatigue.

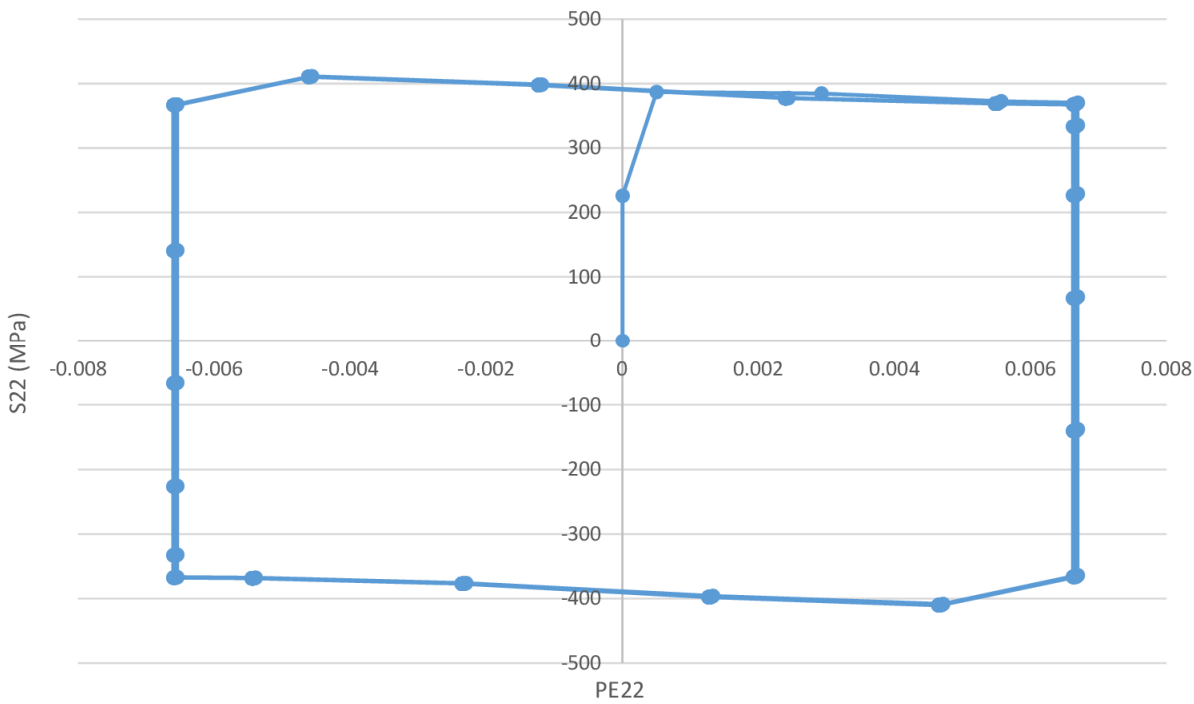

Figure 4.1.8: Stress- plastic strain diagram (load case b – alternating plasticity).

<u>Loading case (c)</u>: The third cyclic loading case involves two loads, one constant in time and one varying with time (Fig. 4.1.9):

$$P_x(t) = 0.6\sigma_y = constant, \qquad P_y(t) = 0.8\sigma_y \sin^2(\pi t/T)$$

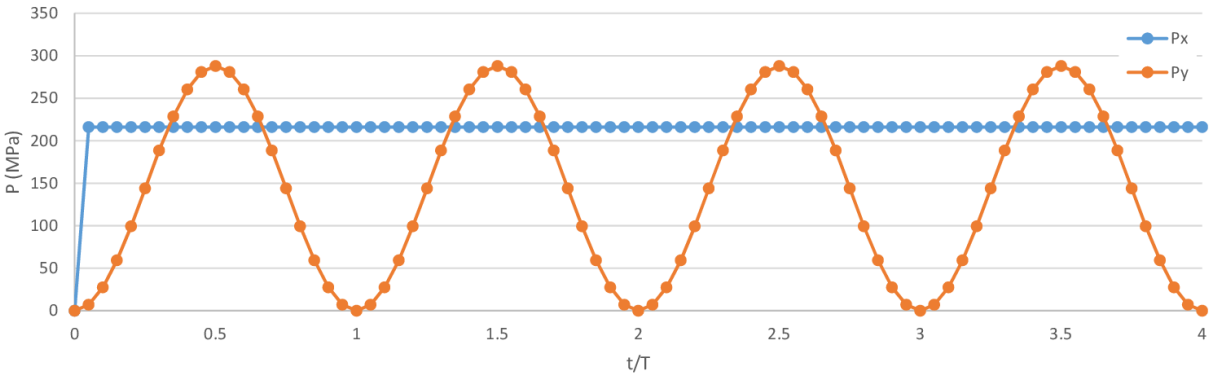

Figure 4.1.9: Load variation with time over four periods (loading case c).

The combination of the two loads leads to an excursion well above the shakedown-reverse plasticity boundary. An alternating plasticity mechanism is predicted by the present numerical procedure for some GPs near the edge of the hole (Fig. 4.1.10).

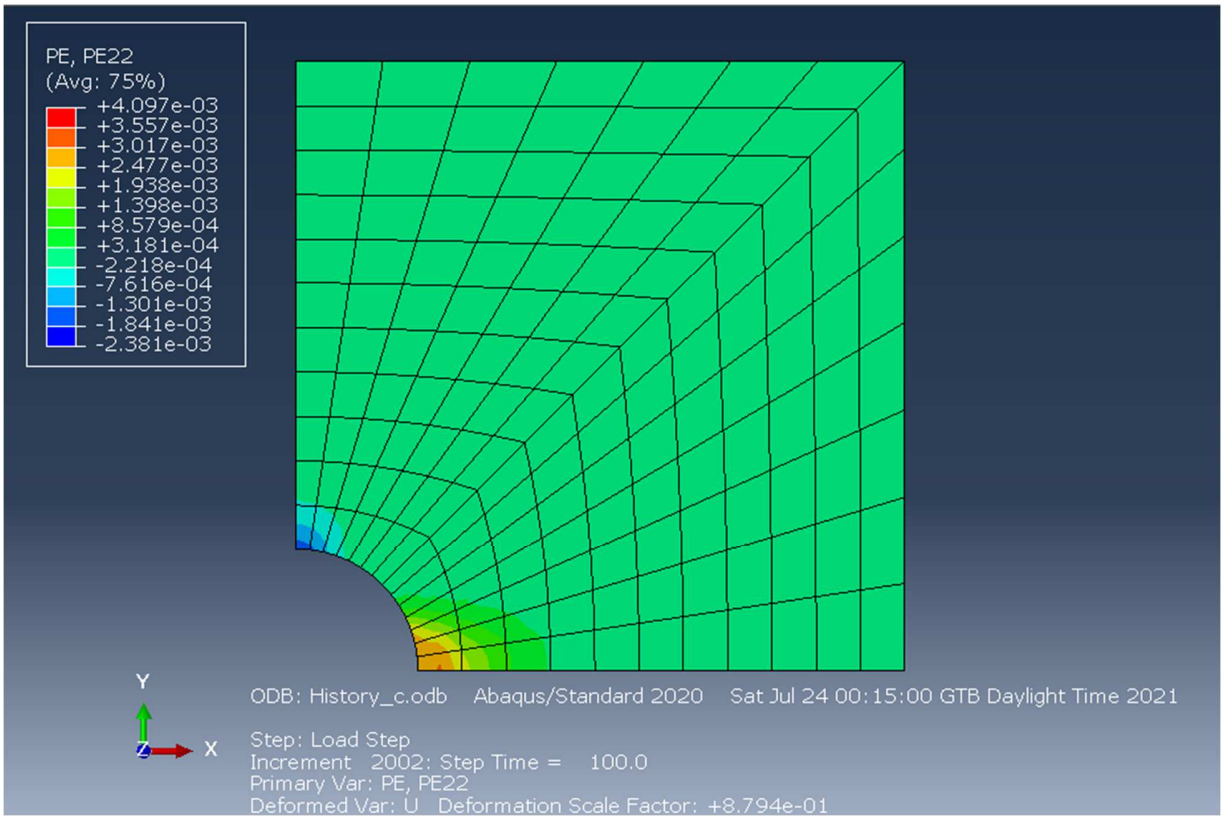

Figure 4.1.10: Local alternating plasticity mechanism for load case c.

Once again the variation of the plastic strain of the most strained GP is plotted for the steady state (Fig. 4.1.11). It is evident that plastic straining of alternating nature occurs inside the time intervals [0.35,0.50] and [0.85,1.00] at the steady cycle. The structure has adopted to the external loading and responds with closed stress-strain cycles after the first period. However, this is not a safe state due to material failure from LCF after a few cycles.

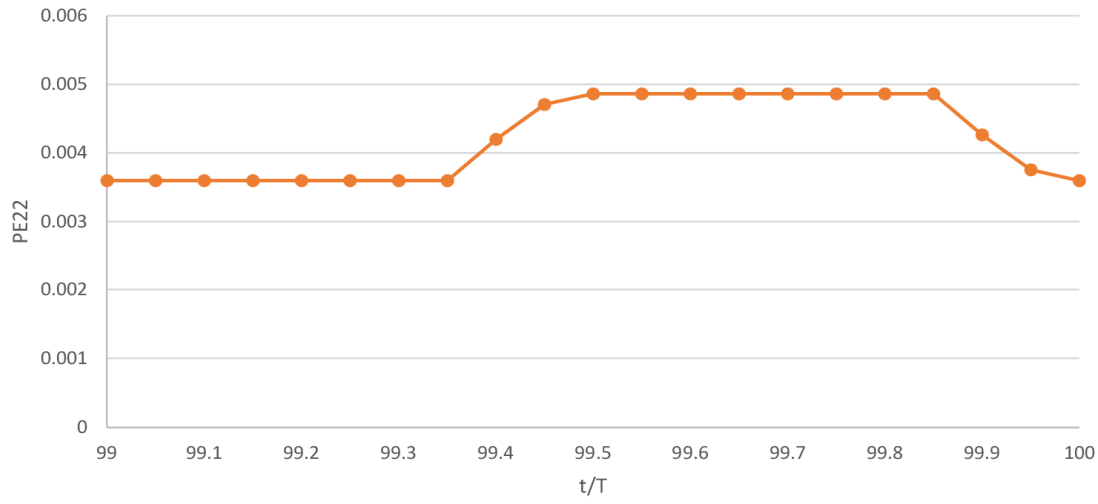

Figure 4.1.11: Plastic strain y-y component (load case c – alternating plasticity).

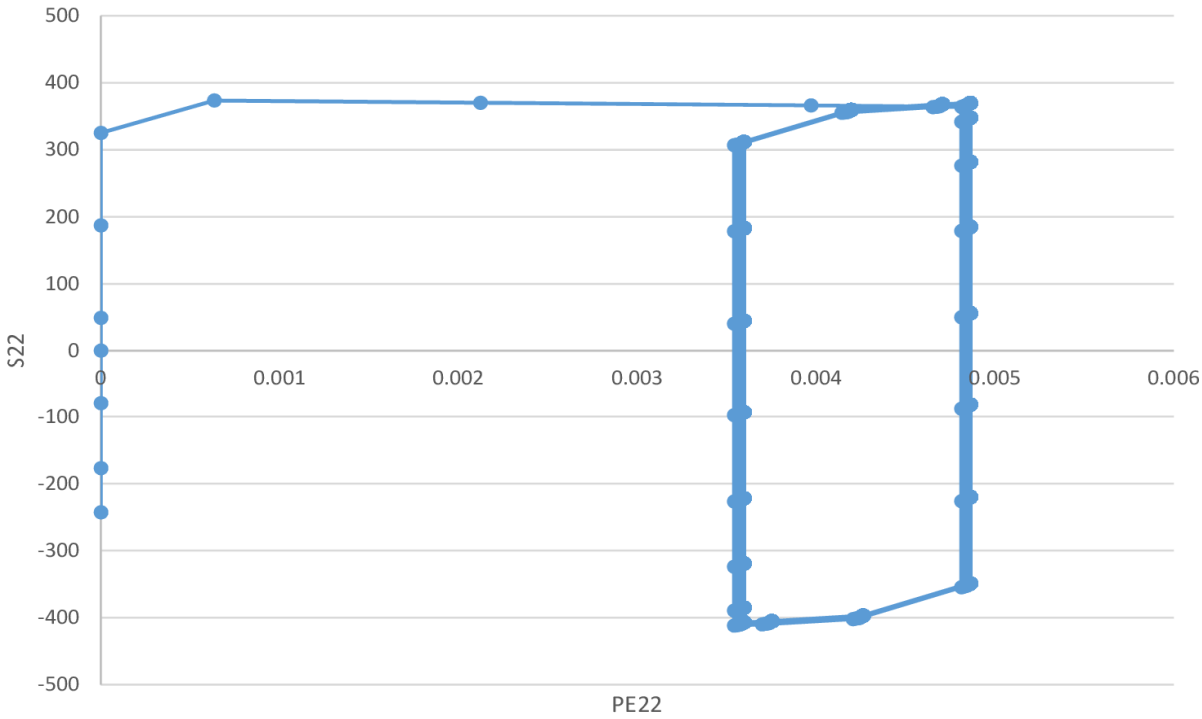

Figure 4.1.12: Stress- plastic strain diagram (load case c – alternating plasticity).

Due to this alternating plasticity mechanism, the plastic dissipation of the structure grows steadily without bound (Fig 4.1.13), which is a clear indicator of inadaptation.

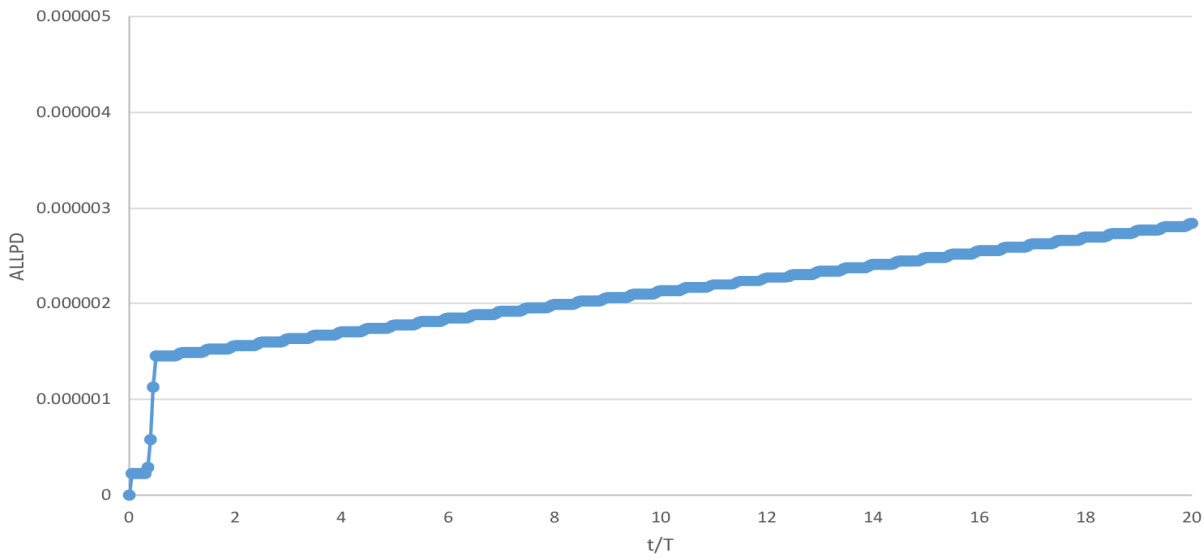

Figure 4.1.13: Plastic dissipation of the whole model (load case c – alternating plasticity).

Loading case (d): The fourth cyclic loading case also involves two loads, one with ramp amplitude for the first cycle and constant after the first cycle and one varying with time (Fig. 4.1.14).

$$P_x(t) = 0.85\sigma_y = constant, \qquad P_y(t) = 0.5\sigma_y \sin^2(\pi t/T)$$

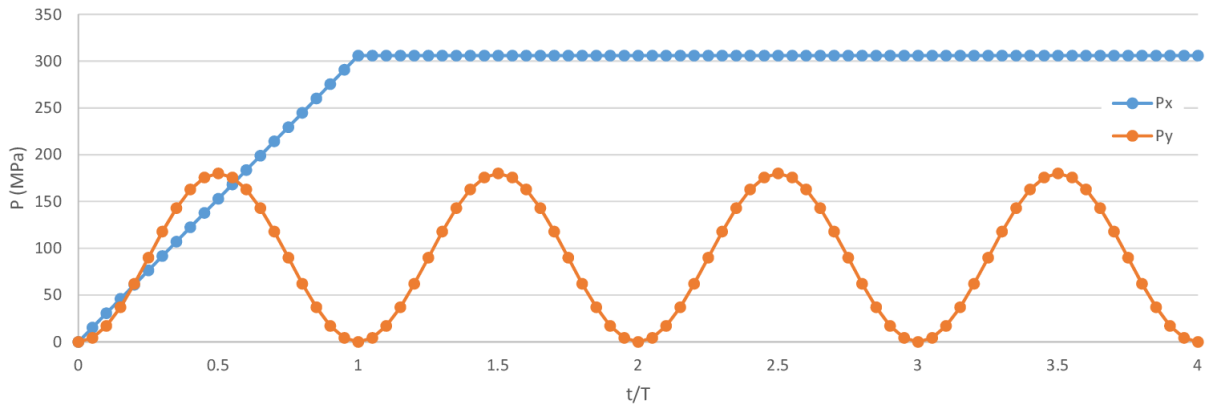

Figure 4.1.14: Load variation with time over four periods (loading case d).

The numerical model predicts instantaneous collapse at $t = 0.9572$. The collapse mechanism is illustrated in Fig. 4.1.15. The mechanism is created by the excessive plastic straining in a large portion of the plate. Plasticity starts from the edge of the whole and spreads diagonally, causing yielding of the material along that diagonal strip. The yielding along this strip forms the collapse mechanism and the right part of the plate slides horizontally. This slide leads to excessive deformations without increasing external loading.

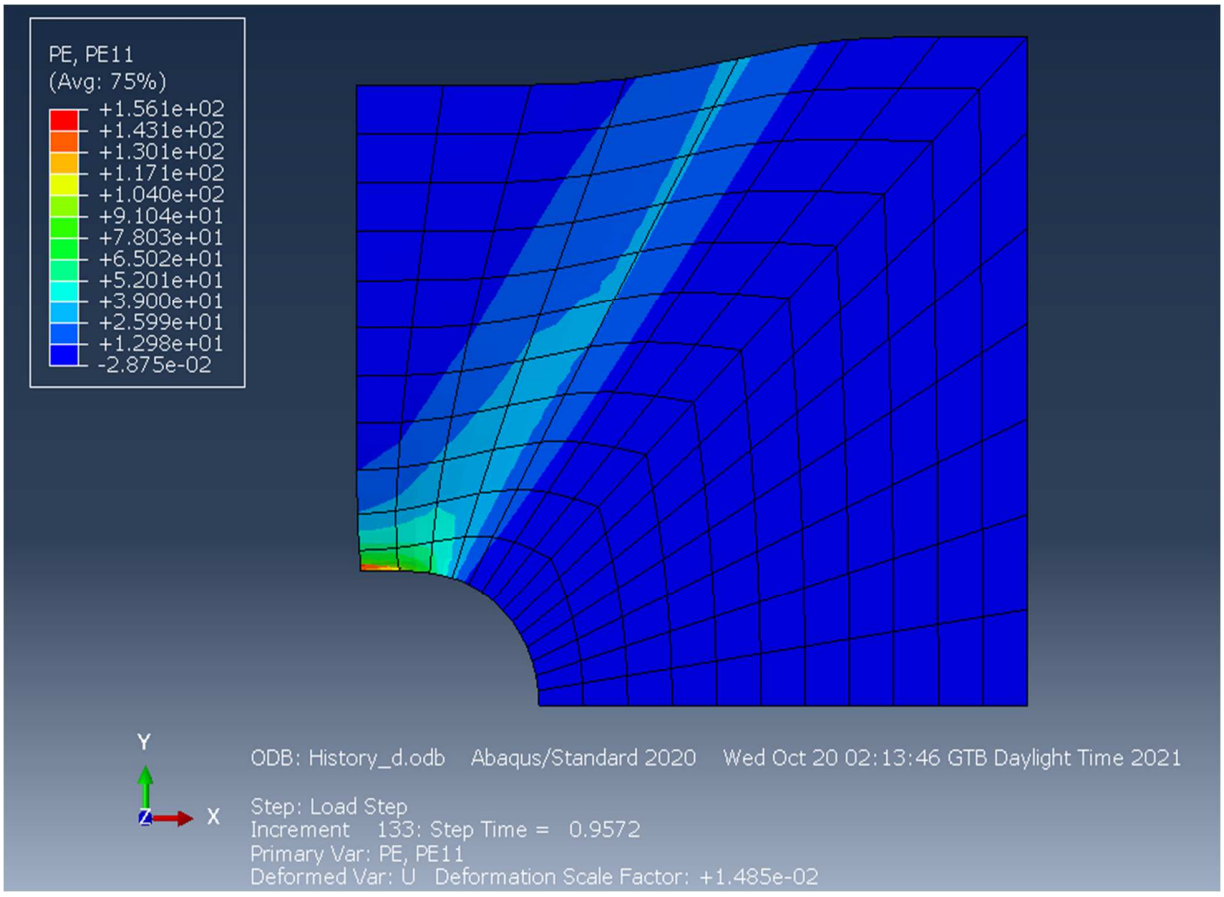

Figure 4.1.15: Collapse mechanism for load case d.

The plastic dissipation, which is presented in Fig 4.1.16, confirms that the loading leads to collapse of the structure, as it tends to infinity near the collapse load.

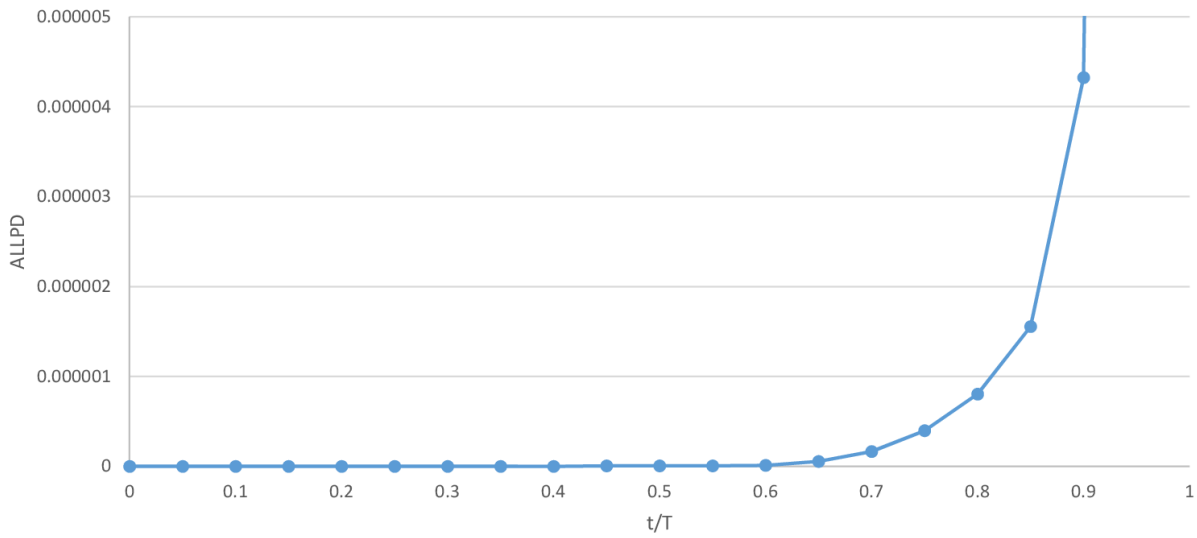

Figure 4.1.16: Plastic dissipation of the whole model (load case d – plastic collapse).

4.2 Structure 1: Square plate with a central circular hole- Shakedown Domain

Problem definitions

This problem has been treated very frequently in literature. For limit and shakedown analysis using the von Mises yield criterion, Staat, Heitzer (2003) presented the FEM based lower bound solutions. Tran T.N. (2008) presented the FEM based upper bound solutions using the exact Ilyushin yield surface and shell elements. Vu D.K. (2001) presented the FEM based primal-dual solutions. etc. Further perfectly plastic analyses of the problem have been compared in Schwabe (2000). As stated in Tran T.N. (2008), Vu D.K. (2001) this structure fails with alternating plasticity. Therefore, there is no benefit of hardening. The shakedown analysis for this structure has two aims: one is the validation for ${\sigma_u}/{\sigma_y} = 1$, and the other one is to confirm the benefit of the hardening effect. The results obtained here will be compared to the ones from the work of Huang, Xu, Chen, Zhang, Bezold, Qin (2019).

Geometry: The model geometry has been described in section 4.1

Material: Young's modulus: $E = 210\ GPa$, yield stress: $\sigma_y = 280\ MPa$, hardening effect (ultimate strength): $\sigma_u = 450\ MPa$ for bounded hardening, Poisson's ratio: $\nu = 0.3$.

Loads: Uniformly distributed loads: vertical tension load P_y and lateral tension load P_x. These loads vary independently in the domains: $P_x \in [0, P_x^{max}]$, $P_y \in [0, P_y^{max}]$

FEM model: The model consists of 1200 8-node-3D elements (C3D8 elements), with 2x2 Gaussian points for numerical integration to model a quarter of the structure.

Elastic Analysis

Before the modelling of the nonlinear material, a purely elastic solution is obtained for a horizontal load $P_x = 100\ MPa$, in order to identify the stress concentration zones of the plate and get an idea of the deformation of the structure.

In Fig 4.2.1.the purely elastic stress field for $P_x = 100\ MPa$ compares well with the one obtained in Huang et al. (2019). It is clear that the stress concentrates near the edge of the hole with a maximum value of Mieses stress around 3.2 times higher than the applied load.

Fig. 4.2.2 shows the purely elastic horizontal displacement field with its maximum value obtained at the lower right corner as expected.

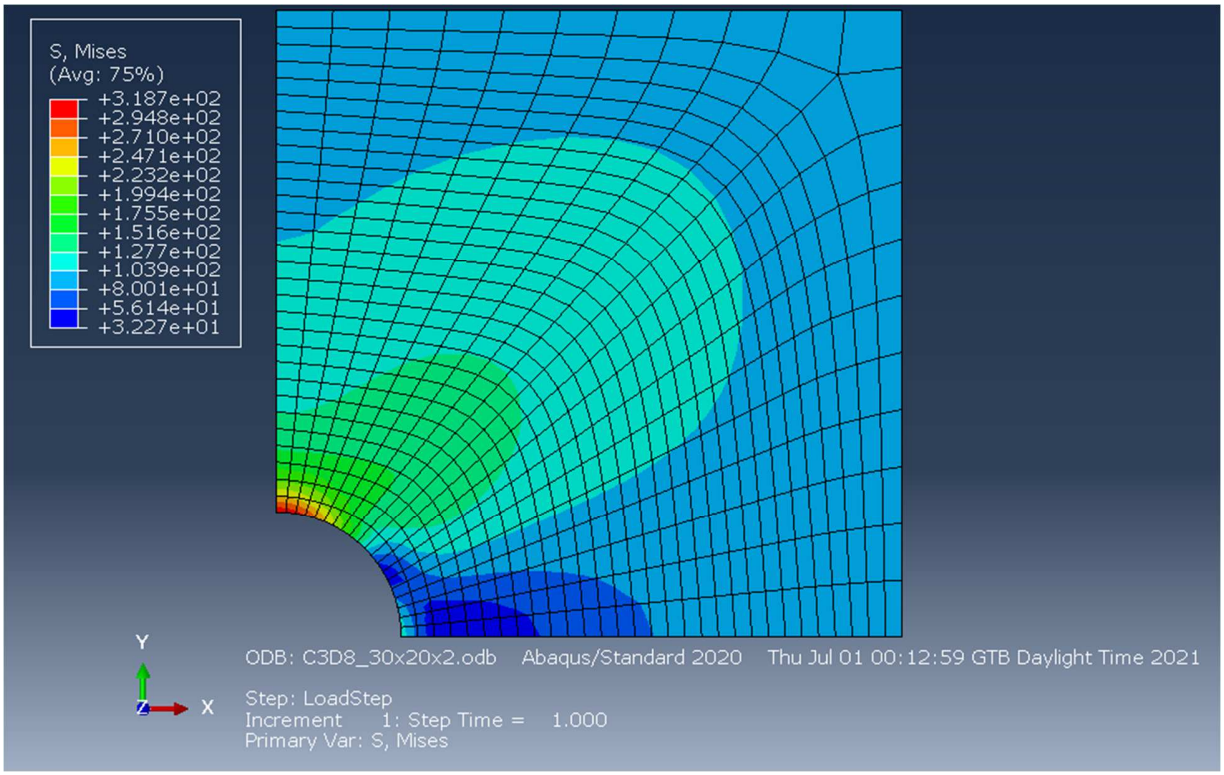

Figure 4.2.1: Purely Elastic Stress Field

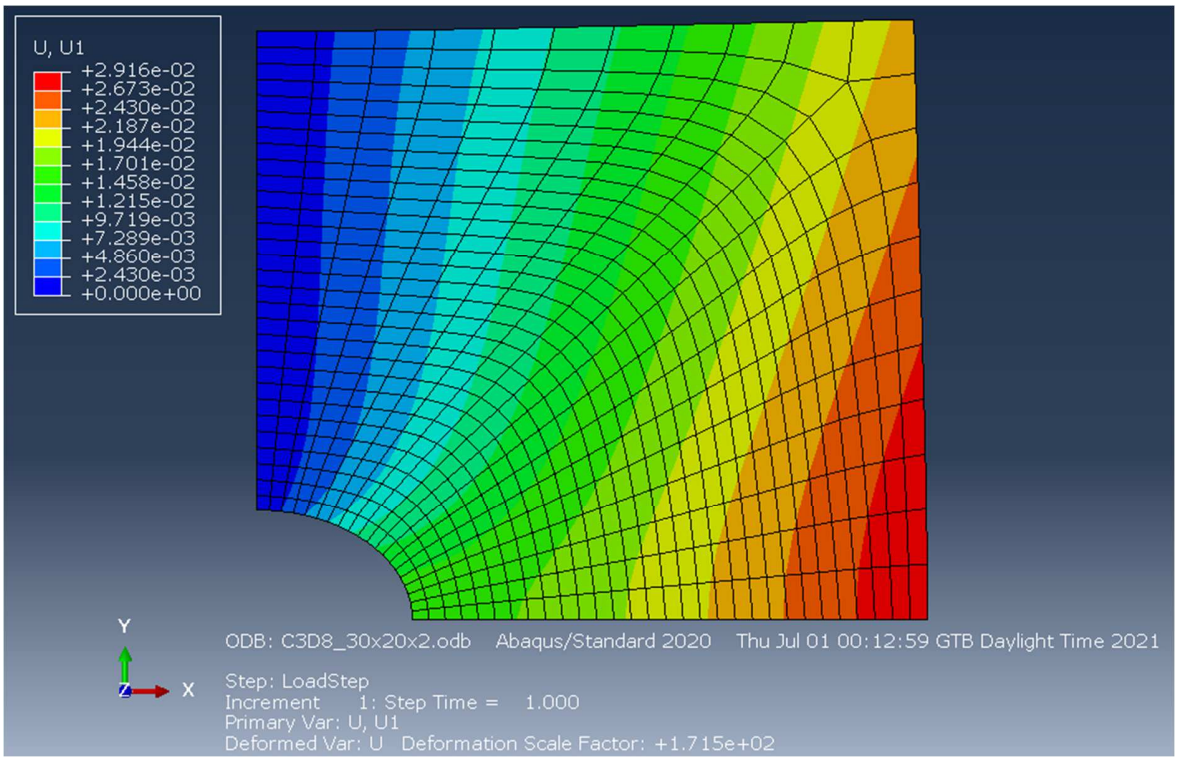

Figure 4.2.1: Purely Elastic Displacement Field U1

Shakedown bounds

Firstly, to validate the numerical procedure for the determination of shakedown bounds, perfectly plastic material ${\sigma_u}/{\sigma_y} = 1$ is chosen.

Case ${P_y^{max}}/{P_x^{max}} = 1$

This is the case, where the maximum values of the horizontal and vertical loads are equal. In order to calculate the maximum value of the two loads before inadaptation sets in, the structure is subjected to elastoplastic step-by-step analysis with a cyclic loading which contains the four vertices of the loading domain (Fig. 4.2.3).

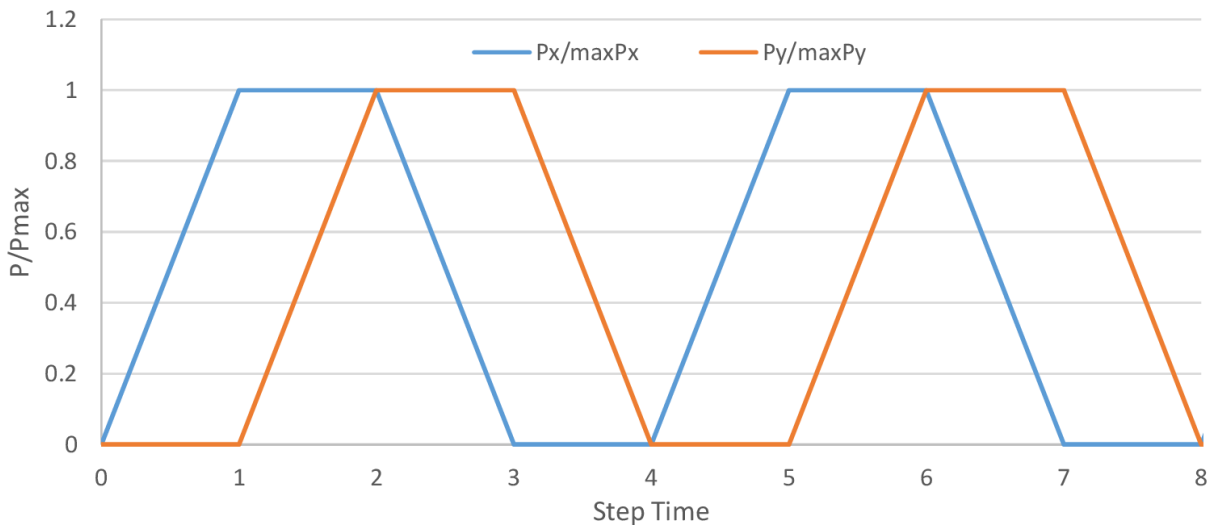

Figure 4.2.3: Load variation with time over two periods.

The structure was analyzed for increasing values for external load with the loading history described above. The plastic dissipation, the plastic strains and the total displacements were monitored in every analysis. If the values of these quantities were stabilized, then the structure had shaken down.

After several analyses, the shakedown boundary, i.e. the maximum value for which the structure shakes down, was calculated.

$$P^{max} = 135\ MPa\ \ or\ \ {P^{max}}/{\sigma_y} = 0.48$$

Note that the stabilization occurred after the first cycle of loading with the above maximum value.

It is obvious that for a maximum value less than the shakedown boundary, the structure also shakes down, but a bigger value would lead to inadaptation. The behaviour of the structure for loads higher than the shakedown limit is investigated in the following figures. Fig. 4.2.4 shows the plastic dissipation of the structure, where it can be observed that it tends to a finite bound as the load approaches the shakedown limit. Fig. 4.2.5 shows the maximum displacement of the

plate for the same applied load histories. Since the maximum displacement is bounded, the incremental collapse mode is excluded. This means that the inadaptation mode is alternating plasticity. The stress- strain diagram of the most strained GP (Fig 4.2.6) confirms the alternating plasticity mode.

In the same way the shakedown bound is calculated for any ratio of maximum loads.

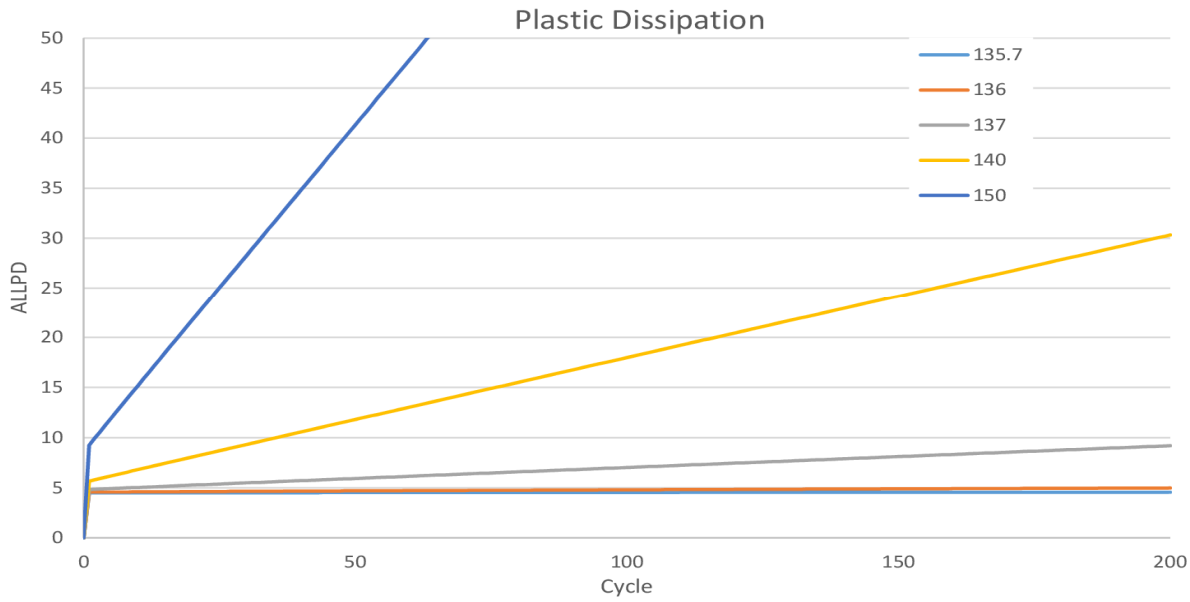

Figure 4.2.4: Plastic dissipation for loads exceeding the shakedown limit.

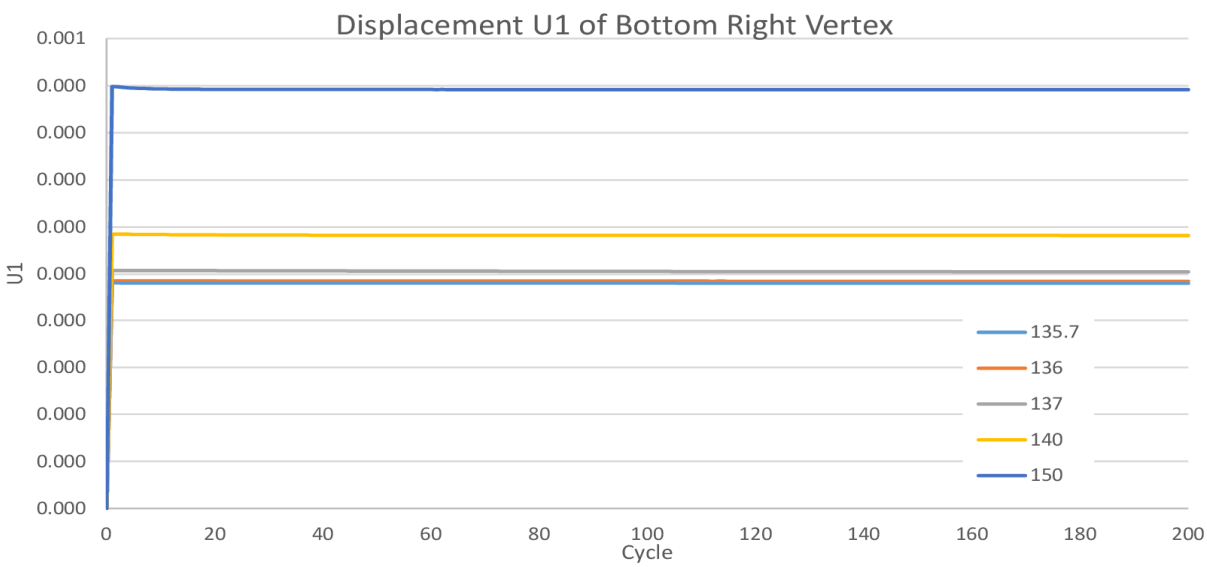

Figure 4.2.5: Maximum displacement for loads exceeding the shakedown limit.

Figure 4.2.6: Stress- Plastic strain diagrams for loads exceeding the shakedown limit.

Shakedown interaction diagram

Before the calculation of the points on the shakedown diagram, it is necessary to highlight an important property, which reduces the calculated points:

> The shakedown domain is convex. This is a very important property, which results from the convexity of the yield function. This ensures that it is always safe to approximate the exact diagram with linear interpolation between the calculated points.

However, in the current problem, the existing symmetries can reduce even more the calculated points for the construction of the domain. Note that:

- Due to the symmetry of the plate quarter with respect to the diagonal, the role of P_x and P_y can be alternated. This means that if the point (P_x, P_y) belongs to the shakedown diagram, the same must happen for (P_y, P_x). This gives symmetry with respect to the line $P_x = P_y$ (bisector of 1st and 3rd quadrants).
- Due to the symmetry of the material with respect to tension or compression, the point $(-P_x, -P_y)$ should also belong to the shakedown diagram. This gives symmetry about the origin.
- The combination of the two previous facts gives also that $(-P_y, P_x)$ also is a point on the shakedown domain. This gives symmetry with respect to the line $P_x = -P_y$ (bisector of 2nd and 4th quadrants).

The shakedown bounds are calculated with elastoplastic step-by-step analyses as described before and are shown on the following table

Table 4.1 Points of the calculated shakedown diagram.

$q=P_x/P_y$	P_x/σ_y	P_y/σ_y
1	0.48	0.48
1.5	0.53	0.35
2	0.56	0.28
3	0.59	0.20
∞	0.66	0.00
-3	0.59	-0.20
-2	0.56	-0.28
-1.5	0.53	-0.35
-1	0.48	-0.48

In Fig.4.2.7, the shakedown diagram for perfectly plastic material is shown, as it was calculated from the present procedure, and its comparison with other obtained diagrams in the literature. It should be noted that the curve obtained by the present procedure coincides with the one from the work of Huang et al. (2019). The perfect match of the two curves happens because both resulted

from calculations of the same FEM discretization. This shows that the present procedure can give identical results with the ones from a more sophisticated Direct Method. In the same diagram are also plotted the shakedown curves obtained from the work of Simon (2011), Chen et al. (2008) and Carvelli et al. The small differences occur because of the use of different models and methods in the various works.

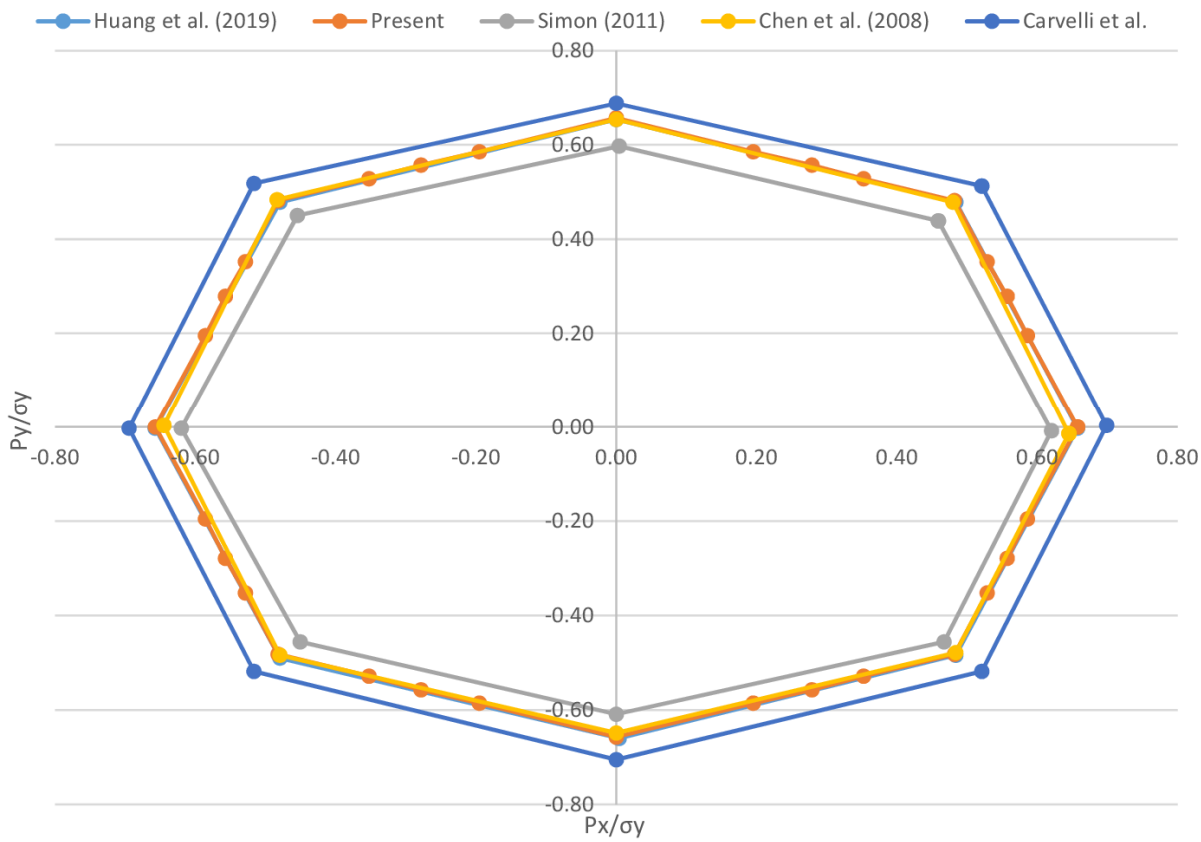

Figure 4.2.7: Comparison of Shakedown diagrams for perfectly plastic material.

Shakedown interaction diagram- Kinematic hardening material

In order to investigate the effect of linear kinematic hardening to the shakedown load, the same analyses were run with a linear hardening material. Fig 4.2.8 shows the shakedown diagram obtained from the present procedure and the one from the work of Huang et al. (2019) and their comparison. The figure shows a perfect match between the two curves, which happens because the same FEM discretization was used, as it was stated earlier.

It should be noted also that the shakedown curves for perfectly plastic and kinematic hardening material are identical. This was expected since the mode of inadaptation in this problem is alternating plasticity. This confirms that in cases where alternating plasticity occurs, there is no merit in modelling kinematic hardening material. Since in case of limit analysis the hardening effect would result in a much higher load, this seems a little strange at first glance. However,

there is a simple explanation why this happens in the case of alternating plasticity in shakedown analysis. The reason for this is that in areas of plasticity the stresses alternate between two different points of the yield surface, so in order to increase the applied load without inadaptation to set in, the yield surface needs to expand. But in the case of kinematic hardening, only translation and no expansion of the yield surface occurs.

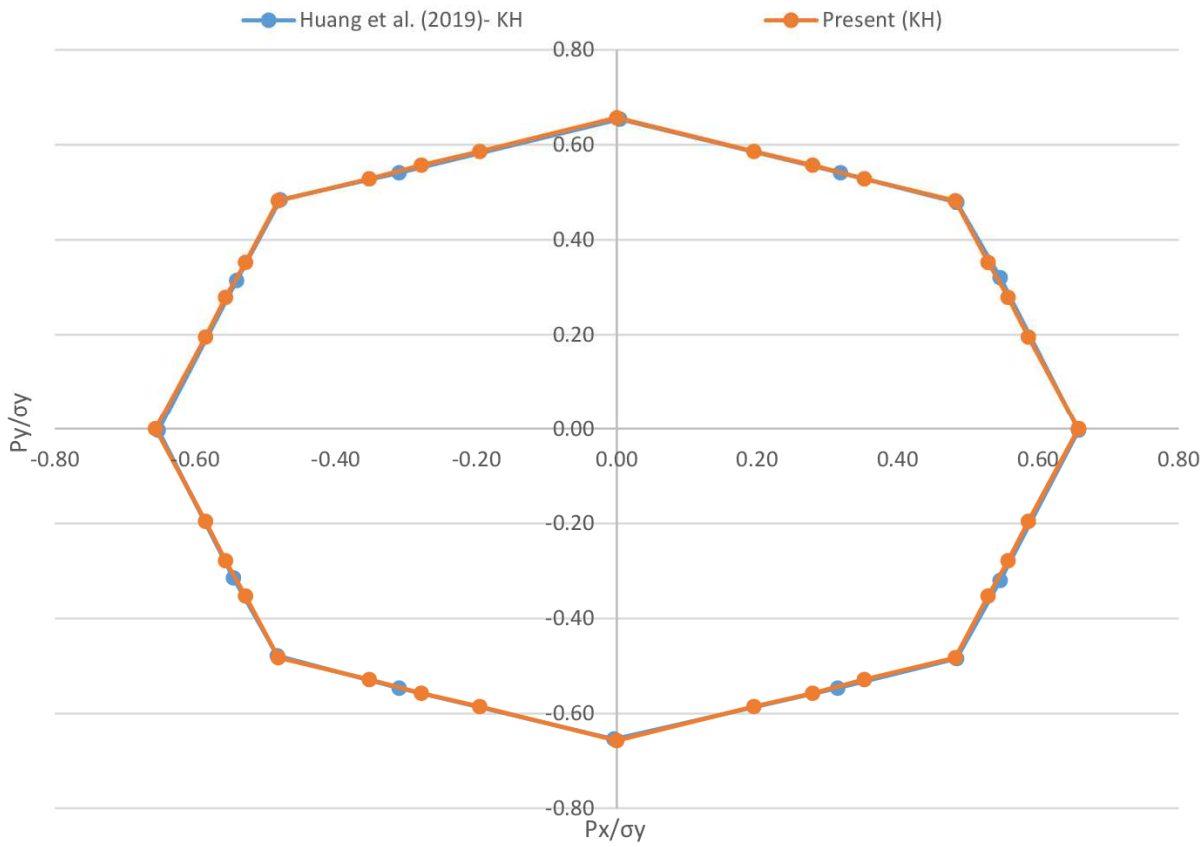

Figure 4.2.8: Comparison of Shakedown diagrams for linear kinematic hardening material.

4.3 Structure 2: Thin plate under tension and temperature

Problem definitions

This problem has investigated in Heitzer, Staat (2003), using a numerical approach based on the lower bound shakedown theorem, Heitzer et al. (2000) applied the basis reduction technique, whereas Schwabe (2000) used the program LANCELOT (Conn et al., 1992) based on the augmented Lagrangian method, and Mouhtamid (2007) used the interior-point algorithm IPDCA (Akoa et al., 2007).

Geometry: The square plate has the dimensions: $B \times L = 100 \times 100\ mm^2$, with thickness $t = 10\ mm$ and is supported vertically at the top and bottom sides, see Fig. 4.3.1.

Material: Young's modulus: $E = 200\ GPa$, yield stress: $\sigma_y = 205\ MPa$, hardening effect ${\sigma_u}/{\sigma_y} = 1.5$ for bounded hardening, poisson's ratio: $\nu = 0.3$, coefficient of thermal expansion $a_T = 1.6 \cdot 10^{-5}\ /K$

Loads: Uniform distributed tension $p\ (MPa)$ applied on the lateral sides, and uniform distributed temperature T (°C) on the plate, these loads vary in the domain: $p \in [0, p_{max}]$, $T \in [0, T_{max}]$, where p_{max} and T_{max} are the maximum values of tension and temperature respectively.

FEM model: The discretization consists of a $12 \times 12 \times 3$ rectangular grid with 432 C3D8 linear elements with $2 \times 2 \times 2$ integration rule.

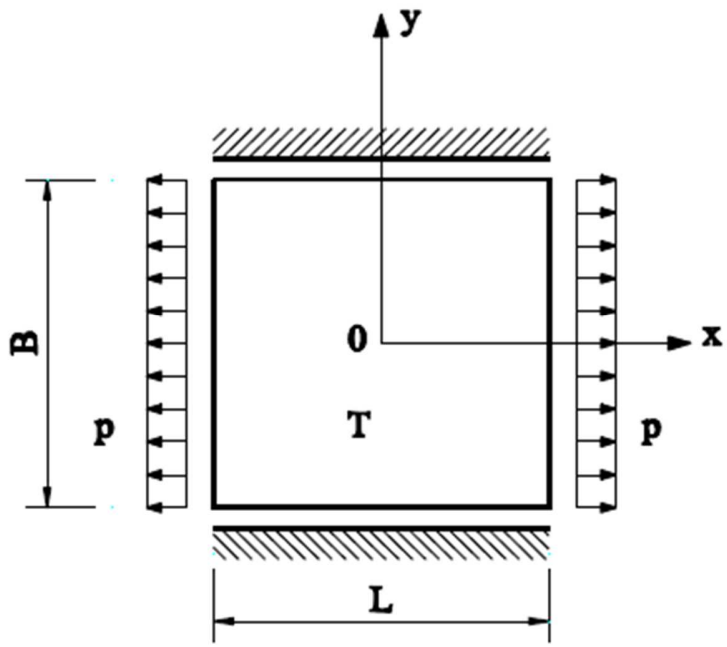

Figure 4.3.1: Thin plate under tension and temperature.

Elastic Analysis

The maximum elastic load for the mechanical tension is computed analytically as

$$p_{el} = \frac{1}{\sqrt{1-\nu+\nu^2}}\sigma_y$$

For the material parameters used in the present example: $p_{el} = 231\ MPa$

This agrees exactly with the numerical solution from ABAQUS.

On the other hand, the maximum elastic temperature variation:

$$T_{el} = \frac{1}{Ea_T}\sigma_y$$

which gives $T_{el} = 64$ °C. This value is also identical to the one obtained numerically from ABAQUS.

Shakedown Analysis- Perfectly Plastic Material

The analytical shakedown bound for pure tension is identical with the elastic load $p_0 = p_{el}$ (it is also equal with the limit load $p_{lim} = p_{el}$). The bound for pure temperature variation proves to be double the elastic one $T_0 = 2T_{el}$. Note, that limit analysis would predict an infinite bound for collapse. This shows that limit analysis is inappropriate for design of structures subjected to cyclic loads, with huge discrepancies in the case of thermal loads.

The points of the calculated shakedown diagrams are presented in table 4.2. and the shakedown diagram is presented in Fig. 4.3.2. Note that the shakedown diagram is normalized with the shakedown loads for pure tension and temperature, p_0 and T_0 respectively.

Table 4.2 Calculated shakedown bounds for perfectly plastic material.

Perfectly Plastyic	
p/p_0	T/T_0
0.00	1.00
0.30	0.91
0.55	0.83
0.71	0.71
0.80	0.60
0.90	0.45
0.98	0.25
1.02	0.00

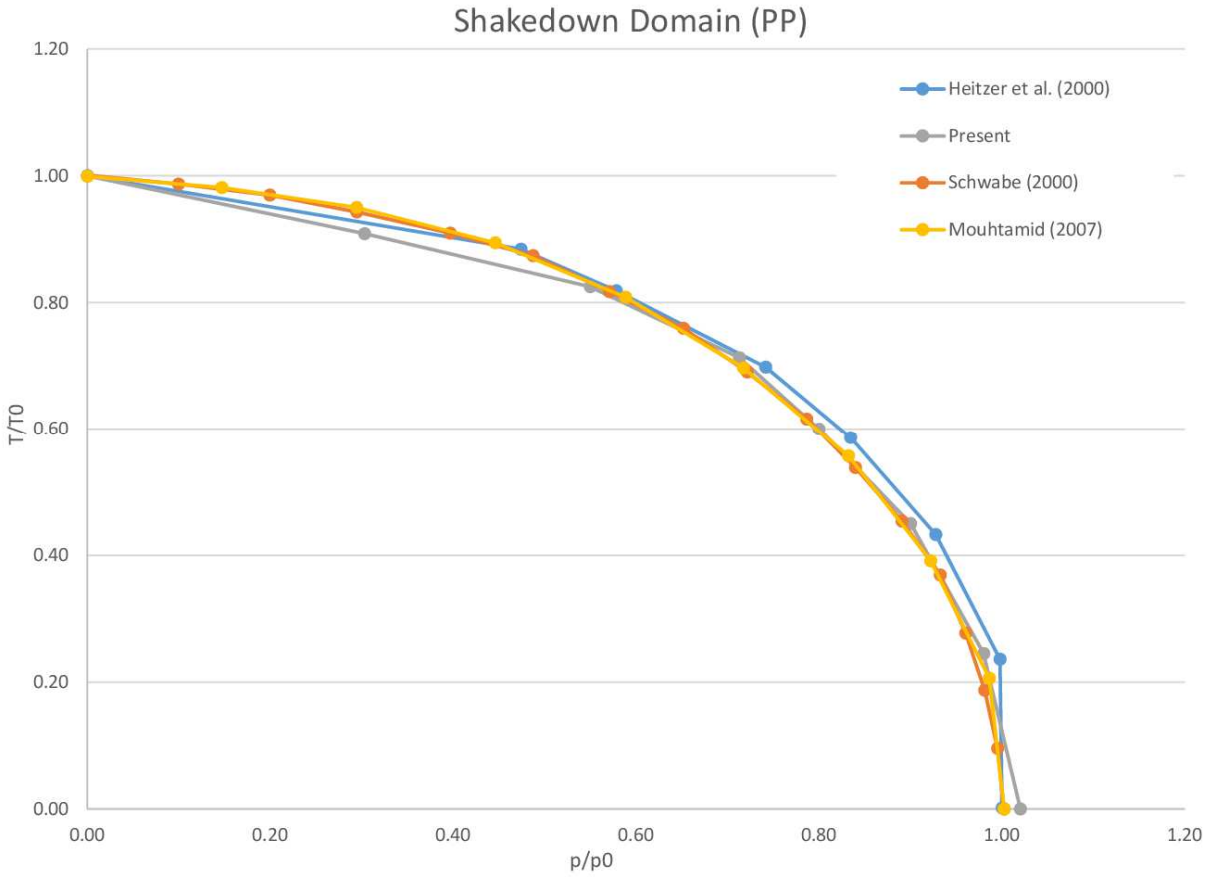

Figure 4.3.2: Comparison of Shakedown diagrams for perfectly plastic material.

<u>Shakedown Analysis- Kinematic Hardening Material</u>

The case of kinematic hardening material presents great interest in this example. For the investigation of the effect of hardening on the shakedown domain, it is assumed that

$$\sigma_u / \sigma_y = 1.5$$

Here are presented the results of the calculations after 1000 cycles for the case with $\frac{T/T_0}{p/p_0} = 1$ for different scale factors a for the investigation of the shakedown boundary.
Fig. 4.3.3 shows the plastic dissipation of the structure for 5 different scale factors a over 1000 cycles of loading. It is difficult to decide which is the maximum value of a for which the total plastic dissipation of the structure remains bounded. It is clear that for $a = 0.75$ the plastic dissipation of the structure $W_p = \int_0^t \int_V D_p\left(\dot{\varepsilon}_p\right)$ converges to a finite value. On the other hand for the case $a = 0.85$ $W_p$will not reach a finite value and diverges. However, as a gets closer to the shakedown boundary, it gets more difficult to decide whether W_p will stabilize, since this may happen after a great number of cycles.

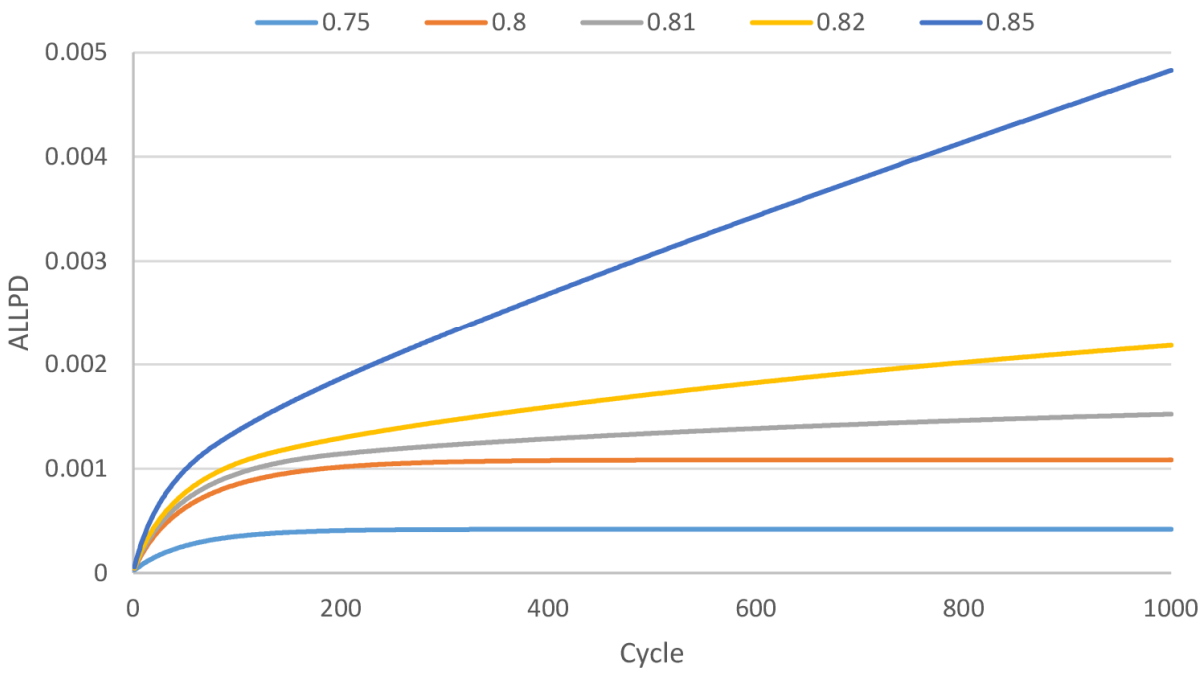

Figure 4.3.3: Total plastic dissipation for different scale factors.

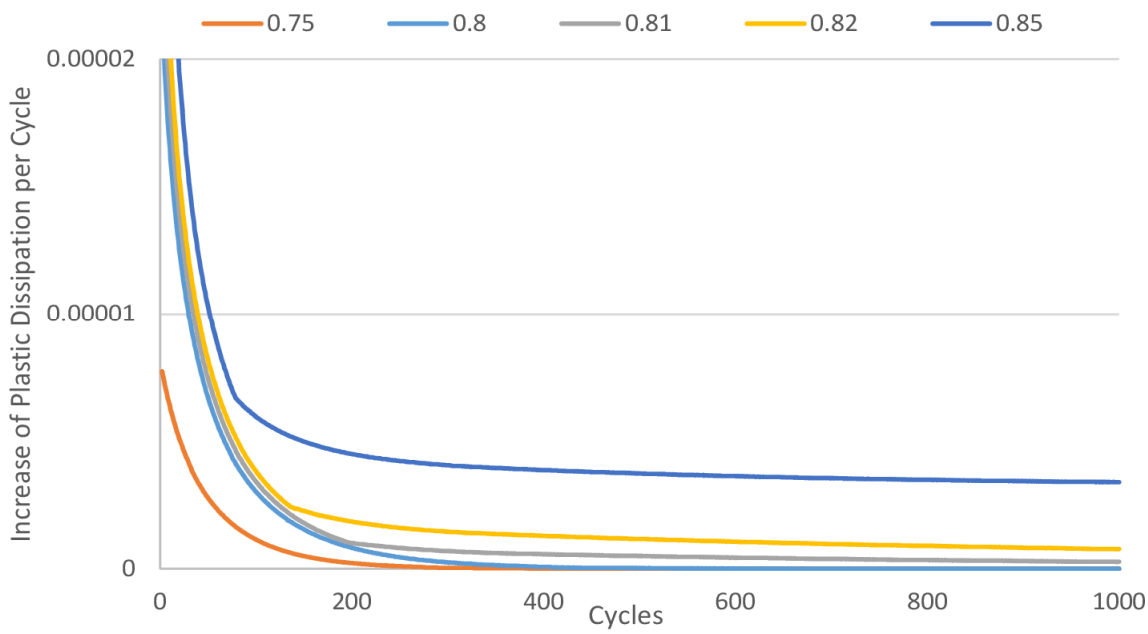

Figure 4.3.4: Increase of total plastic dissipation per cycle for different scale factors.

The increase of the total plastic dissipation per cycle is given in Fig. 4.3.4. If this increase approaches a limit value greater than zero, then this means inadaptation. However, it is difficult to decide whether the limit value is equal or greater than zero.

In order, to overcome this difficulty and decide whether the total plastic dissipation will remain bounded, it is investigated if W_p converges faster than the harmonic series

$$\sum_{n=1}^{\infty} an^s \ \ with\ s < -1$$

where a, s are constants and n is the cycles of loading.

The case of LCF or ratchetting leads to infinite plastic dissipation $(W_p \to \infty)$. This means that in a double logarithmical diagram of the loading cycles and the increase of plastic dissipation, noted as $\Delta W_p(n) = W_p(n) - W_p(n-1)$, that the slope must exceed $s = -1$.

This idea was proposed by Heitzer, Staat, Reiners & Schubert (2003) to determine if some experiments lead to inadaptation or shakedown.

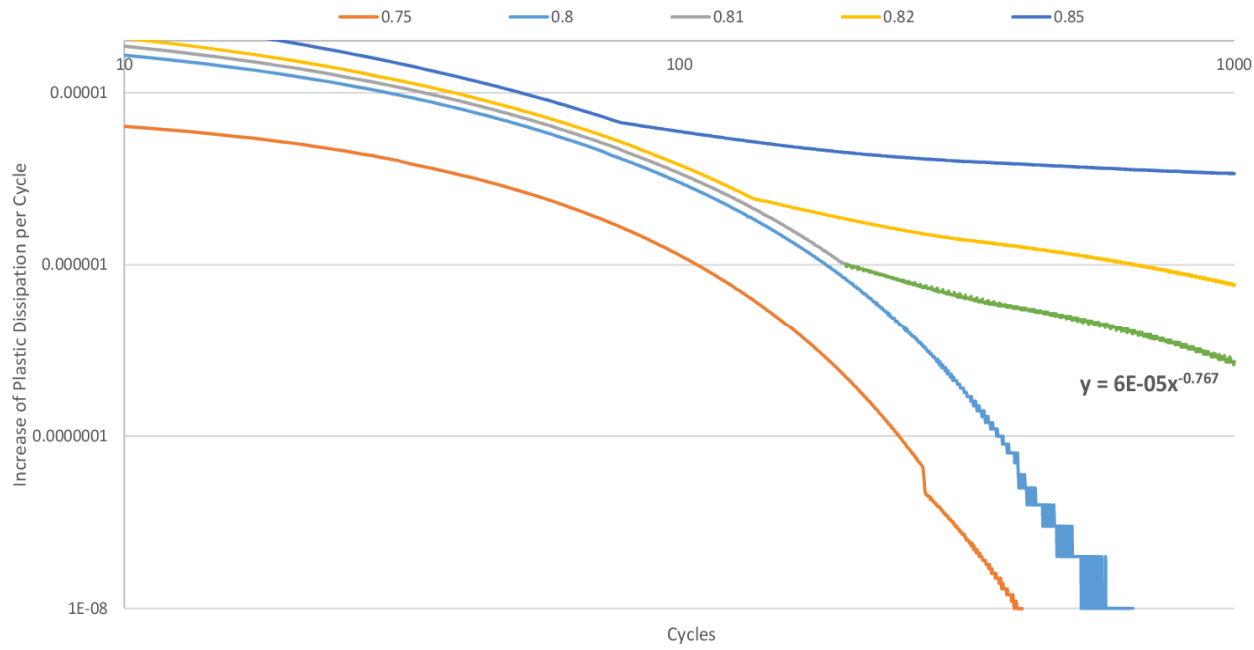

Figure 4.3.4: Increase of total plastic dissipation per cycle in double logarithmic axis.

Figure 4.3.4 shows the increase of total plastic dissipation per cycle in double logarithmic axis. It is clear that the cases $a = 0.75$ and $a = 0.80$ lead to shakedown and cases $a = 0.81$, $a = 0.82$ and $a = 0.85$ lead to inadaptation because $s > -1$. On the same figure has been fitted a power function of the form an^s (linear in double logarithmic diagram) with $s = -0.767 > -1$. Note that the slope of this case changes abruptly around 200 cycles. So if the load history had small duration, then this case would have been regarded as adaptation.

The previous lead to the conclusion that the results obtained here are highly affected by the number of cycles of loading analyzed. If the accuracy needed of the interaction diagram is high, then a lot of cycles should be analyzed with high computation cost. In the present examples the

number of cycles analyzed each time is chosen such that it gives descent accuracy. This is confirmed by the fact that the calculated results agree well with the ones given in the literature.

Table 4.3 Calculated shakedown bounds for kinematic hardening material.

Kinematic Hardening	
p/p_0	T/T_0
0.00	1.00
0.31	0.93
0.58	0.87
0.80	0.80
0.99	0.74
1.24	0.62
1.36	0.54
1.46	0.37
1.54	0.00

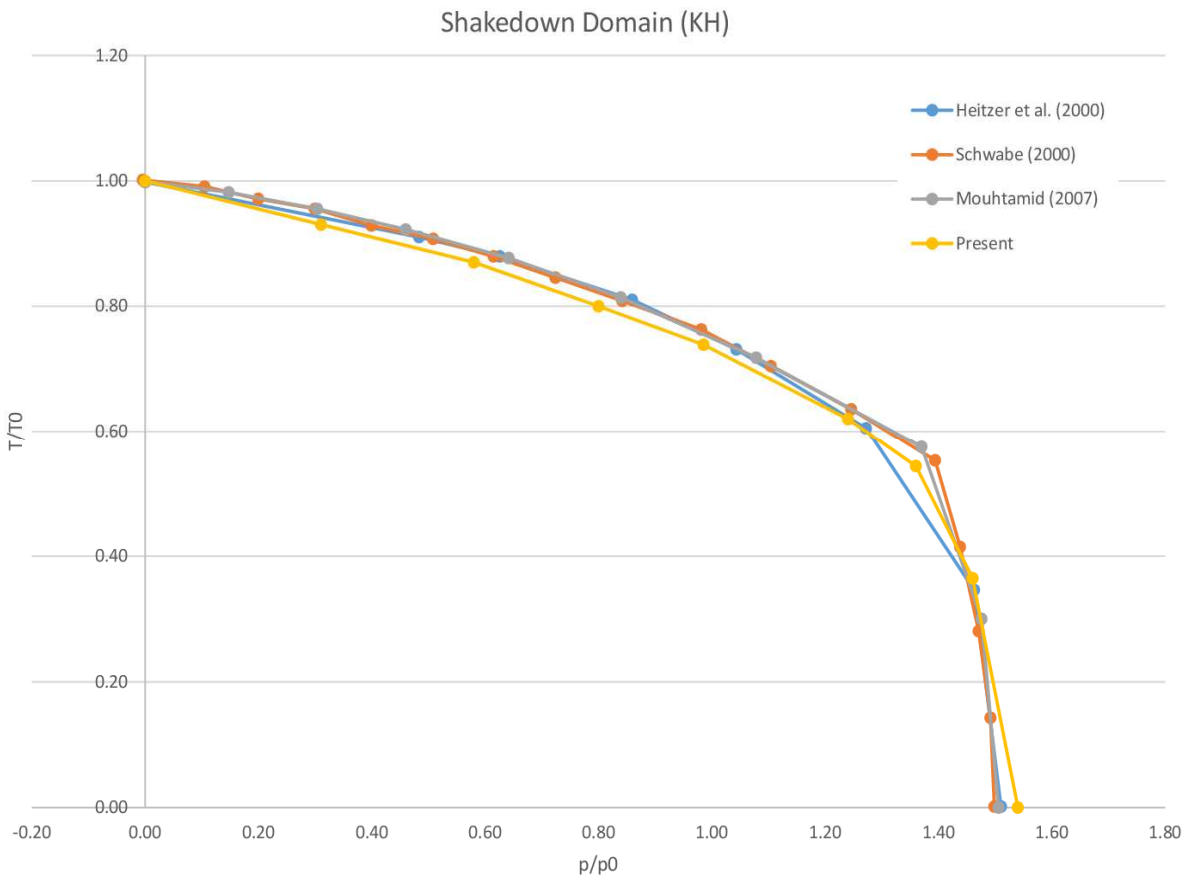

Figure 4.3.5: Comparison of Shakedown diagrams for kinematic hardening material.

The comparison of the obtained results (Table 4.3) with the results obtained by Heitzer et al. (2000) Schwabe (2000) and Mouhtamid (2007) shows good agreement. Generally, the present shakedown diagram is on the safe side, which was expected since the exact diagram would be obtained by analysis over infinite number of cycles. The small excess in the case of pure tension is due to numerical errors.

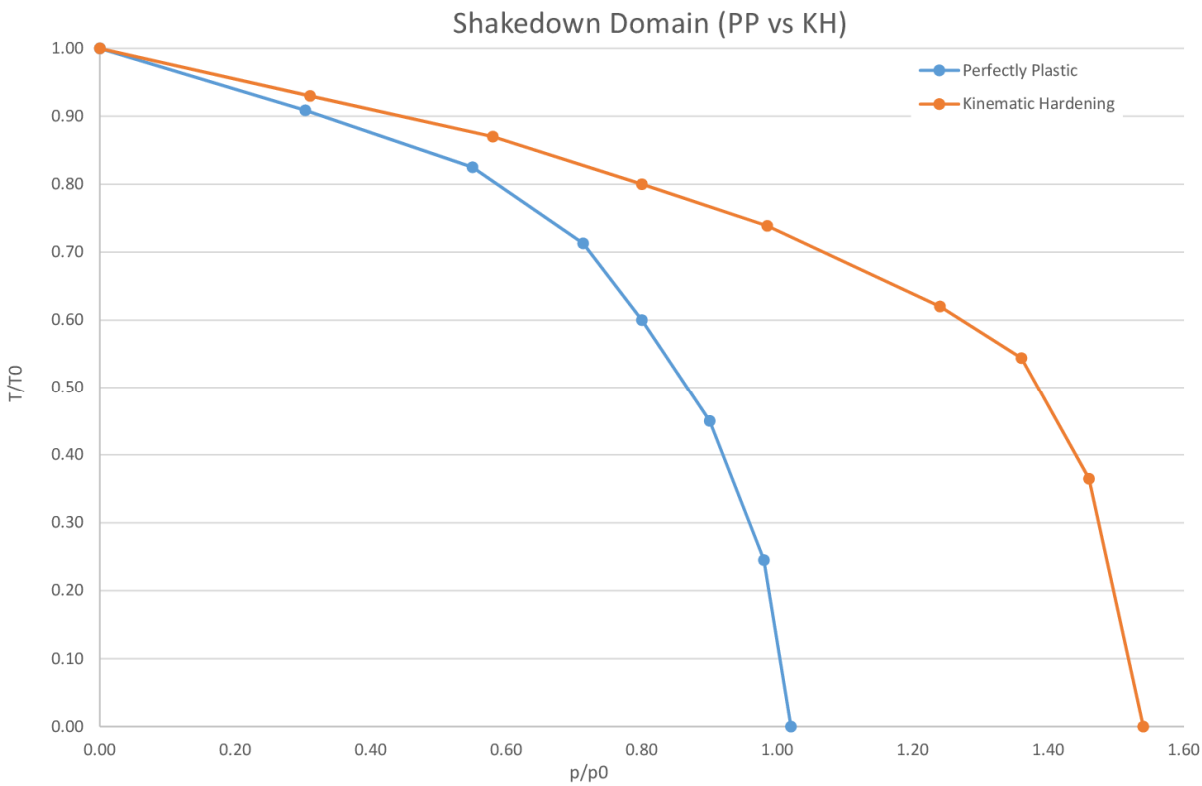

Figure 4.3.6: Comparison of perfect plasticity & kinematic hardening.

The effect of kinematic hardening is illustrated in fig. 4.3.6 where both the shakedown domains for perfect plasticity and kinematic hardening are plotted. Before the comparison, it is necessary to remember here an important inequality for the scale factor:

$$a_{sh}^{pp} \leq a_{sh}^{blkh} \leq \frac{\sigma_u}{\sigma_y} a_{sh}^{pp}$$

where a_{sh}^{pp} is the shakedown factor for perfectly plastic material and a_{sh}^{blkh} is the shakedown factor for kinematic hardening material.

The lower bound inequality holds for the case of alternating plasticity mode of failure, whereas the upper bound is obtained for the case of incremental collapse. This explains also the fact that

$$a_{lim}^{blkh} = \frac{\sigma_u}{\sigma_y} a_{lim}^{pp}$$

, since in limit analysis the mode of failure of alternating plasticity is excluded.

In figure 4.3.6 the following important observations can be made:

- For pure thermal loading, the mode of failure is alternating plasticity, thus there is no benefit form kinematic hardening.
- For pure tension loading, the mode of failure is incremental collapse, thus shakedown scale factor takes its upper bound and equals $\frac{\sigma_u}{\sigma_y} = 1.5$ times the factor of PP material.
- For in-between cases where there are both thermal and mechanical loads, the scale factor takes the in-between of the previous inequality.

4.4 Structure 3: Tension-torsion experiment

Problem definitions

The hollow steel bar is subjected to tension force N and torsion moment M. This problem is investigated by Heitzer et al. (2003), Staat, Heitzer (2002) by both experiment and FE analysis, Their FE results compare well to analytical solutions for linear and nonlinear kinematic hardening obtained for bounded linear kinematic hardening and linear kinematic hardening with the Amstrong-Frederick model respectively (see Staat, Heitzer (2002)). The same problem has been also addressed numerically by Pham & Staat (2010) with an upper bound algorithm for bounded linear kinematic hardening. Recently, Huang et al. (2019) have also deal with this problem. They used an interior point algorithm for the solution of the optimization problem resulting from a lower bound approach.

Geometry: The structure of the test specimen is described in Fig. 4.4.1, with the dimensions in mm.

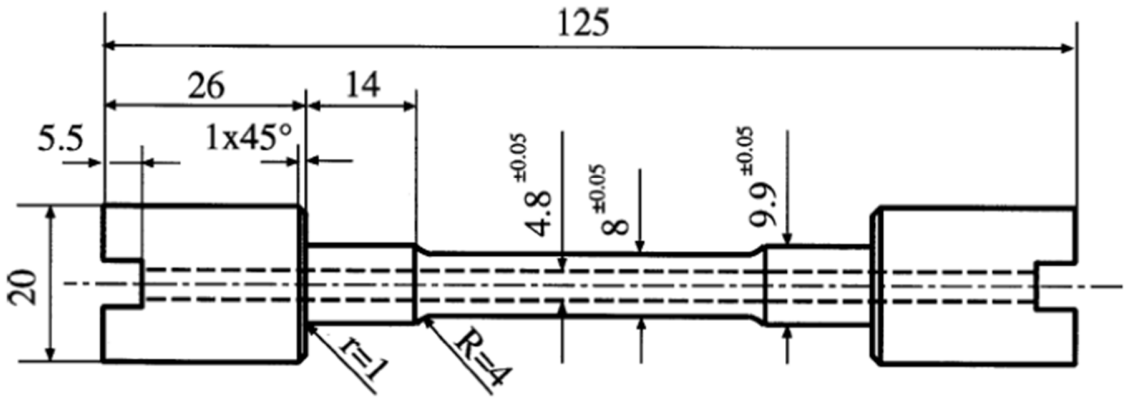

Figure 4.4.1: Specimen dimensions.

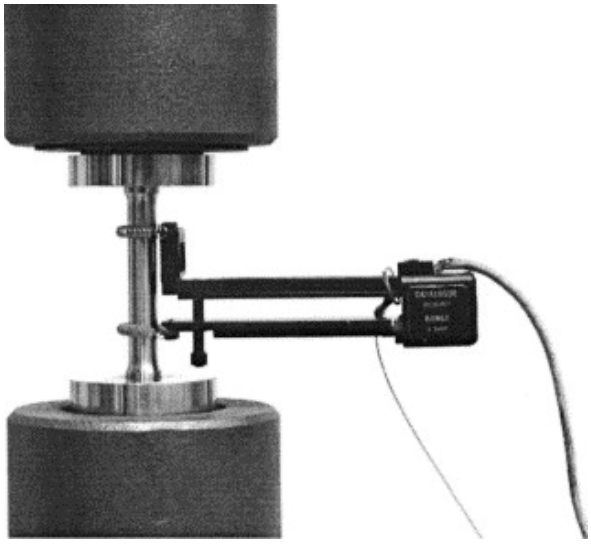

Figure 4.4.2: Experiment layout.

Material: Young's modulus: $E = 207\ GPa$, yield stress: $\sigma_y = 485\ MPa$, ultimate stress $\sigma_u = 631\ MPa$ for bounded hardening, poisson's ratio: $\nu = 0.3$

Loads: The specimen is subjected to constant torsion and cyclic tension with zero mean stress.

$$M = constant, \qquad N \in [-N_{max}, N_{max}]$$

FEM model: Only half of the structure is analysed taking advantage of symmetry. The mesh consists of 896 linear hexahedral elements of the type C3D8, according to figure 4.4.3. For the critical part of the central region, three elements through the thickness were used. The mesh density was taken from Huang et al. (2019).

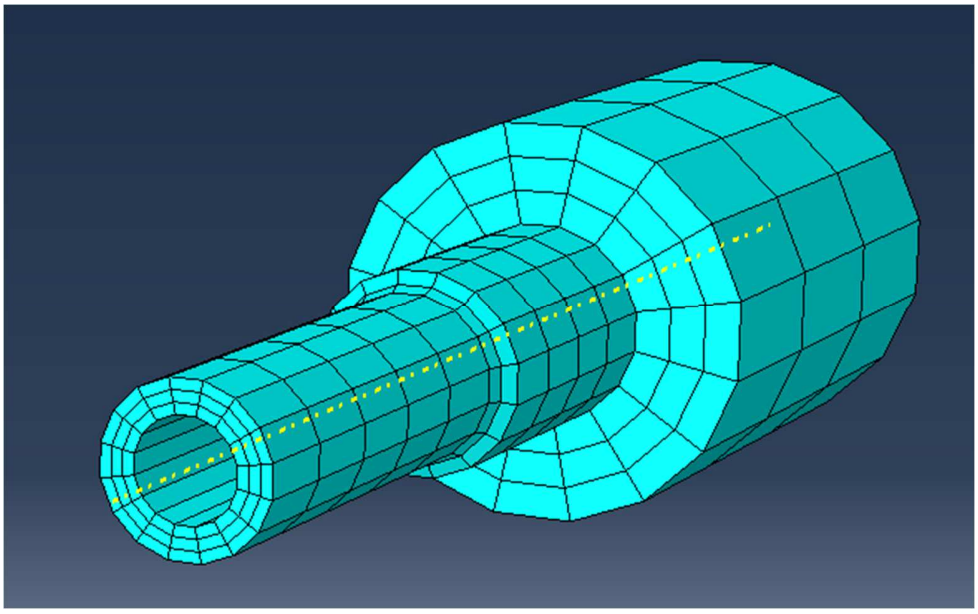

Figure 4.4.3: FEM Discetization.

Analytical solutions

The analytical solutions for this structure can be cited from Heitzer et al. (2003), and presented hereafter:

Elastic analysis

For pure torsion and axial symmetry, the normal stress vanishes and only shear stresses

$\tau(r) = \sigma_{\theta z}(r)$ occur. The stress for moment M at the radius r is calculated as:

$$\tau(r) = \sigma_{\theta z}(r) = \frac{2M}{\pi(r_e^4 - r_i^4)} r$$

The maximum shear stress is at the outer radius. For $r_e = 4\ mm$ and $r_i = 2.4\ mm$ then:

$$\tau_{max} = \tau(r_e) = \frac{2M}{\pi(r_e^4 - r_i^4)}\ r_e = \frac{M}{87.5}\ {}^{1}/_{mm^3}$$

with the equivalent von Mises stress $\sigma_{eq} = \sqrt{3}\tau_{max}$ and the structure starts yielding at:

$$M_{el} = 87.5\ mm^3 \cdot \frac{\sigma_y}{\sqrt{3}} = 87.5 \cdot \frac{485}{\sqrt{3}}\ Nmm = 24501\ Nmm$$

Limit analysis

Pure tension capacity is easily calculated:

- for perfectly plastic material:

$$N_{lim}^{pp} = N_{pl} = \pi(r_e^2 - r_i^2)\sigma_y = \pi(4^2 - 2.4^2) \cdot 485\ N = 15602\ N$$

- for bounded linearly kinematic hardening material:

$$N_{lim}^{blkh} = \left({}^{\sigma_u}/_{\sigma_y}\right) N_{lim}^{pp} = \left({}^{631}/_{485}\right) \cdot 15602\ N = 20299\ N$$

Pure torsion capacity:

- for perfectly plastic material: M_{lim}^{pp} is obtained from elastic moment M_{el} with plastic limit load factor η_{pl}

$$\eta_{pl} = \frac{4}{3} \cdot \frac{1 - \left({}^{r_i}/_{r_e}\right)^3}{1 - \left({}^{r_i}/_{r_e}\right)^4} = \frac{4}{3} \cdot \frac{1 - \left({}^{2.4}/_{4}\right)^3}{1 - \left({}^{2.4}/_{4}\right)^4} = 1.2$$

Then $M_{lim}^{pp} = M_{pl} = \eta_{pl} \cdot M_{el} = 1.2 \cdot 24501\ Nmm = 29402\ Nmm$

- for bounded linearly kinematic hardening material:

$$M_{lim}^{blkh} = \left({}^{\sigma_u}/_{\sigma_y}\right) M_{lim}^{pp} = \left({}^{631}/_{485}\right) \cdot 29402\ Nmm = 38222\ Nmm$$

Numerical results

Elastic analysis:

Before the use of the model for nonlinear analyses, the results of linear elastic analyses are verified. Figures 4.4.4 & 4.4.5 show the Mieses stress distribution for tension $N = 1000\ N$ & torsion $M = 1000\ Nmm$ loading respectively. The numerical elastic tension & torsion loads compare well with the analytical ones.

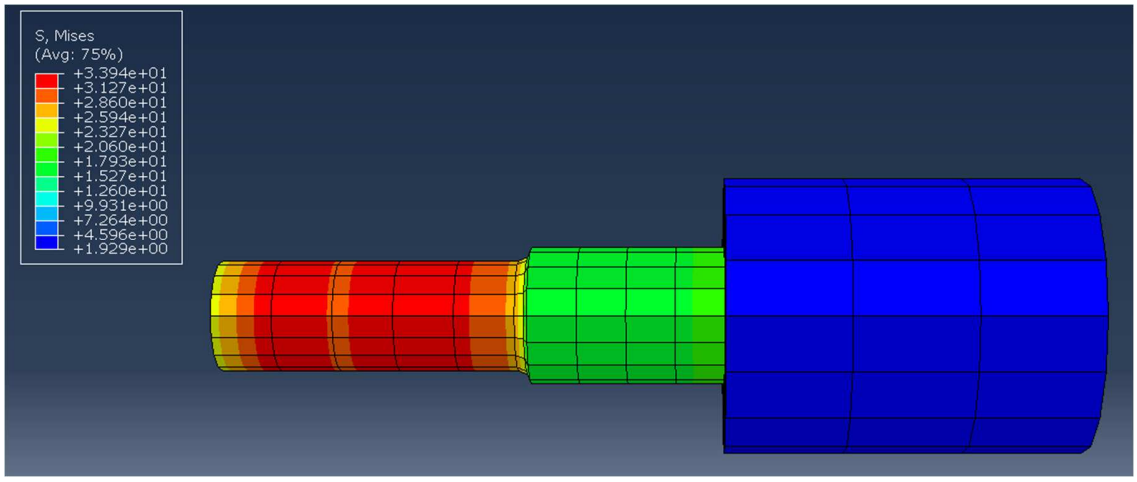

Figure 4.4.4: Elastic stress field for tension loading.

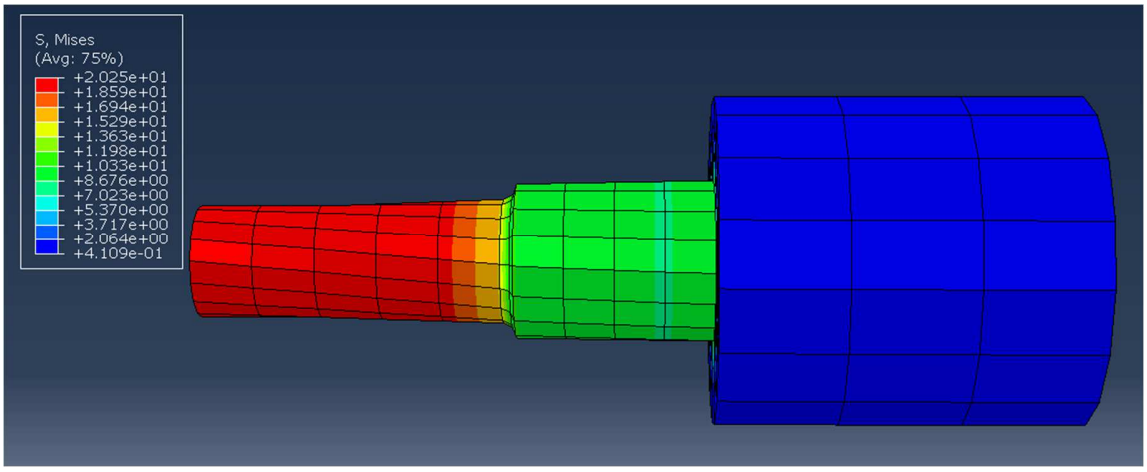

Figure 4.4.5: Elastic stress field for torsion loading.

Shakedown Analysis- Perfectly Plastic Material

For the reason of comparison, the shakedown bounds are normalized by $N_{z0} = 15602\ N$ and $M_{z0} = 27980\ Nmm$, taken from Heitzer *et al.* (2003).

Here, the time-stepping solution will be presented only for the case with $\frac{M/M_{z0}}{N/N_{z0}} = 1$

In order to reduce the time consumed for the process and the interpretation of the results for the determination of the shakedown bounds the loading history is constructed in the following way. Instead of imposing different loading histories and increasing each time the maximum values, only one loading history is simulated with increasing maximum values after a certain number of cycles. For the case with $\frac{M/M_{z0}}{N/N_{z0}} = 1$ the loading history is shown in figure 4.4.6 for 3 levels of loading and 20 cycles for each level.

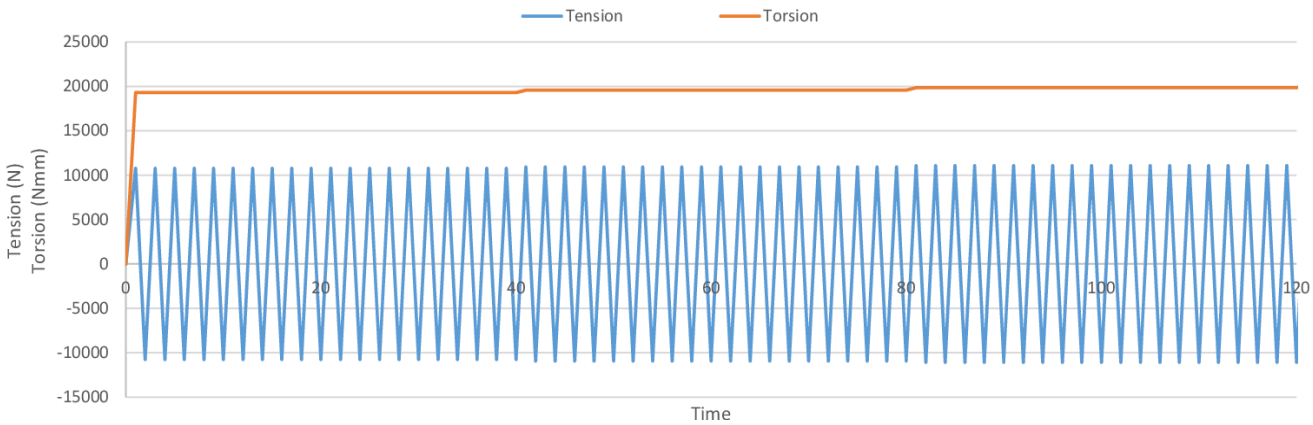

Figure 4.4.6: Cyclic loading histories.

The plastic dissipation for the above loading history is presented in Fig. 4.4.7.

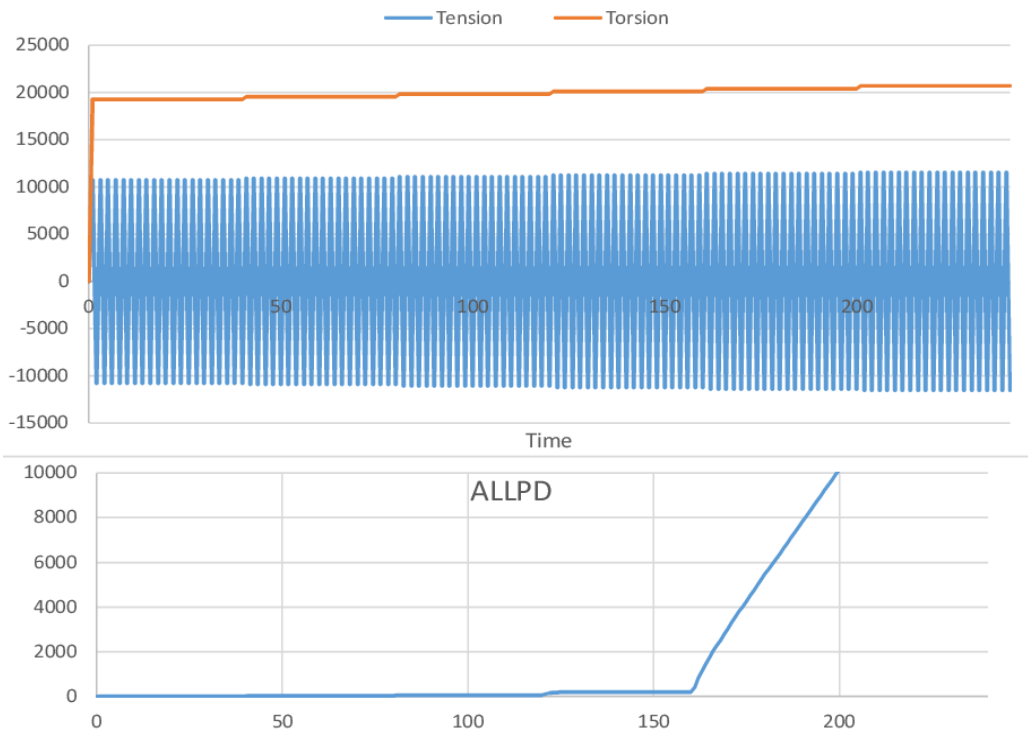

Figure 4.4.7: Plastic Dissipation.

Figure 4.4.7 shows that for the 4th level $a = {}^{M}/_{M_{z0}} = {}^{N}/_{N_{z0}} = 0.73$ of loading the plastic dissipation diverges, which corresponds to inadaptation. On the other hand, for the 3rd level $a = {}^{M}/_{M_{z0}} = {}^{N}/_{N_{z0}} = 0.72$ the plastic dissipation remains bounded, which means that the shakedown bound for this case is $a_{sh}^{pp} = 0.72$. The mode of inadaptation is incremental collapse.

In this way, the shakedown bounds for different ratios $\frac{{}^{M}/_{M_{z0}}}{{}^{N}/_{N_{z0}}}$ are calculated and given in table 4.4.

Table 4.4 Calculated shakedown bounds for perfectly plastic material.

Present-PP	
N/N_{z0}	M/M_{z0}
0.00	1.06
0.26	1.02
0.46	0.92
0.57	0.86
0.72	0.72
0.81	0.61
0.89	0.45
0.95	0.24
0.97	0.00

The shakedown interaction diagram is presented in Fig. 4.4.8. On the same figure are drawn the diagrams taken from Heitzer et al. (2003), Pham & Staat (2013) and Huang et al. (2019) for comparison.

The diagram obtained by the present elastoplastic time history analyses, compares really well with others given in literature. The coarse mesh of Huang et al. was used here. This explains the good comparison between the two lines in general.

The discrepancies between the various diagrams are due to the different FEM discretization and also different (lower or upper) bound approach in each work.

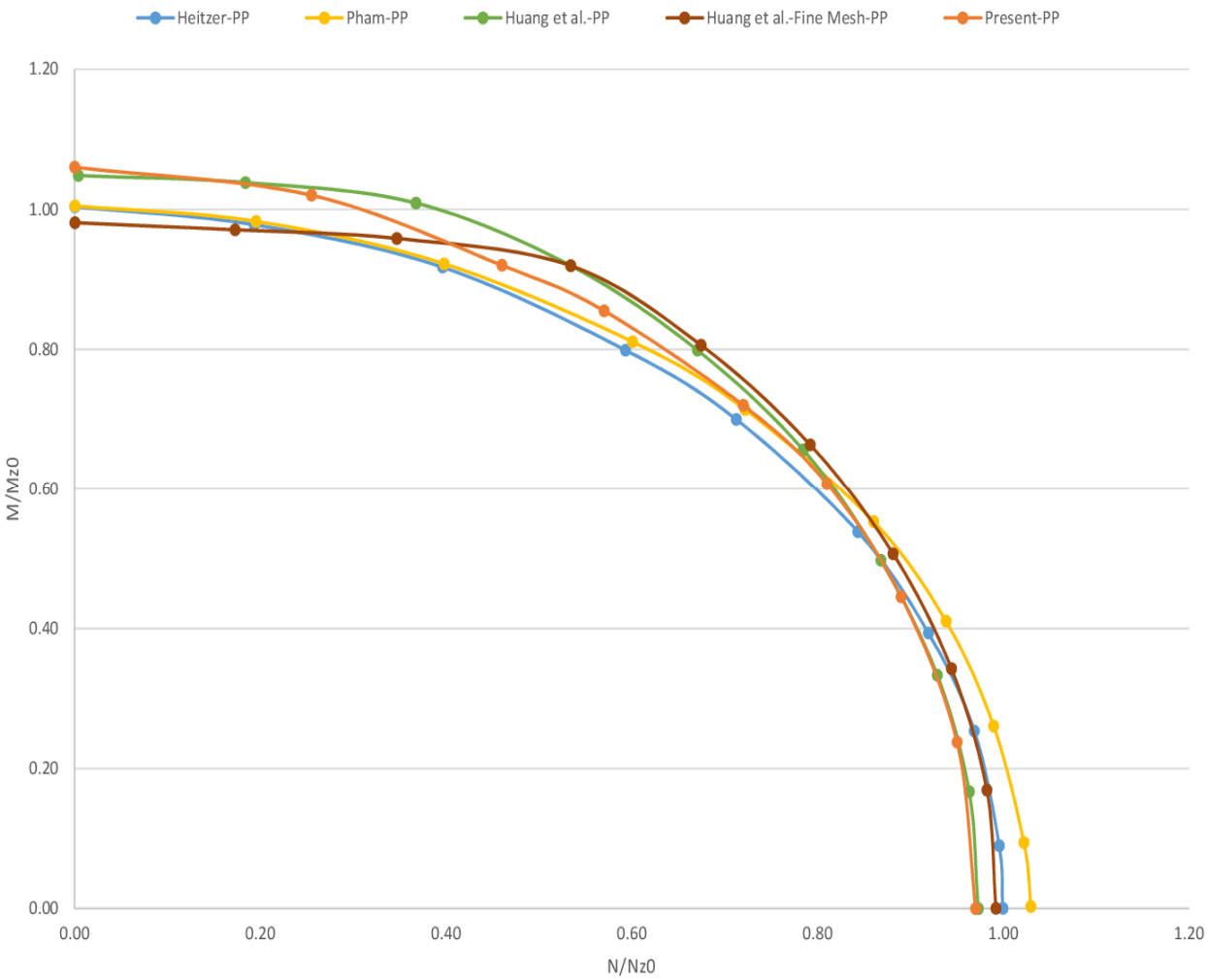

Figure 4.4.8: Shakedown domains for perfectly plastic material.

<u>Shakedown Analysis- Bounded Linear Kinematic Hardening</u>

The same procedure is repeated for the more realistic case of kinematic hardening. The results are presented on table 4.5. Here, it is reminded that the load factor for kinematic hardening should satisfy the following inequality:

$$a_{sh}^{pp} \leq a_{sh}^{blkh} \leq \frac{\sigma_u}{\sigma_y} a_{sh}^{pp}$$

However, for the inadaptation mode of incremental collapse the right hand side should hold as equality. This means that the numerical results must satisfy:

$$a_{sh}^{blkh} = \frac{\sigma_u}{\sigma_y} a_{sh}^{pp}$$

It is evident that in this case the benefit from the hardening effect is maximized.

Table 4.5 Calculated shakedown bounds for kinematic hardening material.

Present-KH	
N/N_{z0}	M/M_{z0}
0.00	1.37
0.33	1.32
0.60	1.20
0.74	1.11
0.93	0.93
1.05	0.79
1.16	0.58
1.23	0.31
1.26	0.00

The following figure (Fig. 4.4.9) presents the results of table 4.5 and the comparison with shakedown diagrams obtained by others.

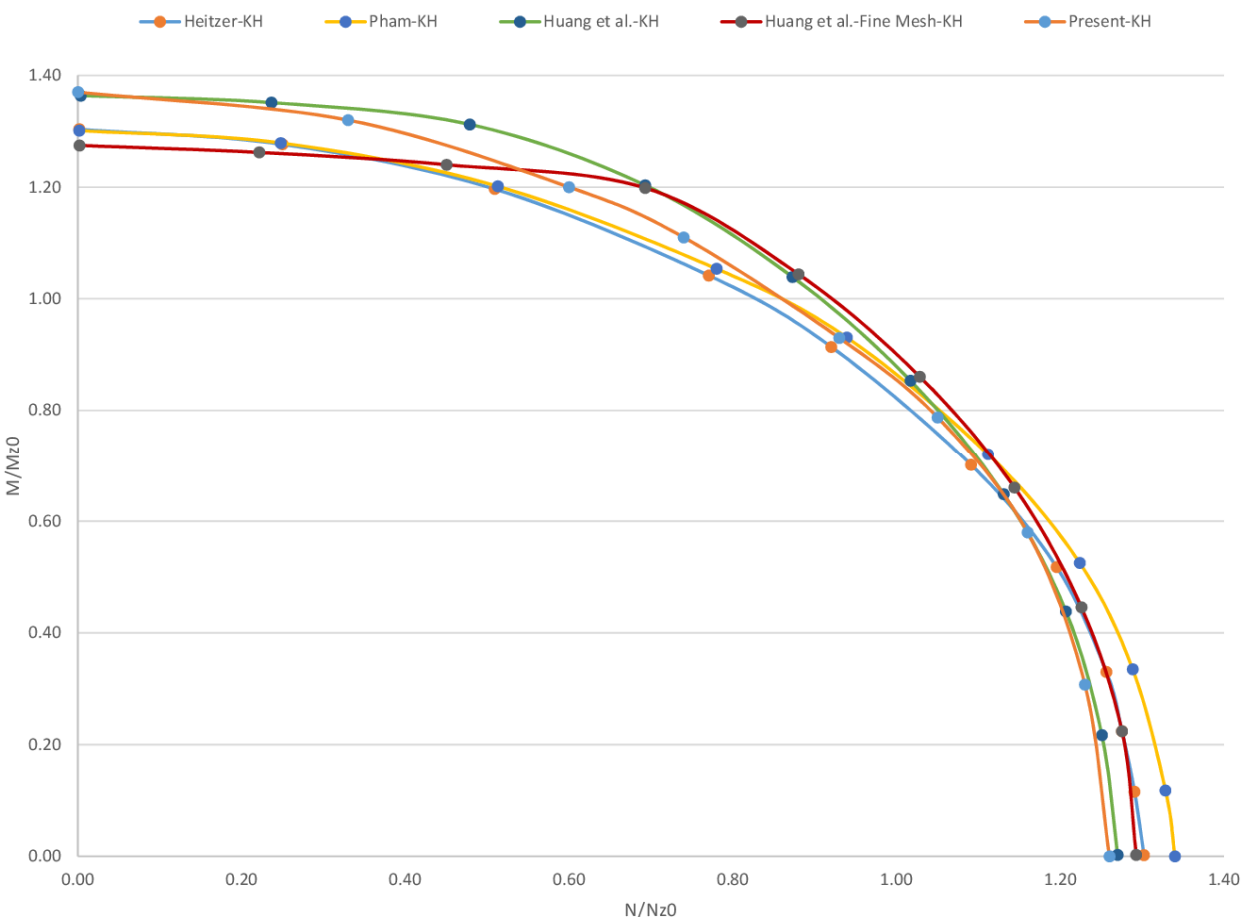

Figure 4.4.9: Shakedown domains for kinematic hardening material.

The benefit of the kinematic hardening is obvious in figure 4.4.10. The equality $a_{sh}^{blkh} = \frac{\sigma_u}{\sigma_y} a_{sh}^{pp}$ holds for the numerical results obtained. In the same figure, the loads investigated experimentally by Heitzer et al. are plotted for comparison. The experiments try to capture the region of shakedown and ratchetting. It should be noted that the assumption of perfect plasticity gives always safe bounds. However, the discrepancy with the actual bound is significant. On the other hand, the bounded linear kinematic hardening gives higher bounds than the actual ones. This is due to the fact that linear kinematic hardening is an idealization of the actual response. A model closer to the actual behaviour would be one with nonlinear kinematic hardening (such as the Armstrong-Frederick model) which would give lower shakedown bounds in general.

However, the use of a nonlinear hardening like the Armstrong-Frederick one is more difficult since it needs experimental data for calibration. The yield and ultimate stresses, though, are always known and can be used for the calibration of a linear hardening model.

The agreement between numerical & experimental results is reasonable.

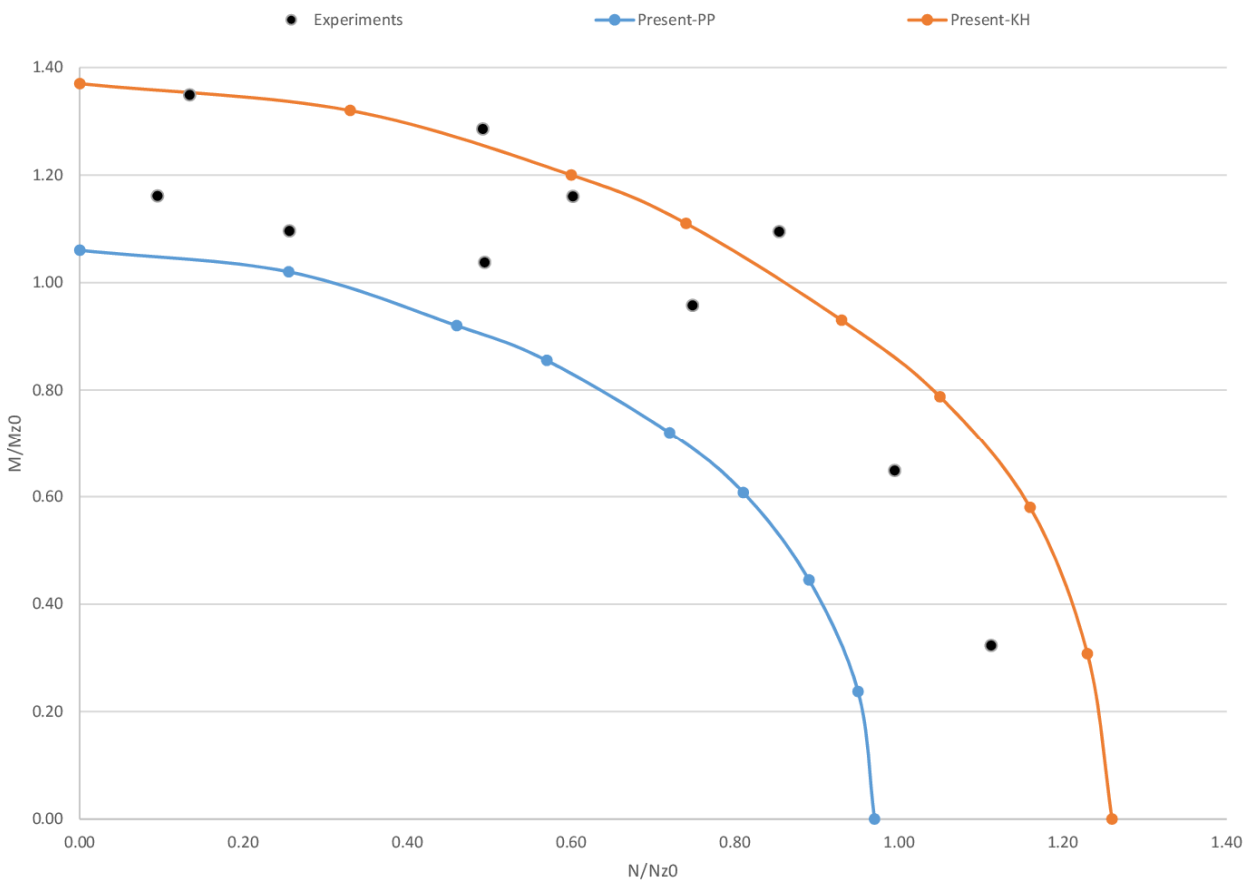

Figure 4.4.10: The benefit of kinematic hardening & the comparison with experimental results.

4.5 Structure 4: Thin pipe subjected to thermo-mechanical loading

Problem definitions

This problem is taken from the area of power plant engineering. The aim is the determination of the shakedown bounds of a thin pipe with an internal pressure and a temperature difference between the inside and the outside of the pipe. The perfectly plastic and unlimited hardening case were investigated by Mouhtamid (2007) using the interior-point algorithm IPDCA (Akoa et al., 2007). Furthermore, limited hardening was considered by Hachemi (2005), who applied the BFGS algorithm (Morris, 1982), and by Heitzer et al. (2000) utilizing the basis reduction technique. Recently, Simon (2013) used an interior point algorithm for the solution of the optimization problem resulting from a lower bound approach.

Geometry: The pipe has a thin cylindrical shape with ${}^{R}/_{h} = 10$ and ${}^{R}/_{L} = 2$.

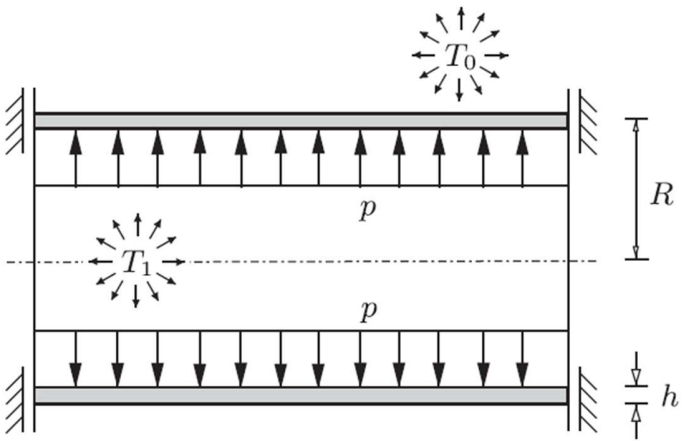

Figure 4.5.1: Thin pipe with thermos-mechanical loading

Material: Young's modulus: $E = 200\ GPa$, yield stress: $\sigma_y = 205\ MPa$, hardening effect ${}^{\sigma_u}/_{\sigma_y} = 1.5$ for bounded hardening, poisson's ratio: $\nu = 0.3$, coefficient of thermal expansion $a_T = 1.6 \cdot 10^{-5}\ /K$

Loads: The pipe is subjected to independently varying internal pressure and thermal loading with non-zero mean values.

$$p \in [0, p_{max}], \qquad T \in [0, T_{max}]$$

FEM model: Only half of the structure is analysed taking advantage of symmetry. The mesh consists of 600 linear hexahedral elements of the type C3D8. In order to get adequate results, 5 elements through the thickness of the shell are used. The mesh density was taken from Simon (2013). It is noted that due to the thickness of the pipe the temperature distribution is assumed linear.

Elastic Analysis

First, a linear model is run with pure mechanical and pure thermal loadings for the verification of the model. Figures 4.5.2 & 4.5.3 show the elastic stress fields for the pure loadings of arbitrarily chosen values $p = 10\ MPa$ and $T = 100\ MPa$ respectively.

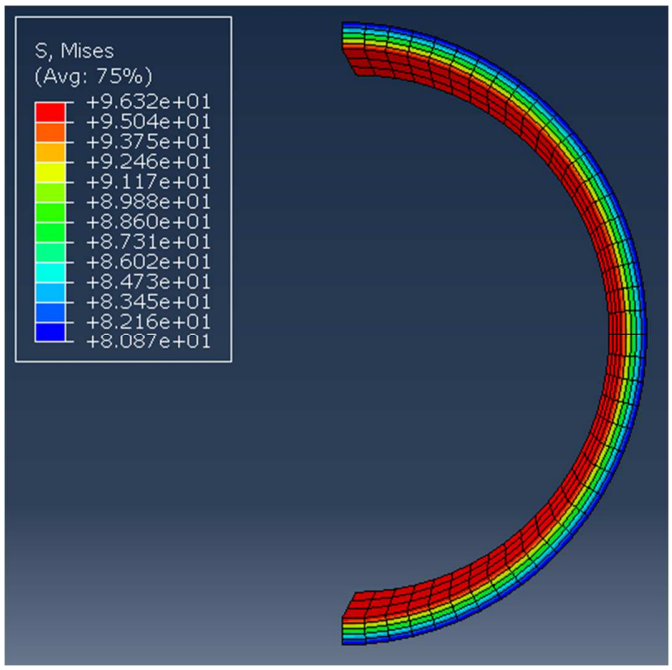

Figure 4.5.2: Elastic stress field for pure pressure.

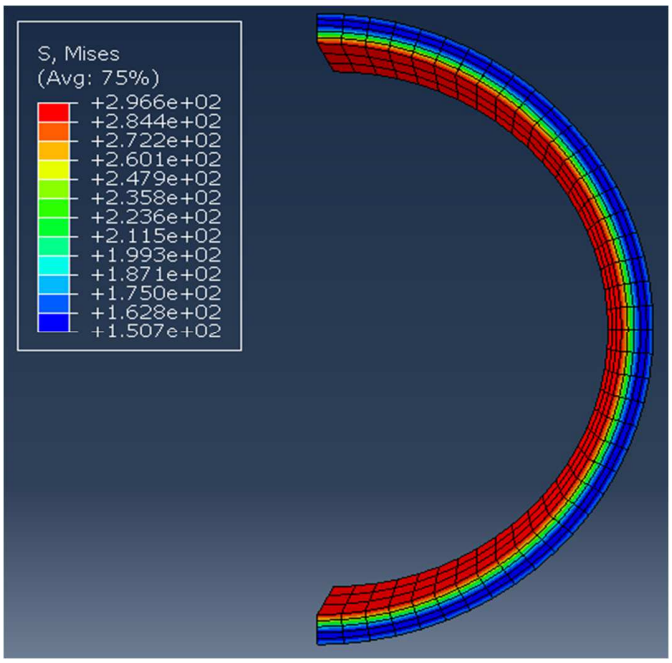

Figure 4.5.3: Elastic stress field for pure temperature.

Shakedown Analysis- Perfectly Plastic Material

The plot's axes are normalized with the shakedown bounds for pure loading and perfectly plastic material behaviour p_0 and T_0, respectively. These values were calculated as

$$p_0 = 23.6\,MPa, \qquad T_0 = 136\,MPa$$

The shakedown bounds for different ratios are given in table 4.6.

Table 4.6 Calculated shakedown bounds for perfectly plastic material.

Present PP	
p/p_0	T/T_0
0.00	1.00
0.24	0.94
0.44	0.88
0.56	0.84
0.66	0.79
0.72	0.72
0.78	0.59
0.84	0.42
0.92	0.23
1.00	0.00

Figure 4.5.4 shows good agreement between the shakedown diagram obtained here and others given in literature. The FEM discretization used was taken from Simon (2013). As a result, the fact that the corresponding lines are really close on the diagram was expected.

Computed shakedown domain of Hachemi (2005) is above the ones computed by the rest investigators. Consequently, the shakedown loads are overestimated. Nevertheless, the curves are qualitatively similar as well as the inclinations at the intercept points.

Alternating plasticity occurs in the regime of predominating temperature. In this area no influence of hardening can be observed, as it will be verified later.

On the other hand, the predominating pressure leads to incremental collapse. The limited kinematical hardening influences the shakedown curves, such that the according domains increase in direct proportion with the ratio σ_u/σ_y.

The diagram presents linear shape in each of the two areas. Where these lines seem to intersect, there is a transition from the one inadaptation mode to the other.

.

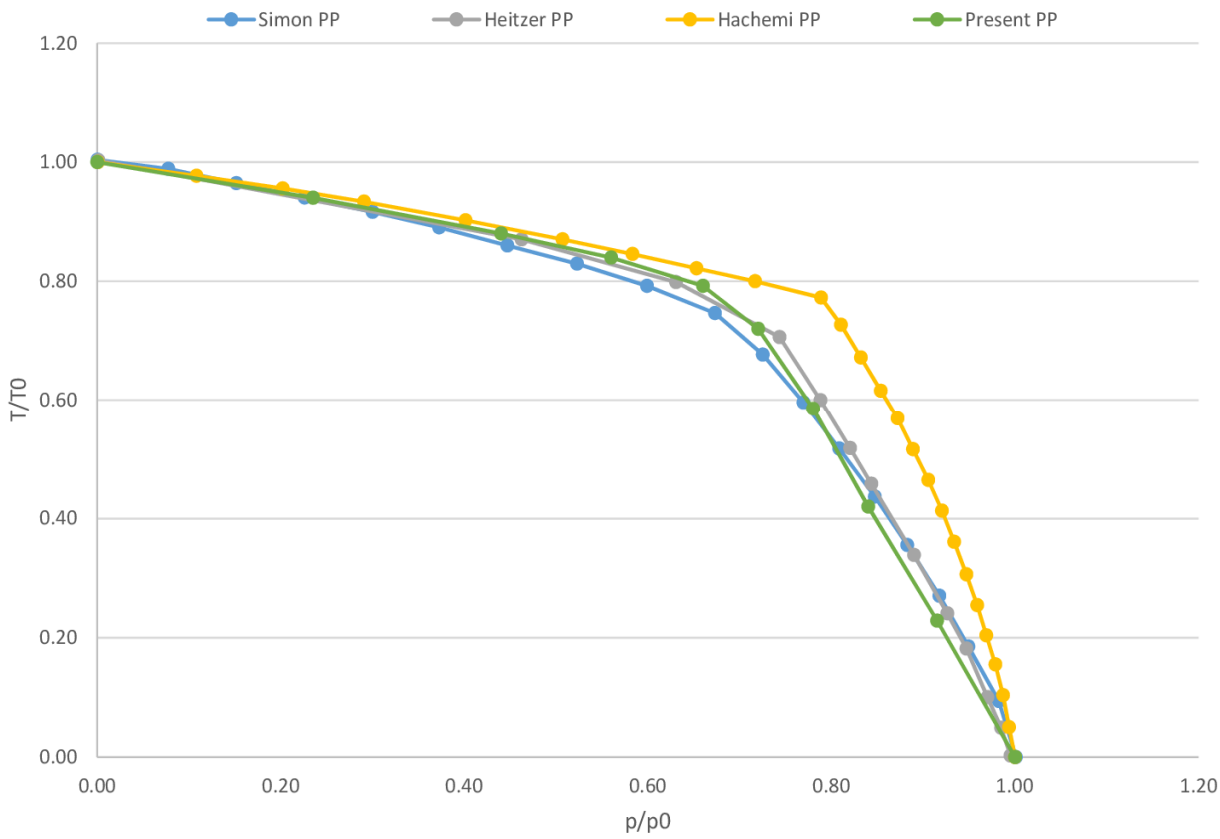

Figure 4.5.4: Shakedown domains for perfectly plastic material.

<u>Shakedown Analysis- Kinematic Hardening Material</u>

Here, a case of $\sigma_u/\sigma_y = 1.5$ is investigated. The obtained shakedown bounds are given in the following table.

Table 4.7 Calculated shakedown bounds for kinematic hardening material.

Present KH	
p/p_0	T/T_0
0.00	1.00
0.24	0.94
0.44	0.88
0.56	0.84
0.66	0.80
0.76	0.76
0.91	0.68
1.13	0.57
1.39	0.32
1.50	0.00

Only the case $\frac{T/T_0}{p/p_0} = 0.5$ will be presented extensively.

The plastic dissipation of the structure after 60 cycles is given in figure 4.5.5 for $p/p_0 = 1.13$.

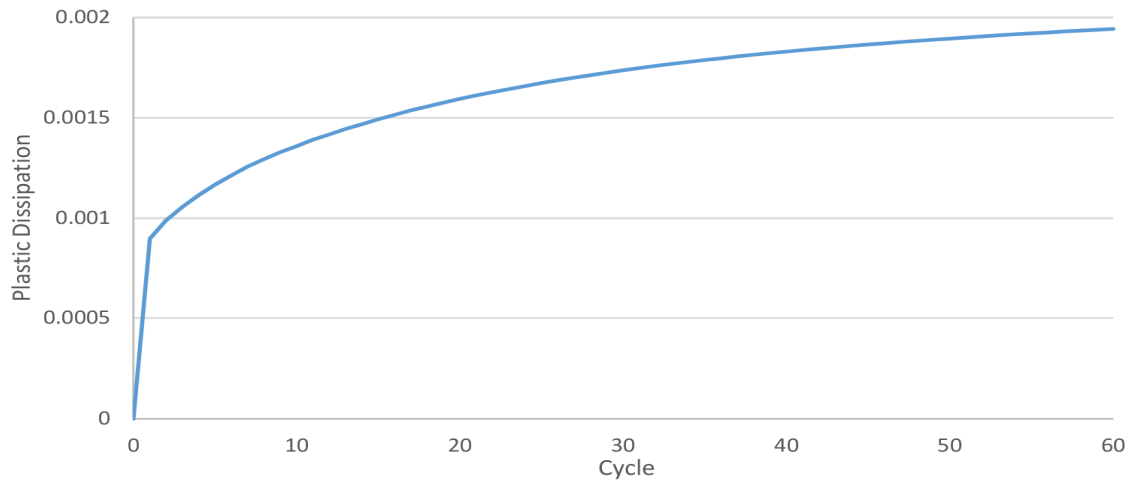

Figure 4.5.5: Plastic dissipation for the case $\frac{T/T_0}{p/p_0} = 0.5$ after 60 cycles.

It is not easy to decide whether the plastic dissipation will be bounded or not. For this reason, as discussed earlier, the increase of plastic dissipation with loading cycles is plotted in double logarithmic scale and the slope of a linear approximation of this line is calculated. In this example the slope is computed $s = -1.191 < -1$, so it leads to shakedown.

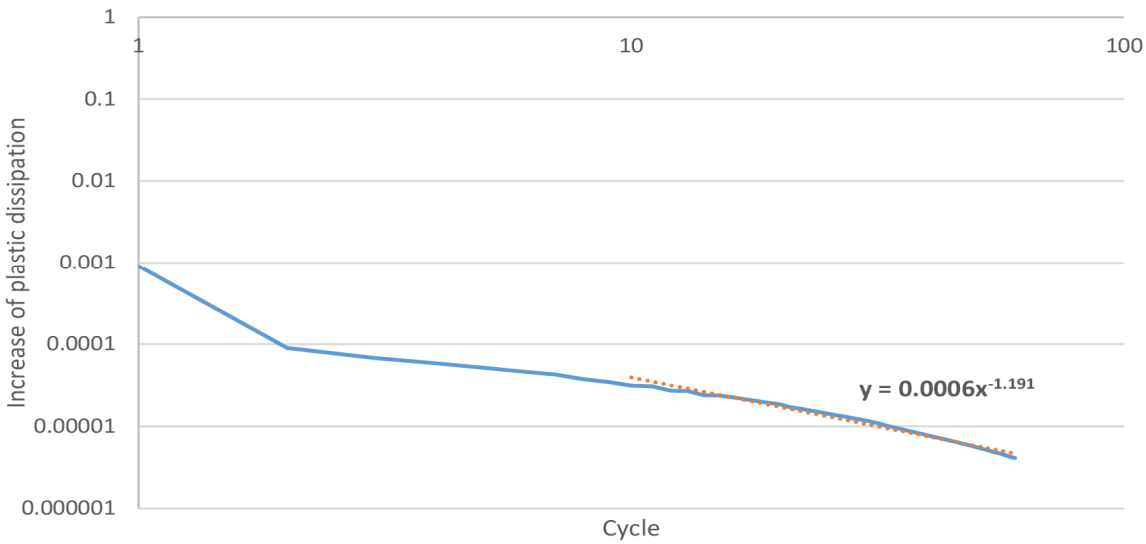

Figure 4.5.6: Increase of plastic dissipation for the case $\frac{T/T_0}{p/p_0} = 0.5$ after 60 cycles (double logarithmic axes).

The presentation of the shakedown diagram and the comparison with the one given in Simon (2013) is done in figure 4.5.7. The agreement between the two lines is satisfactory.

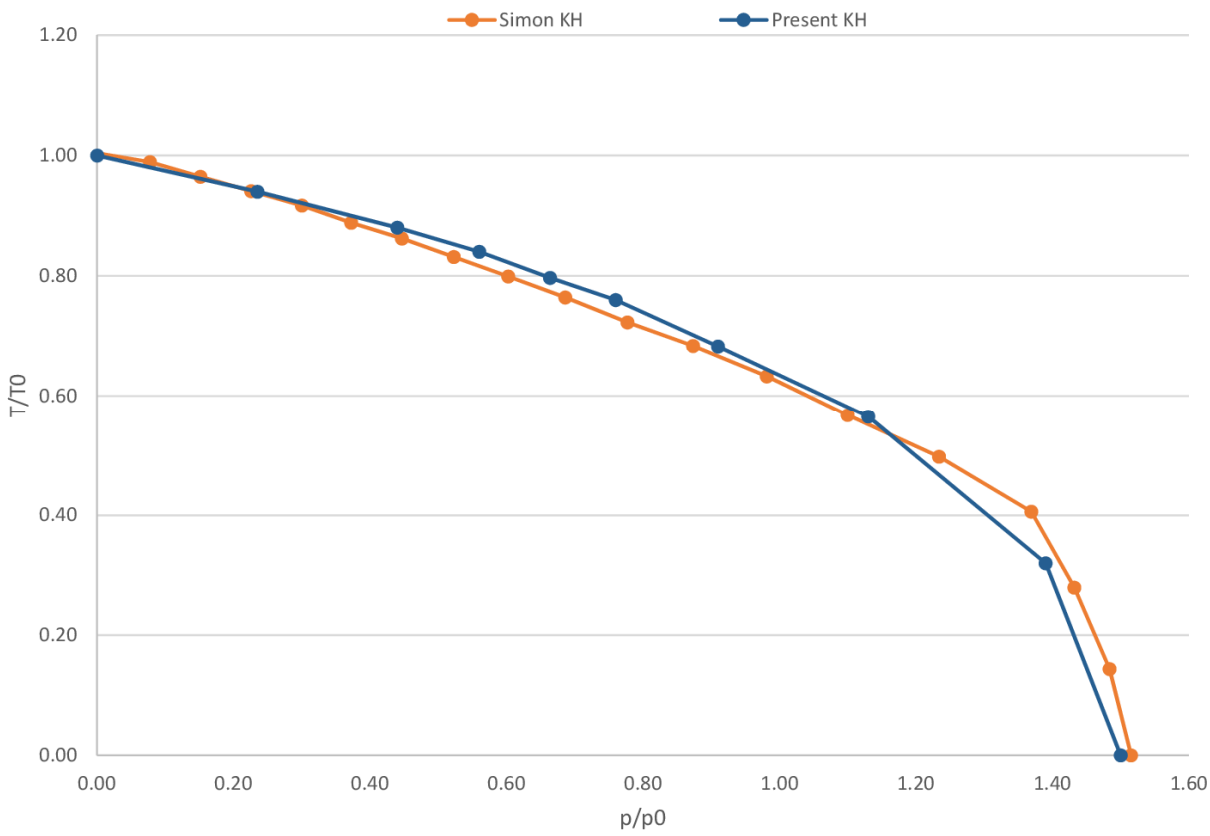

Figure 4.5.7: Shakedown domains for perfectly plastic material.

In order to evaluate the effect of hardening, the diagrams for perfectly plastic and kinematic hardening materials are given in figure 4.5.8.

It is clear that in the area of predominating temperature, hardening has no effect on the shakedown bound. This happens because the inadaptation mode is alternating plasticity as already discussed.

However, in the area of predominating pressure the shakedown bound increases proportionally to the ratio σ_u/σ_y.

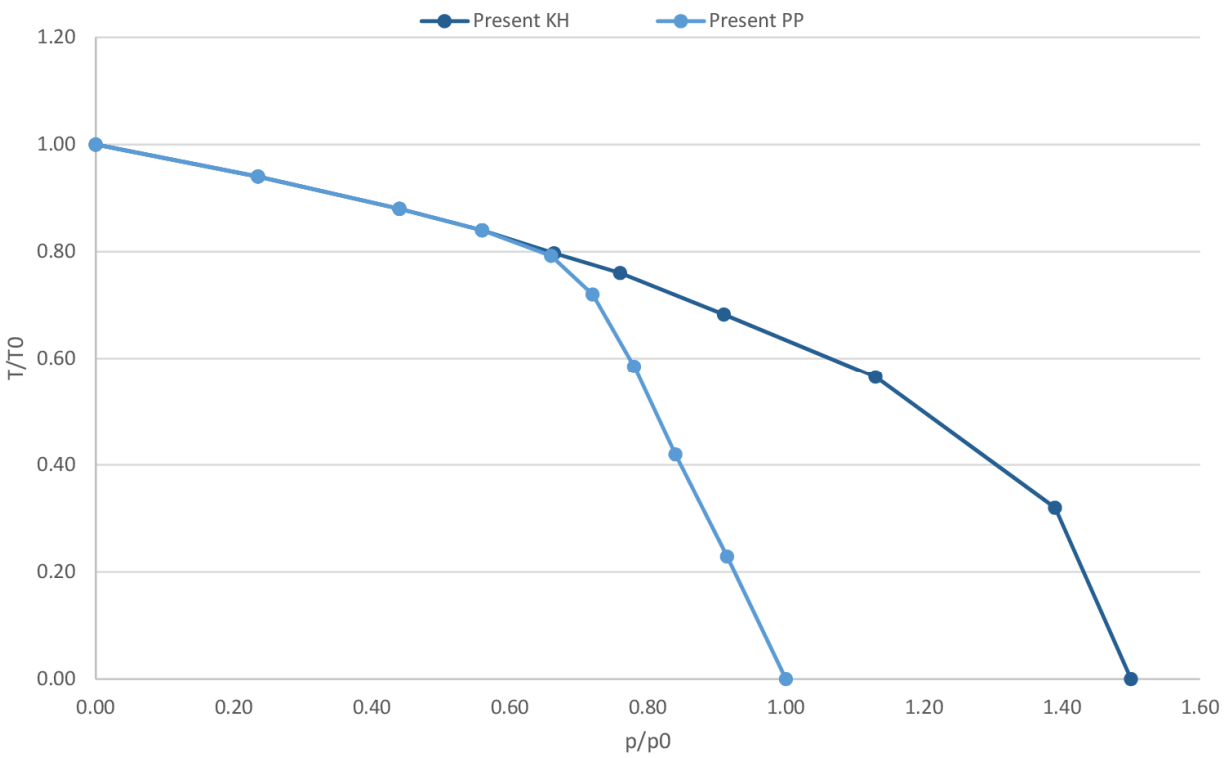

Figure 4.5.8: Effect of kinematic hardening

Bibliography

Books

[1] Jan König. Shakedown of Elastic-Plastic Structures. (1987)

[2] E. A. de Souza Neto, D. Peric, D. R. J. Owen. Computational Methods for Plasticity: Theory and Applications. (2008)

[3] J. Lubliner. Plasticity Theory. (2008)

[4] J. C. Simo, T. J. R. Hughes. Computational Inelasticity. (1998)

Papers

[5] S. Huang, Y. Xu, G. Chen, L. Zhang, A. Bezold, F. Qin. A numerical shakedown analysis method for strength evaluation coupling with kinematical hardening based on two surface model. (2019)

[6] K. Spiliopoulos, K. Panagiotou. A direct method to predict cyclic steady states of elastoplastic structures. (2012)

[7] J.-W. Simon. Direct evaluation of the limit states of engineering structures exhibiting limited, nonlinear kinematical hardening. (2013)

[8] M. Heitzer, G. Pop and M. Staat. Basis Reduction for the Shakedown Problem for Bounded Kinematic Hardening Material. (2000)

[9] P. Pham, K. Vũ, T. Tran, M. Staat. An upper bound algorithm for shakedown analysis of elastic-plastic bounded linearly kinematic hardening bodies. (2010)

[10] M. Staat, M. Heitzer. The restricted influence of kinematic hardening on shakedown loads. (2002)

[11] M. Heitzer, M. Staat, H. Reiners, F. Schubert. Shakedown and ratchetting under tension–torsion loadings: analysis and experiments. (2003)

[12] A. Hachemi. Sur les méthodes directes et leurs applications. Habilitation, Université des Sciences et Technologies de Lille, France. (2005)

[13] D. Weichert, J. Groß-Weege. The numerical assessment of elastic–plastic sheets under variable mechanical and thermal loads using a simplified two-surface yield condition. (1988)

Ph. D Theses

[14] S. Mouhtamid. Anwendung direkter Methoden zur industriellen Berechnung von Grenzlasten mechanischer Komponenten. Ph.D. Thesis. (2007)

[15] P. Pham. Upper Bound Limit and Shakedown Analysis of Elastic-Plastic Bounded Linearly Kinematic Hardening Structures. (2011)

Abaqus Manual

[16] Smith, M. ABAQUS/Standard User's Manual, Version 6.9. Dassault Systèmes Simulia Corp, Providence, RI. (2009)